ACTA UNIVERSITATIS UPSALIENSIS
Uppsala Dissertations from the Faculty of Science and Technology
144

Eleni Myrto Asimakopoulou

Search for charged Higgs bosons with tau-lepton signatures at the ATLAS experiment of the Large Hadron Collider and development of novel semiconductor particle detectors

UPPSALA
UNIVERSITET

Dissertation presented at Uppsala University to be publicly examined in Room 4001, Ångströmlaboratoriet, Lägerhyddsvägen 1, Uppsala, Friday, 26 February 2021 at 13:00 for the degree of Doctor of Philosophy. The examination will be conducted in English. Faculty examiner: Paula Collins (CERN, Switzerland).

Abstract

Asimakopoulou, E. M. 2021. Search for charged Higgs bosons with tau-lepton signatures at the ATLAS experiment of the Large Hadron Collider and development of novel semiconductor particle detectors. *Uppsala Dissertations from the Faculty of Science and Technology* 144. 192 pp. Uppsala: Acta Universitatis Upsaliensis. ISBN 978-91-513-1112-8.

Experimental High Energy Physics (HEP) studies are discussed in the context of exotic particle searches and data analysis techniques and the development and production of suitable detectors. The main covered topics span the aforementioned areas and are primarily related to the ATLAS experiment at the Large Hadron Collider (LHC).

The Higgs boson discovery by the ATLAS and CMS experiments in 2012, solidified the Standard Model (SM), but at the same type provided a suitable probe for searches of new physics, beyond the SM (BSM). This thesis covers a study for a new particle, the charged Higgs boson, which is predicted by several BSM theories and its discovery would be a clear sign for new physics. The study was focused on the predicted $\tau\nu$ final state using a 36.1fb-1 dataset of pp collisions collected at $\sqrt{s}$ = 13TeV with the ATLAS detector. No discovery was made, but new limits on relevant parameters were set.

Studies that involve hadronically decaying τ leptons, such as the aforementioned charged Higgs boson search, are affected by background processes where quark- and gluon-initiated jets as misidentified as τs. A universal method for determining the impact of this background, and the associated systematic uncertainties, is being developed in ATLAS and is introduced in this thesis.

The Large Hadron Collider (LHC) is presently preparing for the High-Luminosity upgrade that is designed to meet the current physics goals. The upgrade will result in more demanding conditions for the LHC experiments, in terms of higher particle fluences and larger collected data volumes, necessitating changes in their detector systems. The ATLAS inner tracker upgrade is discussed, focusing on the workflow and the quality assurance and quality control procedures necessary for the production of the strip modules that will be part of its new end-cap system in collaboration with industry.

Neutron detection is essential for a wide range of neutron science applications and research. The evaluation of a novel boron-coated semiconductor with respect to its suitability of neutron detection is discussed.

Eleni Myrto Asimakopoulou, Department of Physics and Astronomy, High Energy Physics, Box 516, Uppsala University, SE-751 20 Uppsala, Sweden.

ISSN 1104-2516
ISBN 978-91-513-1112-8
urn:nbn:se:uu:diva-429940 (http://urn.kb.se/resolve?urn=urn:nbn:se:uu:diva-429940)

To my family
- for being the backbone in my life,
my friends
- for making it colorful and
Lefteris
- for being you.

Contents

1. Introduction

All gathered knowledge in Physics has been a result of theoretical breakthroughs and experimental observations. In the scope of high energy physics, this knowledge has been summarized in the Standard Model (SM) which provides, along with the General Relativity theory, a robust but inherently incomplete description of nature.

This thesis summarizes the work of the author in topics surrounding the analysis of experimental data and detector development for high energy physics experiments and is segmented in five parts. The first part aims to provide an overview of the relevant theoretical background for the presented projects. It will cover the SM (Ch. 3) and theories expanding beyond it, Beyond SM theories or BSM in short, (Ch. 4) that will be relevant for later chapters, and will also give a theoretical overview of semiconductors and introduce two detector structures that will be important in the thesis (Ch. 5).

The validation of the SM and searches for BSM theories are possible through research facilities such as the Large Hadron Collider (LHC) at CERN. The majority of the presented work has been conducted in the scope of the LHC, which will be introduced in Chapter 6, and more specifically, the ATLAS experiment (Ch. 7). The drawing of meaningful conclusions is only possible after comparisons of the experimentally collected data to the yields and shapes expected from theoretical predictions, which is commonly performed in the scope of hypothesis testing (Ch. 8).

The third part will cover data analysis techniques, and searches carried out with the ATLAS detector. Physics searches are often limited because of the inability to distinguish a signal event from other processes (background) that leave similar signatures in the detector. In the case of physics searches that rely on τ leptons, one type of interfering background are jets that originate from quarks or gluons. Chapter 9 will introduce the efforts of a dedicated ATLAS task force in the development of a universal method of determining this source of background, and the associated systematic uncertainties, through a dedicated tool. Chapter 10 will cover a search for a charged Higgs boson. The existence of this boson is predicted by several BSM theories, but not from the SM, which would make a potential discovery a clear sign of new physics.

Physics understanding has unquestionably been pushed into new regimes with the LHC, yet it is possible to do better. The fourth part concerns the presently ongoing High-Luminosity LHC upgrade (Ch. 11), which aims to further the potential of physics observations in the upcoming years. A side effect will be a more harsh operating environment for the experiments, necessitating changes in their systems. The upgrade of one of the ATLAS detector

subsystems will be discussed in Chapter 12. The chapter will introduce the new detector subsystem and will focus on the production of one of its base units.

The last part of the thesis concerns a non-LHC related project surrounding neutron detectors. Neutron-based science (Ch. 13) is applicable in many different areas and motivates the need for developing neutron detector technologies (Ch. 14) that meet the present needs and available resources. A study investigating the suitability of a novel semiconductor-based detecting setup for neutron detection is introduced in Chapter 15.

List of publications

Parts of the work presented in this thesis is published in the following:

1. ATLAS Collaboration, *Search for charged Higgs bosons decaying via* $H^{\pm} \to \tau^{\pm}\nu_{\tau}$ *in the* τ*+jets and* τ*+lepton final states with* $36\,\mathrm{fb}^{-1}$ *of pp collision data recorded at* $\sqrt{s} = 13\,\mathrm{TeV}$ *with the ATLAS experiment*, JHEP, vol. 09, p. 139. 46 p, Jul 2018.
2. L. Poley, et al., *The ABC130 barrel module prototyping programme for the ATLAS strip tracker*, JINST, vol. 15, p. P09004. 82 p, Sep 2020.
3. E. M Asimakopoulou, on behalf of the ATLAS Collaboration, *Performance of the ATLAS tau-lepton trigger at the LHC in Run 2*, PoS LeptonPhoton2019 (2019) 124, Tech. Rep. ATL-DAQ-PROC-2019-016, CERN, Geneva, Sep 2019.

Author's contribution

As in most research areas, an individual's work is only possible because of collaborations. This holds true for all research projects and becomes more pronounced in the scope of large experiments, such as the ATLAS experiment, where the collaboration includes more than 3000 people. The present work is no exception, yet an attempt to single-out the author's contribution is given below.

For the work described in Chapter 9 the author contributed to studies on the discriminating power of the jet-width in the splitting of the considered fake τ jet origins in four types; b-quark jets, non-b-quark jets, gluon jets and unmatched objects. Additionally, the author is conducting ongoing studies on the possibility to account for different contributions in the non-b-quark type, namely from c-quarks and quarks of lighter origin, separately, as it is described in the text. All studies have been conducted in Monte Carlo simulations.

For the work conducted in Chapter 10 the author was responsible for the efficiency estimation of the employed missing transverse energy triggers and

the calculation of their associated uncertainties. The work is summarized in Sec. 10.5 and is published in Paper-1.

The author was heavily involved in all the UU related activities that are described in Chapter 12. The work entailed the quality assurance of all employed procedures during module production, both in the in-house and industrial environment, and the subsequent performance of electrical and metrology quality control tests. Parts of this work are published in Paper-2. In several occasions, the author worked on the design and prototyping of necessary jigs and tools, such as the custom ASIC pick-up head for the industrial hybrid assembly and the support and alignment structures for the mini pick-and-place machine used at Uppsala University for the local hybrid assembly.

The work described in Chapter 15 was primarily conducted by the author unless otherwise stated. This excludes the study concept (R. Brenner), the design of the read-out board for Phase-I (N. Bingefors), the bonding (L. Lindquist) and the boron coating (experts at the ESS Linkoping facilities) of the sensor.

The author has also been involved in different contribution levels to ATLAS projects that are not included in this thesis. These include the maintenance and further development of the HLT tau trigger monitoring software, the generation and validation of signal samples needed for di-Higgs boson searches through the $bb\tau\tau$ channel and software development for simulated performance studies of a track trigger for the High-Luminosity LHC upgrade.

2. List of abbreviations

The use of abbreviations in this thesis was unavoidable. Each abbreviation is introduced before its use, yet to make the reading slightly less confusing a list of the used abbreviations and acronyms are listed below in alphabetical order.

2HDM	two Higgs Doublet Models
4FS	four-Flavor Scheme
5FS	five-Flavor Scheme
ABC	ATLAS Binary Chips
AMAC	Autonomous Monitoring and Control ASIC
ASICs	Application Specific Integrated Circuits
BDT	Boosted Decision Trees
BF3	Boron triFluoride
BR	Branching Ration
BSM	Beyond the SM theories
C	Charge-Symmetry or Color charge, the use is clear in the context
CL	Confidence Level
CMOS	Complementary Metal-Oxide-Semiconductor
CR	Control Region
CSC	Cathode Strip Chambers
DAQ	Data AcQuisition
EC	End-Cap
EM	Electromagnetic (force, calorimeter)
ENC	Equivalent Noise Charge
ESD	ElectroStatic Discharge
EWBS	ElectroWeak Symmetry Breaking
FCNCs	Flavor Changing Neutral Currents
FF	Fake Factor
FTTF	Fake Tau Task Force
GSC	Global Sequential Correction
HAD	hadronic calorimeter
HCC	Hybrid Controller Chips
HEP	High-Energy Physics
HL-LHC	High Luminosity LHC
HLT	High-Level Trigger (software trigger)
hMSSM	habebus-MSSM
HV	High Voltage
HV-MAPS	High-Voltage MAPS
IBL	Insertable B-Layer
ID	Inner detector

Continued on next page

IPs	Interaction Points
ITk	Inner tracker detector (ATLAS detector upgrade)
IV	Leakage current vs Voltage measurement
JES	Jet Energy Scale
L1	level-1 trigger (hardware trigger)
L1Calo	level-1 trigger using calorimeter information
L1Muon	level-1 trigger using muon spectrometer information
L1Topo	level-1 topological trigger
LAr	Liquid Argon
LS	long trip
MAPS	Monolithic Active Pixel Sensors
MC	Monte Carlo
MDT	Monitoring Drift Tubes
MET	Missing Transverse Energy
ML	Maximum Likelihood
MS	Muon Spectrometer
MSSM	Minimal Supersymmetric Standard Model
MVA	MultiVariate Analysis
NLO	Next-to-Leading Order
P	Parity-Symmetry
PDF	Probability distribution function
PLA	PolyLactic Acid material
PMOS	p-channel Metal-Oxide-Semiconductor
prongs	number of tracks, refers to the reconstructed tracks associated with a tau particle
PS	Proton Synchrotron
PSB	Proton Synchrotron Booster
PV	Primary Vertex
QA	Quality Assurance
QC	quality control
QCD	Quantum Chromo Dynamics
RNN	Recurrent Neural Networks
RoIs	Regions of Interest
RPC	Resistive Plate Chambers
SANS	Small Angle Neutron Scattering
SCT	Semiconductor Tracker
SET	Single-Event Transient
SEU	Single-Event Upset
SM	Standard Model
SNF	Strong Nuclear Force
SNR	Signal-to-Noise Ratio
SPS	Super Proton Synchrotron
SR	Signal Regions
SS	Short Strip
SSB	Spontaneous Symmetry Breaking
SUSY	SUperSYmmetry

Continued on next page

T	Time-Symmetry
TDAQ	Trigger and Data AcQuisition system
TFFT	Tau Fake Factor Tool
TGC	Thin Gap Chambers
TID	Total Ionization Dose
TRT	Transition Radiation Tracker
TTC	Trigger, Clock and Control
TV	Tau Vertex
WNF	Weak Nuclear Force

Continued on next page

Part I:
Introduction and theoretical background

3. The Standard Model

Physics is the science surrounding the questions of "what?", "how?" and "under what circumstances?" in a consistent and repeatable manner. Depending on the scale (e.g. length and energy) that one chooses to address these questions, the considered fundamental blocks behave differently. In particle physics this is discussed in the context of the elementary building blocks of matter and their interactions. All current understanding of elementary particle physics is described within the Standard Model (SM), which provides along with General Relativity a robust but inherently incomplete description of nature.

Before moving on to a more technical description of how things fit together, it would be useful to first introduce the elementary particles that are known today. The particles are commonly divided based on their intrinsic angular momentum properties, called spin, into fermions (spin of $1/2$) and bosons (spin of 0 or 1). Fermions are the matter-building particles and are consisted of quarks and leptons. Leptons consist of three "flavors"; the electron (e^-), muon (μ^-) and tau (τ^-) and their respective neutrinos (ν_e, ν_μ, ν_τ). Quarks have six different types, known as up (u), down (d), strange (s), charm (c), bottom (b) and top (t), in order of increasing mass. Each of the fermions is also attributed an anti-particle, which shares the same mass but opposite quantum numbers (defined later in the text). The bosons are split in scalar (spin-0) and vector (spin-1) categories, with the latter being often referred to as the force-carriers. These include the Higgs boson and the gluon, photon, Z and $W^\pm$ bosons respectively. The particles are summarized in Fig. 3.1, along with their mass, charge and spin characteristics. They are grouped in generations, the choice of which will become clear later in the text.

Assuming an observable in nature, which could be a particle, a ball or a planet, if one wishes to describe or study it they would have to determine a system that surrounds it and a meaningful way to correlate actions or states of the object with respect to that system. Different approaches can offer different advantages and one needs to remain dynamic in their choices. The only requirement is that all descriptions encapsulate accurately the physics, and this is reflected by the ability of transforming one description into another without any effect on the physics properties. The most common methods of description in physics are the Lagrangian and Hamiltonian formalisms. They offer the common language for describing the physical world and discussing and evaluating existing or new states and interactions.

The state of a physical system can be formulated through a Lagrangian based on information of its potential and kinetical energies. Changes of the

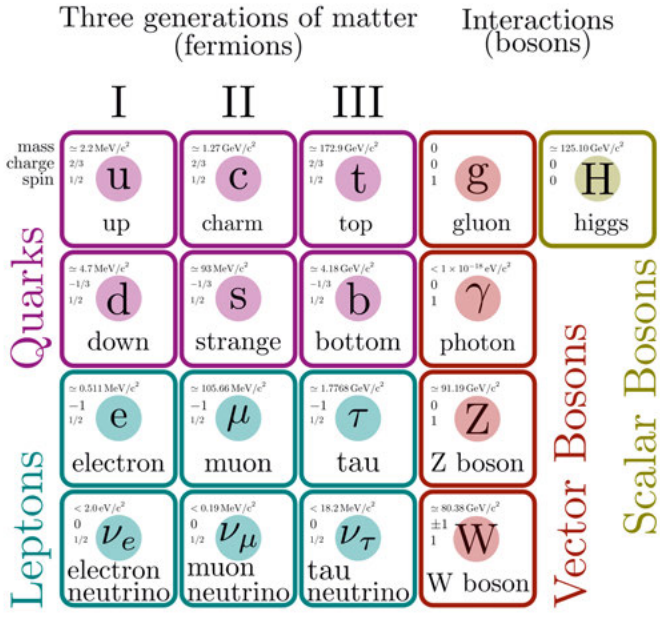

Figure 3.1. Table of known elementary particles. The information listed in the table are from [1].

system need to respect the principal of minimal action, which is equivalent to requiring a Lagrangian that minimizes the action of the system. The correct Lagrangian that describes a system is determined from the exhibited symmetries in the system. The Lagrangian is recorded in a configuration space, where a point is expressed from all the locations that the objects in the system have at a given point in time.

Another approach of describing the same physical system would be from the position and momentum change rates of its objects. This is known as a Hamiltonian formalism and is recorded in a phase space, where a point is defined from the position and momenta of the objects in the system. The Hamiltonian is intrinsically linked to the time direction, as it can be considered as a generator of translations in time. Mathematically, the Lagrangian and Hamiltonian formalisms are related by a Legendre Transformation.

The SM description of nature is a quantum field theory whose Lagrangian is invariant under space-time translations, rotations and boosts of the Poincare group. Following the notion that the physics should remain the same regardless of the description system, the physical meaning that is mathematically formulated through the Lagrangian should not be dependent on the reference frame but needs to remain gauge invariant. This needs to be followed when defining basic properties of the system, such as the concept of vacuum. The vacuum in this context is considered to be a collection of elementary parti-

cle fields capable of creating and annihilating particle states. It is essential to stress that the Lagrangian remains the mathematical representation of nature and as such it needs to preserve its gauge invariance regardless of the properties of the physical vacuum.

This becomes important when considering that particles can be formed in the physical vacuum with non-zero vacuum expectation values. Such particles have a defined vacuum ground state and therefore will not be invariant under all symmetries of the Lagrangian. This would imply that a vacuum state will not have all the same symmetries of the Lagrangian. According to the Nambu-Goldstone theorem [2] for each of the Lagrangian symmetries that are not satisfied from the vacuum state there needs to exist a massless scalar boson (Goldstone bosons), which will interact according to the symmetries of the Lagrangian.

This is observed in the case of the Higgs scalar field [3–5]. The associated Goldstone boson is named the Higgs boson and was the last particle of the SM to be discovered in 2012 [6, 7]. Details of the mechanism that predicted the existence of the boson will be discussed later in the text.

Having chosen an appropriate formalism for describing elementary particles and defined the concept of vacuum, it is possible to discuss forces within the system. It is believed that all forces were once united into a single force and as time progressed, branches of the original force started forming independently. Gravitation became separated at around 10^{-46} s from the other forces, followed by the strong nuclear force (SNF) at 10^{-36} s. The remaining unified force is commonly referred to as the electroweak force, which eventually branched further, with the separation of the electromagnetic (EM) and weak nuclear force (WNF) at 10^{-12} s, resulting in the four separate forces that are observed today. Puzzling together the way that the gravitation, SNF, EM and WNF forces fit together furthers the understanding of their present manifestations.

Particles undergo interactions with one another through force exchange. Interactions are considered as a reflection of the system's fundamental internal symmetries and are mathematically described by operators that commute with the Hamiltonian of the system. The commutation of the operators indicates a conserved charge associated with the exchange and the equivalent eigenvalue of such an operation is called a quantum number. The forces (i.e. the underlying symmetries) are propagated through the boson particles mentioned earlier, which are also referred to as mediators.

The symmetries that have been successfully incorporated into the SM Lagrangian formalism are those of the strong and electroweak forces. The strong force corresponds to a Lagrangian symmetry under rotations of the so-called *color* eigenstates. The conserved quantity is named *color* and it exists in three

states; red, green and blue. Only quarks are affected by the strong force[1], while leptons are invisible to it.

Matter is only formed in *color*-less, bound quarks states (*hadrons*) of two, three or more quarks. *Baryons* (three quark groupings) achieve this by combining quarks each with a different color (red, green, blue), while *mesons* (two quark groupings) are *color*-anti*color* formations (ex. red and anti-red). The part of the Lagrangian that expresses the force is invariant under local gauge transformations of the $SU(3)_C$ group, where 'C' stands for *color*. The strong force is mediated via gluons, which are massless, carry color charge, but not electric charge.

From a technical point of view, the weak and electromagnetic interactions are the outcome of a Lagrangian that is invariant under local gauge transformations of the direct product group $SU(2)_L \times U(1)_Y$. The conserved quantity that is associated with this symmetry is called Hypercharge and it plays an important role in the grouping of the elementary particles, as they are in fact grouped to represent eigenstates of rotational invariance under this symmetry. As an example, the *electron* and *electron neutrino* leptons transform into one another through an $SU(2)_L \times U(1)_Y$ transformation, while keeping a constant hypercharge. In a similar fashion the same holds true for *up* and *down* quarks.

The physical vacuum however does not exhibit the same symmetry but rather a subgroup of the original symmetry: $U(1)_{EM}$. This poses an interesting asymphony that the Higgs mechanism addresses rather elegantly; one needs to break the $SU(2)_L \times U(1)_Y$ gauge symmetry to the electromagnetic $U(1)_{EM}$ through a spontaneous symmetry breaking (SSB):

$$SU(2)_L \times U(1)_Y \xrightarrow{SSB} U(1)_{EM}. \tag{3.1}$$

Through this SSB, one can give mass to three of the gauge bosons mediating the electroweak interaction at the cost of introducing a new scalar bosonic field, the Higgs field, which will be transforming under the electroweak gauge group [8] and interact with other SM fields. The end results is the splitting of the two forces, each having its own mediators; the observed $U(1)_{EM}$ symmetry is the electromagnetic force with the photon as its mediator and the electric charge as the associated quantum number, while the weak force is mediated via three massive bosons; two of which are charged ($W^{\pm}$) and one is neutral (Z^0). The weak force mediators allow the transformation between "up-type" and "down-type" states of the original electroweak symmetry that were mentioned before. The coupling of the Higgs field to the other SM fields is what gives mass to the $W^{\pm}$ and Z^0 mediators of the weak force, and also to the fermionic particles through the Yukawa coupling. Concerning the latter, the mechanism results in a post-SSB Lagrangian form that naturally includes masses for the leptons and quarks and it also predicts the couplings in a mass-proportional

[1] The strong interactions are described via the quantum chromodynamics (QCD) theory.

way. One caveat however is that neutrinos are predicted to be massless, while experimental observations suggest otherwise [9, 10].

The symmetries that have been mentioned so far, in the context of forces, concern only internal symmetries of the system. Other types of symmetries that a physical system exhibits can be discrete symmetries such as charge (C), parity (P) and time (T) conservation. The symmetries correspond to the exhibition of the same system properties when changing a particle with its anti-particle (C-symmetry), mirroring the reference system coordinates (P-symmetry) and carrying out transformations in either directions (T-symmetry) respectively. The CPT-conservation symmetry is considered to be a global symmetry, while the CP-conservation symmetry can be observed but it depends on the context. The observation of a CP-symmetry in the strong interactions is often discussed as an interesting puzzle as it is not required in any formulation of the SM, yet it has not been observed to be broken.

The strong CP-symmetry puzzle along with the neutrino mass problem, can serve as a good prelude to exploring physics beyond the discussed SM, which will be the focus of the next chapter.

4. Beyond the Standard Model

4.1 Shortcomings of the Standard Model

The SM is a robust theory that has been studied extensively, but however fails to give the full picture. Two examples that were mentioned in the previous chapter are the fact that it fails to predict neutrino masses[1] and that it does not offer an explanation for the non-observance of any strong CP-symmetry violation. There is also a rather poor understanding of the fermionic sector and its structure, with some examples being the inability to explain why there seem to be three generations or why the generations exhibit such a mass hierarchy. Additionally, there is motivation to build up to a more inclusive theory, unifying the electroweak and strong forces, which the SM cannot deliver, while it also fails to explain the relevant coupling strengths of the forces (hierarchy problem).

From the cosmological point of view, the shortcomings of the SM extend to the lack of explanation for the observed matter-antimatter ratio in the universe and its inability to incorporate gravity into the model. Perhaps one of the most interesting problems that the SM leaves open is the lack of justification for the suggestive evidence for dark energy and dark matter in the universe.

Theories that expand outside of the SM framework are called Beyond the SM theories (BSM) and focus on one or more of the open questions from the SM. Depending on the area that one wishes to explore, the established parts of the SM can serve as useful probes for further explorations, with the Higgs boson being one of them.

4.2 Two-Higgs-Doublet Models

The discovery of the Higgs boson was the last missing piece that solidified the SM, yet at the same time it can serve as a probe for new physics. Studies of the particle's interactions can potentially lead to observations of deviations on its couplings from the SM predictions, which would be a flag for new physics. Also the Higgs boson could belong to an extended scalar sector that realizes electroweak symmetry breaking (EWSB) and could serve as a portal to study such extensions further.

[1] The SM can be extended to account for the neutrinos as massive, but what is missing is the mechanism that predicts their masses.

Pivoting from the second point raised; there exist many possible extensions and deformations of the minimal Higgs sector that, in contrast to the simplest-possible scalar structure that is assumed in the SM, include additional scalar doublets and/or singlets, or even more complex structures involving triplets. One of the simplest class of extensions are theories with two Higgs fields transforming as doublets under $SU(2)_L$ and with unit $U(1)_Y$ charge, abbreviated as two-Higgs-doublet models (2HDM) [11, 12]. 2HDMs are motivated by supersymmetry theories [13], axion models [14] and even the observed baryon asymmetry in the Universe [15] and they commonly follow the assumption of CP-conservation.

In 2HDM two fields realize the EWSB and there are eight real scalars. Three of the scalars are consumed by the EWSB, leaving five physical scalars where two are CP-even Higgs bosons (h and H with a mixing angle α where H is heavier than h by convention), one is a CP-odd Higgs boson A and two are charged Higgs bosons $H^{\pm}$. The model is fully described with six physical parameters; the four Higgs masses (m_h, m_H, m_A, $m_{H^{\pm}}$), the ratio of the two vacuum expectation values ($\tan(\beta)$) and the mixing angle (α) which diagonalizes the mass matrix of the neutral CP even Higgs particles. This is a richer phenomenology compared to the SM which uses only 2 parameters; the mass of the Higgs boson and its self-coupling parameter, λ[2].

The two Higgs doublets of the model can be denoted as Φ_1 and Φ_2. The presence of the additional doublet can introduce flavor changing neutral currents (FCNCs) [3], which however have not been observed. It is possible to avoid tree-level FCNCs by requiring the two fields to satisfy the Glashow-Weinberg condition [16] and only interact with exactly one of the fermionic types (*up*, *down*, *leptons*) of a given gauge representation. For Φ_1 and Φ_2, the condition is satisfied by precisely four discrete types of 2HDM distinguished by the possible assignments of fermion couplings. Following a convention that Φ_2 is fixed to be the Higgs doublet that couples to the *up* quark, the four types are as indicated in Tab. 4.1.

	Type-I	Type-II	Type-III	Type-IV
u	Φ_2	Φ_2	Φ_2	Φ_2
d	Φ_2	Φ_1	Φ_2	Φ_1
e	Φ_2	Φ_1	Φ_1	Φ_2

Table 4.1. *Types of 2HDM that satisfy the Glashow-Weinberg condition. The rows "u", "d" and "e" are used to indicate to the relevant elementary particles' generations.*

[2]The Higgs boson self-coupling is predicted within the SM, but has not been experimentally observed yet.

[3]FCNCs are interactions that allow a fermion's flavor change while keeping the electrical charge the same.

The most relevant type for the analysis that will be discussed in this thesis is the Type-II 2HDM.

4.3 Minimal Supersymmetric Standard Model and associated scenarios

The Type-II 2HDM is considered to be the Higgs sector of the Minimal Supersymmetric Standard Model (MSSM) [17], where the MSSM is a minimal model that realizes supersymmetry (SUSY) by considering the minimum number of new particle states and new interactions required. SUSY is an extension of the SM by defining superpartners to all discovered particles, characterized by heavier masses and a $1/2$ spin-offset. It can be summarized as a symmetry between bosons and fermions, that hence necessarily relates particles with different spins [18]. Observation of any SUSY particles would be an important breakthrough in the understanding of physics, but no such experimental evidence has been found yet. The MSSM accounts for the lack of observation of any of the SUSY particles by introducing a soft SUSY breaking that predicts the superpartners to have high masses. In SUSY theories the superpotential, i.e. the combination of superfields which encode the interactions of particles and their supersymmetric partners in a Lagrangian, need to only be a function of either only the particles or only the superpartners (holomorphic). The forbidding of such crossing terms automatically implies that the MSSM contains a Type-II 2HDM, where each fermion flavor couples to only one of the Higgs doublets [19].

In the case where, additionally to the Glashow-Weinberg condition, it is required that an MSSM model ensures CP conservation (as mentioned earlier), the couplings of the physical scalars at tree-level to the fermions and massive boson of the SM are typically set with respect to only two parameters: the mass of CP-odd Higgs boson A, $\mathrm{m_A}$ (or the mass of charged Higgs boson, $\mathrm{m_{H^\pm}}$, depending on the search focus[4]), and the angle β, which parameterizes the relative contribution of each doublet to the EWSB via $\tan(\beta) := \frac{\langle\Phi_2\rangle}{\langle\Phi_1\rangle}$, ie the ratio of the vacuum expectation values of the fields. One specific case of interest is the one where α and β satisfy the relation: $\cos(\beta-\alpha) \sim 0$, which is called the "alignment limit" and h behaves like the SM Higgs.

Other assumptions, such as those on the masses of the supersymmetric partners, can be used to define a variety of MSSM benchmark scenarios. Some examples, that will only be briefly mentioned and not further discussed here, are the $\mathrm{m}_h^{\mathrm{max}}$ and $\mathrm{m}_h^{\mathrm{mod}\pm}$ scenarios [20]. In the first, the benchmark values are chosen such that the mass of the observed light CP-even Higgs boson is maximized for fixed $\tan(\beta)$ and large $\mathrm{m_A}$ and can be used to derive conser-

[4]Charged Higgs boson searches use the charged Higgs boson mass parameter over the mass of the CP-odd Higgs boson.

vative lower bounds on m_A, $m_{H^\pm}$ and $\tan(\beta)$. The mass of the light CP-even Higgs boson in the m_h^{max} scenario however is in agreement with the discovery of a particle similar to the discovered Higgs boson in only a relatively small region of the m_A-$\tan(\beta)$ plane and at rather low $\tan(\beta)$ values. The modified, $m_h^{mod\pm}$, scenarios attempt to maximize the agreement with the experimental discovery by altering the amount of mixing in one of the superpartner sectors. Another MSSM scenario is the habebus-MSSM [21], or hMSSM, where the measured value of the Higgs boson (125 GeV) is used to predict the remaining Higgs boson masses and couplings. The scenario allows to parameterize the CP-conserving MSSM Higgs sector without choosing explicitly the soft-supersymmetry-breaking parameters.

Searches for hMSSM-abiding extended sectors that satisfy the alignment limit are carried out through different analysis channels. Studies that look for charged Higgs bosons offer an opportunity to detect a clear sign of new physics. In the case that such particles are observed it would be an indisputable sign for the existence an extended Higgs sector, given that the SM does not predict any charged scalars, regardless of the underlying phenomenology. One such study will be presented in Ch. 10.

5. Semiconductor detectors

Every theory needs to be validated by experimental measurements. This is naturally also true for the SM, that has been extensively verified and challenged by experimental measurements, and BSM theories, that have so far only been challenged by exclusion limits (discussed in Ch. 8). Experimental observation of elementary particles relies on detectors. A variety of detecting setups have been designed and optimized over the years, yet in this thesis an extensive overview will be given for semiconductor detectors, based on [22–24], as they will be the main topic of later sections.

5.1 Material properties

Semiconductors are a category of materials that are singled out because of their electrical conductivity characteristics. They are one of the three categories (the other two being conductors and insulators) of materials that are classified based on they way they allow current flow. Conductors are characterized by low resistivity values and allow an electrical current to pass through easily, insulators conversely have high resistivity prohibiting current flow, while semiconductors show both properties at the same time giving them uniform features employable for charged particle detection.

Electrical conductivity is related to the availability of free electrons within a material's basic atom structure. In a single atom, electrons orbit around the nucleus in discrete energy levels. When multiple atoms are in close proximity, as in the case of periodic lattices in crystalline materials, the orbits of electrons in the outer orbits from different atoms overlap. Atomic electrons are bound to obey the Pauli exclusion principle which forbids them to occupy the same energy state. As a result, each atomic orbital splits into discrete molecular orbitals (one for each atom in the lattice), with a distinct energy. Typically the number of atoms in a lattice is quite large and the spacing of the orbitals is so small that can be considered a continuum, referred to as an *energy band*. The lowest energetic energy band is called the *valence band*, while the next higher-lying band is called the *conduction band*, where electrons are free to move. The bands are separated by a barren region called *bandgap* that is free of any electrons. Materials can be categorized based on the spacing of the bandgaps that separates the two energy bands into: *insulators* ($E_{gap} \leq 5\,eV$), *semiconductors* (E_{gap} of a few eV) and *conductors* ($E_{gap} \sim 0\,eV$). In the absence of thermal excitations all the outermost electrons of each atom in the

lattice end up populating the lowest energetically possible band. In the case of insulators and semiconductors (Fig. 5.1) all electrons occupy fully the valence band and need some excitation to make the jump to the conduction band. In conductors on the other hand the two bands are overlapping and the electrons require only minimal energy to start moving in the conduction band.

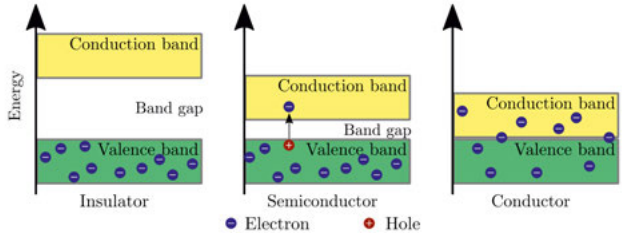

Figure 5.1. The band model of materials. Illustration adapted from [25].

In non-zero thermal conditions, thermal excitations are present and it becomes possible for electrons to jump into the next energy band. When an electron moves from the valence band to the conduction band, it leaves an empty slot (*hole*) in the valence band, which is equivalent to the absence of an electron. Electron and holes are considered *charge carriers* that contribute to a negative and positive (lack of negative) electrical current to their respective bands (conduction band for electrons and valence band for holes). Electrons are typically referred to as *n-type* charge carriers (negative), while holes as *p-type* (positive). They are essentially free particles as they are not associated with a particular lattice location.

The probability of a charge carrier to occupy an energy state is given by the Fermi-Dirac function:

$$F(E) = \frac{1}{1 + exp(\frac{E - E_F}{kT})}, \tag{5.1}$$

where E the energy state level, E_F the energy level at which the occupation probability of a (possible) state is $\frac{1}{2}$ (also called *Fermi energy*), k the Boltzmann constant and T the absolute temperature.

For the case of intrinsic semiconductors (where the lattice atoms are all from the same element) the expression becomes:

$$F_n(E) \simeq exp(-\frac{E - E_F}{kT}) \tag{5.2}$$

for electrons and

$$F_p(E) \simeq exp(\frac{E - E_F}{kT}), \tag{5.3}$$

for holes, since E_F is roughly at the middle of the bandgap.

In thermal equilibrium conditions the concentration of holes in the valence band ($n_{p,i}$) and electrons in the conduction band ($n_{n,i}$) is equal: $n_{p,i} = n_{n,i} = n_i$[1].

[1]The subscript i here underlines that this is true for intrinsic semiconductors

As a reference, the intrinsic carrier concentration in ultrapure silicon at room temperature is approximately $1.45 \cdot 10^{10}\,\mathrm{cm}^{-3}$.

At fixed temperatures it should be noted that the *mass-action* law applies. The law states that the product of the number of electrons in the conduction band and the number of holes in the valence band is constant: $n_{p,i} \cdot n_{n,i} = n_i^2 =$ constant. This applies to all semiconductors, regardless of whether they are intrinsic or not.

In lack of any external fields, the charge carriers move in random thermal motion, scattering on lattice imperfections. A typical mean free path is of the order of a few hundred nanometers. Despite the continuous movement, the overall average displacement of the carriers is zero.

In the presence of an electric field however the carriers are accelerated in their short movement intervals, resulting in a net average velocity (called *drift* velocity). The drift velocity (v_e for electrons and v_p for holes) is dependent on the applied electric field and the so called *mobility* of the carriers (μ_e and μ_p respectively):

$$\mu_n := \frac{-q_e \cdot \tau}{m_n} \tag{5.4}$$

and

$$\mu_p := \frac{q_e \cdot \tau}{m_p} \tag{5.5}$$

where $\pm q_e$ is the electrical charge of the carriers, τ is the mean life time it takes for the carriers to recombine and m is the mass of the carrier.

The relation of the drift velocity and the electric field and mobility is linear when small [2] acceleration fields are applied. In the case of higher fields the relation is no longer linear, while eventually a saturation limit is met and the drift velocities are no longer dependent on the applied field. Electrons and holes hit different saturation velocities. In Si these have been recorded [26] to be of the order of $1 \times 10^7\,\mathrm{cm/s}$ and $8.4 \times 10^6\,\mathrm{cm/s}$ respectively[3], demonstrating a higher maximum value for electrons compared to holes.

The discussed properties of semiconductors can be utilized to compose a detecting system. Assuming a charged particle traverses through a biased intrinsic semiconductor, it will create an electron-hole pair in the material because of ionization. The electrons and holes will start drifting in opposite directions because of the field applied to the device. It is possible to collect the drifting charge carriers at the barriers of the material using electrodes, thus recording a signal that corresponds to the detection of the traversing particle. The described approach is the backbone of semiconductor detectors.

A good detector needs to be able to collect a signal, while keeping the noise levels in the system low. This is commonly known as a large *Signal-to-Noise*

[2] *Small* refers to electric field values that do not affect the mean free time between collisions of the carriers and the impurities in the lattice.

[3] These measurements are for $T = 300\,\mathrm{K}$.

ratio (*SNR*). In the discussed setup a large signal means that the traversing particle ionizes easily the material and creates a large number of electron-hole pairs that are then collected. This is equivalent to a low ionization energy, which implies a small bandgap region. Low noise on the other hand means the lack of intrinsic charge carriers in the material that could be collected as a false signal. This is true in the case of a large bandgap barrier[4]. These contradicting requirements for a good SNR suggest that intrinsic semiconductors are not ideal for detector applications, which lead to the development of doped (*extrinsic*) semiconductors and *pn junctions*.

Extrinsic semiconductors have impurities in their lattice, meaning that some atoms are not from the same kind of material. When the addition of impurities is done purposefully the action is called doping (Fig. 5.2). The dopant elements are normally atoms whose valance shells contain one electron more or less than the atoms of the host crystal. Depending on which dopant is used, the impurity is called an *n-type* (if an element with more valence electrons is used) or *p-type* (if an element with fewer valence electrons is used) impurity. Assuming a silicon host crystal, which has 4 valence electrons, a *p-type* impurity can be introduced if one of the silicon atoms is substituted by a boron or gallium atom (that have three valence electrons), while an *n-type* by a substitution with phosphorus or arsenic (five valence electrons).

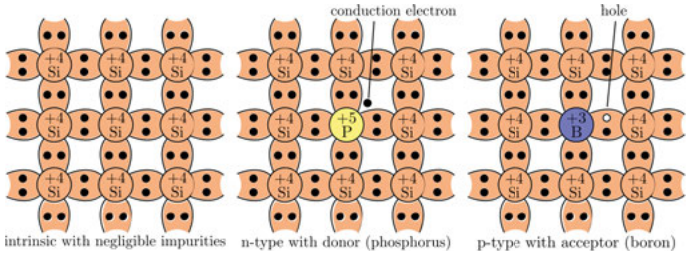

Figure 5.2. Silicon *n-type* and *p-type* doping. Illustration adapted from [27].

The presence of such impurities in a semiconductor changes drastically the behavior of the material as it can introduce a new band into the system (Fig. 5.3). In the case of *n-type* semiconductors the atoms surrounding the impurity atom will form bonds with four out of its five available valence electrons. The remaining electron is not part of the regular lattice and has a weaker bond to the impurity atom. The looser bond allows the electron to occupy a position within the normally forbidden bandgap, forming a new energy band, close to the conduction band. The small energy gap between the new band and the conduction band causes a higher probability for the electron to jump easily to the conduction band, even in low thermal excitations. This results in high (compared to intrinsic semiconductors) concentration of electrons in the con-

[4]Cooling of the structure would also reduce noise, but complicates the setup. The focus here will remain on room-temperature operated setups.

duction band, which increases the rate of recombination and therefore alters the equilibrium between electrons and holes. During this shift the semiconductor needs to follow the mass-action law, ensuring that the carrier density product remains the same as for the intrinsic case. The increase of concentration of electrons in the conduction band therefore results in a decrease of the equilibrium concentration of holes in the valence band. The material is still charge neutral but with higher electrical conductivity that is determined almost exclusively by the flow of electrons, while holes contribute to a much lesser extent. In this case, the electrons are called the *majority carriers*, while holes the *minority carriers*.

In the opposing case of *p-type* semiconductors, the impure atom will not have all the available electrons to bond with its neighbors leaving a bond unsaturated. The place of the unsaturated bond consists a hole in the crystal, which can be filled by electrons. When an electron occupies the place of the hole, while still bound to the location, it is not actually occupying a normal place in the lattice but instead has looser ties. The looser bond allows the electron once again to occupy a position within the normally forbidden bandgap, forming a new energy band, this time close to the valence band. The typical electron-hole pairs that are produced because of thermal excitations in the lattice supply an abundance of available electrons to move to the impurity spots and occupy the place of the holes. This results in a high (compared to intrinsic semiconductors) concentration of holes in the valence band. Once again this enhances the recombination probability between conduction electrons and holes and also decreases the equilibrium number of conduction electrons in order to keep the carrier density product constant. The electrical conductivity of the material is higher compared to the intrinsic case and is determined almost exclusively by the flow of holes, which consist the *majority carriers* in this case, while electrons are the *minority carriers*.

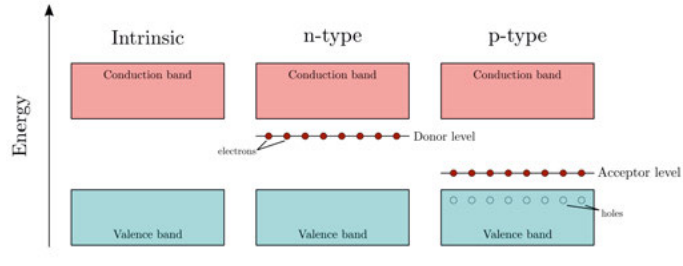

Figure 5.3. Doped semiconductor energy bands. Illustration adapted from [28].

When the two oppositely doped materials are brought together, they consist a *p-n* junction. Each of the two sides has neutral charge and an abundance of available charge carriers that begin to flow towards the opposite side of the junction; electrons flow from the *n-type* side towards the holes of the *p-type* side and vice versa. The movement causes a shift in the electrical charge equi-

librium of the two sides, making the *n-type* side positively charged (because of the additional holes) and the *p-type* side negatively charged (because of the additional electrons). The build up of charge in the two opposing sides causes the formation of an electric field hindering the further flow of the carriers between the two sides. An equilibrium is established when the number of majority carriers on the two sides are equal and the Fermi levels are equated, while no more current flows through the structure. The space between the p-type and n-type semiconductors becomes depleted of charge carriers and is therefore called a *depletion region*.

The built-in potential that is formed in the depletion region, V_d, is expressed through [23]:

$$V_d = \frac{E_{p,i} - E_{n,i}}{q} = \frac{kT}{q} ln \frac{N_p\, N_n}{n_i^2} \tag{5.6}$$

where $E_{p,i}$ and $E_{n,i}$ are the intrinsic Fermi levels of the p-type and n-type regions, while N_p and N_n are the hole and electron charge carrier concentrations in the respective regions.

Typically pn junctions are considered "abrupt junctions" in the sense that the doping type changes over a very small distance compared to the extent (width) of the depletion region. The width of the depleted region can be approximated, under the abrupt junction assumption, by:

$$W_d = \frac{2\varepsilon(N_n + N_p)(V_d - V)}{q\, N_n\, N_p}, \tag{5.7}$$

where ε is the material's dielectric constant and V is the applied voltage.

Eq. 5.7 suggests that a non-uniform electron-hole charge carrier concentration in the junction (i.e., asymmetric doping) creates a larger depletion width in the pn junction. This is a desirable feature in HEP particle detectors, since larger depletion region widths imply a larger active volume, giving higher sensitivity.

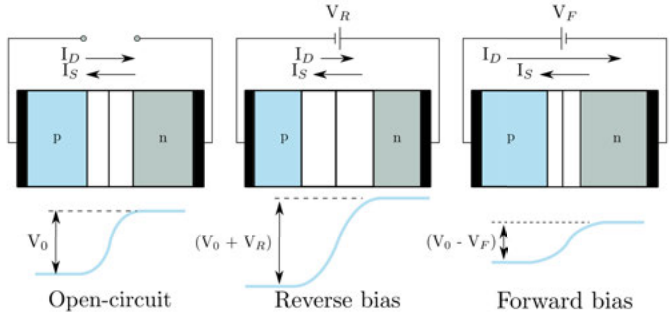

Figure 5.4. pn junction without (*left*), with reverse (*center*) and with forward (*right*) bias. Illustration adapted from [29].

The junction equilibrium changes when an external voltage (forward or reverse) is applied, depending on the polarity of the connections (Fig. 5.4). A

negative polarity on the *n-type* side of the junction and a positive on the *p-type* side is called a *forward bias*. When the polarity is reversed (positive bias on the *n-type* side and negative on the *p-type* side), the biasing of the junction is called a *reverse bias*. The biasing causes a characteristic non-linear current flow through the junction that is distinct between the two biasing configurations (Fig. 5.5).

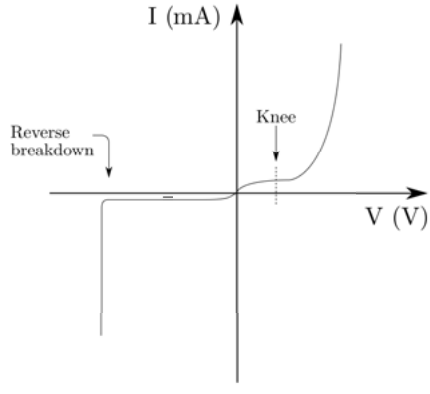

Figure 5.5. Illustration of an IV curve.

A forward bias can supply the charge carriers with the additional energy required to overcome the depletion region and cross to the other side. The negative voltage repels electrons towards the depletion region while providing them the energy to cross over and combine with the holes that are being pushed in the opposite direction towards the junction by the positive voltage. This effectively lessens the width of the depletion region down to a narrow strip, creating a low resistance path allowing high current flow, and decreases the equilibrium voltage across it. This behavior is demonstrated in a characteristics IV curve with close-to-zero current flowing through the junction for biases up to a threshold voltage point, called the "knee", and a subsequent abrupt high current flow that keeps rising with any further increase of the voltage across the junction.

A reverse bias on the other hand suppresses the movement of the charge carriers across the depletion region. The positive voltage on the *n-type* side attracts the electrons on the opposite side of the depletion region while similarly the negative voltage on the *p-type* side attracts the holes. The depletion region consequently becomes wider, creating a higher resistance path hindering the current flow, and increases the voltage across the junction. The characteristic IV curve exhibits a close-to-zero current flowing though the junction for bias values up until a "breakdown" threshold value. Above that point the junction will break down because the high bias values will result in overheating and cause avalanche effect around the junction. This may cause the diode to become shorted and will result in the flow of maximum circuit current.

The behavior of a pn junction in reverse bias acts like an open circuit and it can serve as a suitable device for charged particle detection, similarly to what was discussed for intrinsic semiconductors but with higher signal collection capabilities. During operation of a pn junction in reverse bias no current (in reality only a few micro-Ampere, called *leakage current*) flows through. In the event that a charged particle traverses the structure, it will create electron-hole pairs in the material that will travel towards the areas of the junction that attract them (electrons will move towards the *n-type* side, while holes towards the *p-side*). The movement of the formed carriers in the bandgap will cause a further generation of electron-hole pairs increasing even further the number of collected charge carriers that reach the two sides of the depleted region.

The amount of generated charge in the detector is correlated to the energy loss of the traversing particle in the material, which is given by the Bethe-Bloch formula [30]:

$$-\frac{dE}{dx} = \frac{2\pi n z^2 e^4}{mu^2}\left(\ln\left[\frac{2mu^2 W_m}{I^2(1-\beta^2)}\right] - 2\beta^2 - \delta - U\right) \tag{5.8}$$

where z is the atomic number of the particle, u is its velocity, defined as $u = \beta \times c$ with β being the dimensionless fraction of the velocity with respect to the speed of light (c), m is the electron mass, n the density or electrons per cm^3 of the traversed material, I the mean atom excitation energy in the material, W_m the maximum transferable energy per interaction, δ the density-effect correction and U is a factor that takes into account the non-participation of the inner shell electrons in the interactions.

The charge that is collected from the two terminals indicates the presence of a traversing charged particle that has effectively closed the circuit and its integration over time reflects the accumulated charge deposited in the semiconductor. The measured signal depends on the response of the detector and the attached readout setup the handles the detector output, both which will be discussed further in later sections.

The characteristics of semiconductors, especially in arrangements such as the pn junction, make them excellent choices for detectors. A usual choice for a semiconductor is silicon due to its properties; the most important being its low ionization energy at room temperature (order of a few eV), its high density that results in large energy depositions within the material and its capacity to be easily integrated with electronics. The work presented here is based on silicon semiconductors and all discussed semiconductor structures onwards will be silicon based.

5.2 Detector structures

The development of a detector is typically customized to the needs of the experiments they will be used for and it is a product of many interconnected

factors. The sensor signal efficiency, as it was discussed already, is one of the main driving needs for most cases, but it not the only one. Additional requirements, especially for the case of HEP experiments like the ones discussed in this thesis, are the system's radiation hardness, thermal endurance, complexity of production, cost-efficiency, long-term operation, etc.

A typical application of semiconductor detector structures is in imaging the trajectories of charged particles. Such detector apparatus are commonly called tracking detectors and their operating principle is based on geometric arrangements of semiconductor units that will provide a consecutive list of recorded signals ("hits") when charged particles travel through. Typically tracking detectors are combined with magnetic fields to also extract charge and momentum information. Two very popular silicon semiconductor-based geometry blocks for tracking detectors are the strip and pixel silicon detectors (Fig. 5.6).

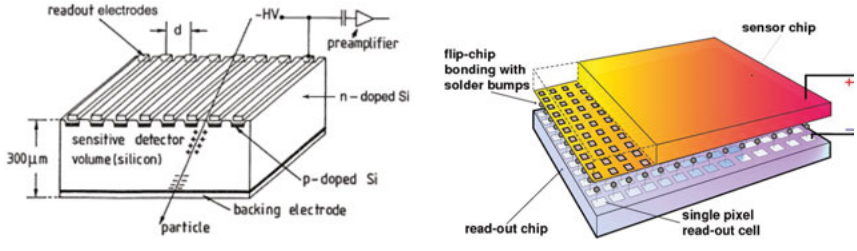

(a) (b)

Figure 5.6. Typical silicon strip (a) [31] and pixel (b) [32] detector anatomy.

Both geometries can provide position information but with different resolutions. The structures are based on common bulk substrate and the implantation of micro-scale dopants to create pn junction elements. Each pn junction is read-out by individual electrodes, constituting a single read-out channel. In the case of strip detectors, the spacing of the implants is done in 1D, running down from one edge to the other as a strip (hence the name), while pixels have a 2D implant spacing in the form of square blocks. The granularity of pixels is much finer and it is preferred over the strips in extremely dense environments where the number of particles hitting a given area simultaneously (hit-occupancy) is expected to be high. The collected charge is read-out as a signal through AC- or DC-coupling of the implants to a metallic layer, which transfers the signal with metallic bonds to the read-out structure. The read-out structure can be either integrated in the silicon structure (monolithic) or part of a distinct structure that is then mounted together with the sensor (hybrid).

5.2.1 Hybrid strip detectors for the ATLAS detector tracker upgrade

Overview

One example of strip detectors, that is of high relevance to the work described in this thesis, are the strip detectors developed for the ATLAS detector tracker upgrade, which will be discussed in more detail in later chapters. They are AC-coupled strip detectors with n-type implants in a p-type silicon bulk (n+-in-p). An illustration of the structure is given in Fig. 5.7.

Their fabrication is based on a single-crystal p-doped wafer that is manufactured using the float zone technology; a method for growing pure silicon monocrystalline materials that is widely used in detector applications [33]. An insulating SiO_2 layer is added to protect the silicon on the wafer on top of its surface. The insulating layer is etched away (photolithography) in places where the other layers need to be attached. Highly doped n-type implants (n+) are added via ion implantation on top of the sensor (only attaching to the etched parts), while a highly doped p-type layer (p+) is added on the bottom to provide an ohmic contact. An isolation layer is also added between the n+ implants to break the ohmic contact between the n+ implants, thus making the strips electrically separated. The readout in these sensors is done capacitively (AC coupled) and is manufactured by interleaving a thin oxide layer between the n+ implants and the metallization layer described below. A metallic layer is added as a final layer on the areas surrounding the n+ implants and the full bottom p+ coated side, to provide the connections for the read-out and biasing respectively.

The biasing is based on a DC path (common bias line) connecting the back and front contacts. The path connects to a ring (bias ring) on the stip side that runs around the structure and connects to each strip through polysilicon bias resistors.

An isolation DC path, referred to as the guard ring, connects one of the n+ implants to the common ground. The guard offers electrical isolation of the active areas from the device edges, thus protecting the detector from potential defect-induced leakage currents in the edges.

As mentioned, the signal is transferred to the metal layer via AC coupling, through the SiO_2 isolation layer. The signal is then transmitted to a hybrid read-out system mounted on the sensor via wire bonding, where Application Specific Integrated Circuits (ASICs) convert the charge from the sensor to a voltage pulse that is amplified, shaped and discriminated into a binary output.

The technical characteristics of the sensor are listed in Appendix A.

Radiation tolerance

These detectors will need to operate under very demanding radiation environments, and their development and later optimization relies on extensive studies on the effects that radiation can have on its performance. Specifically

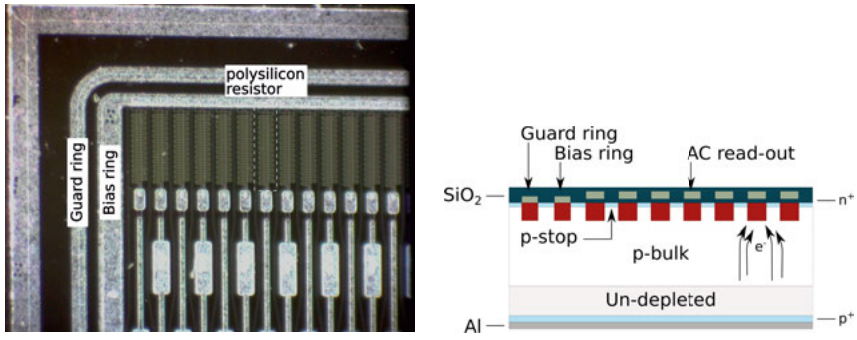

(a) (b)

Figure 5.7. Annotation of sensor parts. A close-up picture of the guard- and bias-ring and polysilicon resistor are showed in (a). A schematic side-view of the same structure is shown in (b).

they will have to demonstrate adequate performance for radiation levels up to $12.2 \times 10^{14}\, n_{eq}\text{cm}^2$ and a total ionizing dose (TID) of $1.5 \times 33.3\,\text{MRad}$ (= 50 MRad) [34]. Problematic effects can occur on both the sensor and the data-acquisition side and the detector design needs to be well-suited for them.

Radiation damages on the sensor side take the form of microscopic damages on the crystal lattice that then demonstrate themselves as macroscopic effects. One such effect is bulk damage, which is when radiation causes the excitation and subsequent displacement of atoms in the lattice. Such a displacement creates pairs of vacancies and displaced atoms that move to other parts of the lattice (interstitials). These can create undesired energy bands in the lattice that act as acceptor centers. A high increase of acceptors in n-type materials can cause type inversion where the bulk changes to p-type. Conversely, semiconductors with p-type bulk do not suffer from type inversion as an increase of acceptors will increase the depletion region.

This type of damage cannot be ignored in cases where it is non-trivial to replace the detector after a few years. A p-type bulk would work best for long-time operations, motivating the choice of semiconductor for the upgraded tracker in ATLAS. The choice of a p-type bulk implies that the implants will be of n-type and the read-out will be based on the collection of electrons. Electrons move faster than holes, offering the additional advantage of faster collection times and fewer trapping effects, resulting to higher signal collection efficiencies than structures that rely on hole collection.

Another radiation-induced sensor effect are surface damages, which are connected to the received TID. The predominant surface damage effect is due to ionizations within the insulating layer. Charge carries created in SiO_2 may never escape the layer, especially holes due to their lower mobility. In the case of a p-type bulk, the applied electric field would cause the holes to move towards the interface with the silicon, gradually building a positively charged

region. The region will start attracting electrons from the other side of the interface, which will increase the capacitive coupling between strips thus increasing the series noise in the detector and increase the signal sharing between readout strips. These two factors together will reduce the single strip SNR which will in turn reduce the single hit efficiency, affecting the tracking performance of the detector.

On the data-acquisition side, radiation can affect electronics that handle the sensor read-out (since they are also semiconductor structures) through cumulative and single-events effects, which are known to affect logic gates, state machines and memory elements. Cumulative effects for electronics inflicted by ionization are grouped together under the term TID effects. The exposure to chronic dose creates trapped charges and interface states in oxides (similarly to what was mentioned for sensors), causing them to lose their electric properties. The problems appear as an increase in the pulses' rise and fall times and the corresponding decrease of their frequency. Mitigation of such errors is possible through shielding and/or changes in the physical design of the used transistors. The single-event effects can be non-destructive ("soft errors"), or permanently damaging ("hard errors"). Soft errors are ofter split into transient (single-event transient or "SET") and static (single-event upset or "SEU") errors. SETs are glitches caused from ionization-induced charges traveling through combinational logic and captured into storage elements, while SEUs are storage element state changes caused by a hit on sensitive nodes (e.g. bit-flip in a memory element). Mitigation techniques for soft-errors include changing the topology of the circuitry or employing a redundant logic (ex. triple modular redundancy) in critical elements.

In the ATLAS strip detector case, this translates to a need to protect configuration registers, state machines and all control information from SEUs and SETs. The read-out ASICs were designed under these considerations, and revisions introducing a highly redundant logic approach and more spaced-out circuit topology made the system more robust.

5.2.2 Monolithic active pixel sensors

Monolithic active pixel sensors (MAPS) [35] are novel detector structures with many advantages to offer. They are growing more popular over the years in large experimental structures, such as the ALICE experiment that will be introduced in the next chapter.

As the name implies, the sensor and the readout electronics are combined in one structure, integrated in the same volume. The typical anatomy of such a detector can be seen in Fig. 5.8. In this structure, traversing charged particles create electron-hole pairs within the thick epitaxial layer. The carriers diffuse in the material until they are collected by the depleted region of a biased diode. The collection time is of the order of 100 ns. Transistors can be

implemented in the well-structure of each pixel which can be used to integrate readout electronics for the signal.

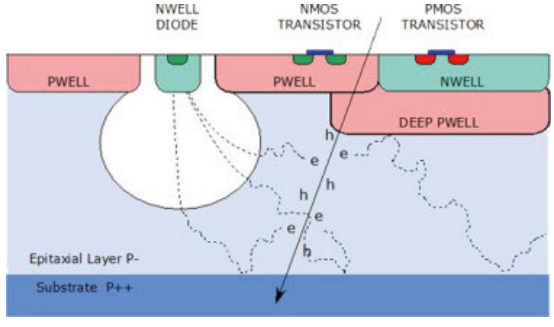

Figure 5.8. Example of a MAPS structure [36]. The illustration shows the collection of electrons created in the depleted region near the collection diode in the thick epitaxial layer of the MAPS detector.

The signal for a crossing ionizing particle is created in a thin epitaxial layer that extends over roughly $10-30\,\mu$m and the generated charge carriers are collected by thermal diffusion within the order of a few 100 ns. Two very compelling advantages of this detector type are its low material budget (thickness in the order of $50\,\mu$m) and its very high intrinsic granularity. Conversely, one can argue in favor of hybrid pixel detectors over the MAPS detectors because of their higher readout speeds and radiation tolerances, since diffusion is severely affected from displacement damages. These arguments, combined with the extensive familiarity with the hybrid pixel detectors performance and challenges, motivate their favoring over the monolithic design.

The high-voltage MAPS (HV-MAPS) technology (Fig. 5.9) [37], that has grown more popular over the years, overcomes the speed concern of simple MAPS. In this design a voltage is applied between the substrate and the deep well that contains the active electronics, leading to the fast charge collection by drifting, and not diffusion as in simple MAPS. The structure thus relies on both low- and high-voltage circuits and a "floating logic" technology is used to ease their interface. The floating logic structure allows the implementation of arbitrary complex CMOS readout circuits inside the deep wells (capable of amplifying and processing the signal).

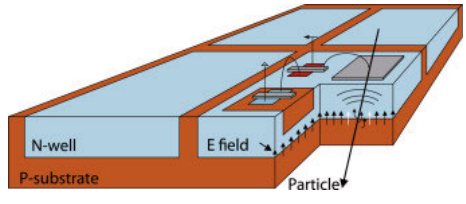

Figure 5.9. Example of a HV-MAPS structure. The figure is also available in [38].

A specific HV-MAPS structure will be discuss here, the MuPix detector [38], which was developed by Heidelberg University for the Mu3e experiment[5] (Fig. 5.10). The detector uses a p-substrate with a deep n-well which acts as the charge collection electrode. Shallow n- and p-wells are created within the n-well, hosting low-biased electronics. The pixel size in the latest version (MuPix10) has a size of $80\,\mu\text{m} \times 80\,\mu\text{m}$. The signal flow from a traversing charged particle starts with the generation of electron-hole-pairs in the pixel diode. The signal is amplified with a PMOS amplifier in the pixel, followed by its transmission to a corresponding readout buffer cell in the periphery of the sensor. The time-over-threshold is recorded for each pulse, as well as its timestamp, offering a times resolution of the order of $\sim 6\,\mu\text{s}$.

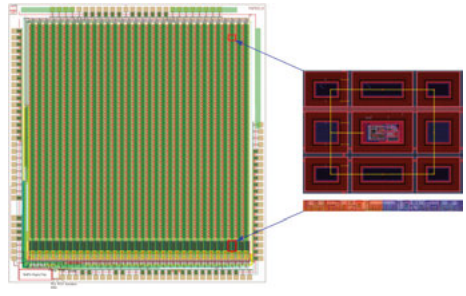

Figure 5.10. Layout of the MuPix-7 pixel and the corresponding electronics in the periphery. Each pixel relies on nine diodes and a set of amplifier electronics in the middle. The figure is also available in [38].

5.3 Detector performance

The main attribute that judges the quality of a detector is its SNR capabilities. The generation of the signal is primarily dependent on the thickness of the depletion zone and on the energy losses of the particle in the material. A good signal collection however requires good and fast charge collection from the detector, as it has been already discussed.

The presence of leakage current in the system is unavoidable as it is caused from random thermal motions of the charge carriers with certain concentration gradients in the doped regions (electrons in the p+ region and holes in the n+ region) that diffuse and drift to the junction and are collected by the electrodes. While the leakage current can not be eliminated completely, it is important that it is kept as low as possible so as to minimize its contamination to the generated current within the sensor (actual signal). The typical I-V behavior from a good sensor is depicted in Fig. 5.5, which, in combination with the

[5]Mu3e is a novel experiment searching for charged lepton flavor violation in the rare decay $\mu^{\rightarrow}e^{+}e^{-}e^{+}$.

expected capacitance-potential (or C-V) behavior of the sensor, specifies an optimal range for bias operation. Other important noise contributions are from the resistors within the detector structure and these are addressed during the design of the detector.

An important feature detector performance for tracking setups is their position resolution. Specifically for the case of strip detectors, the position resolution is affected from both internal physical processes (such as statistical fluctuation of the expected energy loses within the detector and the drifting and diffusion of charge carriers within the junction) and external parameters (such readout structure, the inter-strip distances and the overall achieved SNR). Concerning the drift and diffusion of the charge carriers it is important to note that while the carriers drift towards the electrodes because of the applied field, they also experience diffusion that causes a spread of their distribution. The width of the distribution is primarily affected by the time required to travel towards the electrodes.

The aforementioned parameters are taken into consideration during the design of sensors, yet it is essential that at least some of them are tracked also at later occasions to evaluate if their performance is still intact. This becomes increasingly important in cases where the sensors have to sustain excessive handling after their production. A good example that will be further discussed in later chapters is the case of the ATLAS strip tracker, where the sensors need to stay in storage for extended periods of time, have to undergo assembly procedures for the gluing and bonding of the read-out hybrids as well as extensive testing procedures. In this kind of handling a list of dedicated quality control procedures are set in place to monitor the detector performance, aiming to catch early-on possible defects. A more detailed overview of these tests will be given in later chapters.

Part II:
The Large Hadron Collider and the ATLAS experiment

6. The Large Hadron Collider

The Large Hadron Collider (LHC) [39] is a particle accelerator located in a 27 km underground ring extending between Switzerland and France. The accelerator is part of the larger CERN accelerator complex and was constructed in 2008.

The LHC is a synchrotron accelerator facility designed to fullfil the goals of the physics community in performing precision measurements of established physics processes and exploring new frontiers. Both of these goals presuppose the production of the desired processes experimentally and the accumulation of enough statistics for their study. The event rate of a given process at a collider is determined by its cross-section (through the laws of particle physics), σ_{event}, and the beam collision profile provided by the accelerator complex. The latter is characterised by the parameter of luminosity, L, which is such that the number of events can be expressed as:

$$N_{\text{events}} = L\,\sigma_{\text{event}}. \tag{6.1}$$

The LHC addresses these points by producing high energy counter-rotating beams (beams of proton, lead or xenon), split in distinct bunches, that are steered and collided against one another in designated interaction points (IPs) across the ring. The beams that enter into the LHC ring are gradually accelerated to their final injection energies by an extended accelerator complex where they travel in vacuum to avoid undesirable collisions. The full CERN accelerator complex is illustrated in Fig. 6.1, where the parts relevant for the discussed beam accelerations can be seen. The work presented in this thesis is performed with data collected from collisions with proton beams and thus only those will be discussed.

Proton beams are formed from hydrogen atoms; they are initially striped off of their electrons using an electric field and are then passed through Linac 2 that accelerates them to an energy of 50 MeV. Protons then enter the Proton Synchrotron Booster, a group of four synchrotron rings, that accelerates them to an energy of 1.4 GeV. Thereafter, the protons are directed into a much larger synchrotron structure, called Proton Synchrotron (PS), that has a circumference of roughly 600 m. The PS utilizes 277 electromagnets to steer and accelerate the beam to a final energy of 25 GeV. The protons are then inserted to the Super Proton Synchrotron (SPS) which consists of 1317 conventional electromagnets spread over a 7 km circumference, making it the second-largest machine in the ring. In the SPS, the beams are accelerated to a final energy

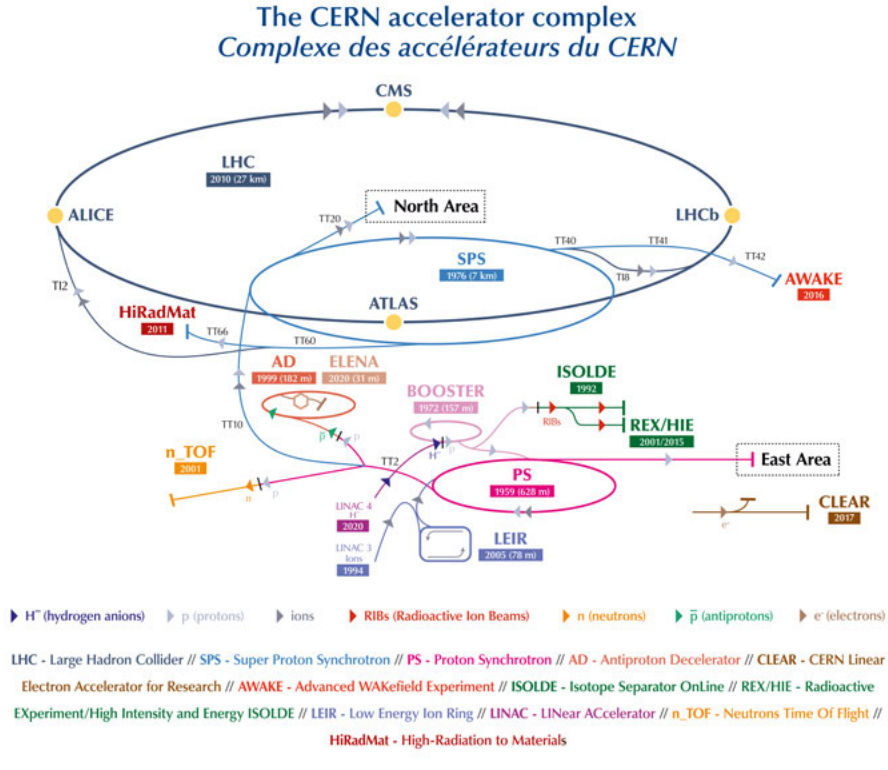

Figure 6.1. The CERN accelerator complex [40].

of 450 GeV. The final step is the injection into the 27 km LHC ring that accelerates the beam to the final 6.5 TeV energy. The ring is also composed of a variety of magnets, each serving a different function, most importantly the bending (dipole magnets) and the focusing (quadropole magnets) of the beam.

There are seven IPs in total along the ring, four of which serve the large particle physics experiment, namely *ATLAS* [41], *CMS* [42], *ALICE* [43] and *LHCb* [44]. ATLAS and CMS are general purpose experiments, aiming to collect a wide range of signals for broad physics studies, ALICE is primarily a heavy-ion detector centered around quark-gluon plasma studies, while LHCb is focused around matter-antimatter asymmetry and b-quark physics. There are additionally three smaller experiments, namely *TOTEM* [45], *LHCf* [46] and *MoEDAL* [47], which are served from the remaining three IPs.

The achieved luminosity from the collisions is a function of many different factors in this process [48]; the number of particles per bunch of each beam (N_b), the number of bunches per beam (n_b), the beam's revolution frequency (f_{rev}), the normalized transverse beam emittance[1] (ε_n), the particles' velocity (through the relativistic gamma factor: $\gamma_r = 1/\sqrt{1-\frac{u^2}{c^2}}$), the $\beta^\star$ function[2] at the IP and the geometrical features of the collision at the IP (affected by the beams' crossing angle, bunch length, etc):

$$L = \frac{N_b^2\, n_b\, f_{rev}\, \gamma_r}{4\,\pi\,\varepsilon_n\,\beta^\star} \times F. \tag{6.2}$$

The factor F expresses the geometric luminosity reduction factor due to e.g. the crossing angle at the IP:

$$F = \frac{1}{\sqrt{1+(\frac{\theta_c\,\sigma_z}{2\,\sigma^\star})^2}}, \tag{6.3}$$

where θ_c is the full beam crossing angle at the IP, σ_z is the root-mean-square bunch length and $\sigma^\star$ is the transverse root-mean-square beam size at the IP.

Physics searches require both high beam energies and high beam intensities. The optimization of the above parameters has allowed increasingly higher luminosity values to be accessible during operation, thus enabling larger datasets to be collected and analyzed. The LHC data taking has been split in distinct periods referred to as *Run 1* (2010-2012) and *Run 2* (2015-2018) periods. The collision energies during Run 1 were initially at 7 TeV and were increased to 8 TeV. During Run 2 the proton beams reached 13 TeV center of mass collision energies, with an instantaneous luminosity of roughly $10^{34}\,\mathrm{cm}^{-2}\mathrm{s}^{-1}$ from

[1] Emittance is a parameter that quantifies the average spread of the bunch particles' distributions in the position-momentum phase space. The normalized emittance is a convenient quantity that encapsulates the decrease of the emittance with increasing beam energy during acceleration.

[2] $\beta^\star$ is a local minimum of the general β function which is related to the beam size along the transverse directions with respect to the beam's trajectory at a given location.

Parameter	Run 2 (Design)
Nominal (proton) energy	6.5 (7) TeV
Nominal (proton) collision energy	13 (14) TeV
Peak luminosity	2.1 (1.0) $\times 10^{34}\,\mathrm{cm}^{-2}\mathrm{s}^{-1}$
$\beta^\star$	$30 \rightarrow 25$ (55) cm
Normalized emittance	1.8 (3.75) μm
Bunch spacing	25 (25) ns
Number of bunches per proton beam	2556 (2808)
Number of protons per bunch	1.2 (1.0) $\times 10^{11}$

Table 6.1. *Proton beam parameters during Run 2 [50, 51]. The respective design parameter values are mentioned in parentheses. During Run 2 $\beta^\star$ had an initial value of* 30 cm *and through levelling techniques reached down to* 25 cm *to enhance luminosity at lower collision intensity.*

bunch crossing collisions every 25 ns. The delivered luminosities to the ATLAS experiment [49] (which is the most relevant for the work presented here) during the two data taking periods were 22.8 fb^{-1} and 156.0 fb^{-1} respectively, resulting in a total of 178.8 fb^{-1}. The main proton beam parameters during Run 2 [50, 51] are summarized in Tab. 6.1.

7. The ATLAS experiment

The ATLAS detector (Fig. 7.1) is one of the two general purpose experiments situated on the LHC ring [41]. It has a cylindrical structure extending 46 m long and 25 m in height, and sits in a cavern 100 m underground.

The detector surrounds the collision point and was designed to achieve an almost hermetic coverage to be able to collect all particles emerging from the collisions. Heavy particles are known to decay quickly, prohibiting their direct detection. This motivates the detecting principle in HEP that relies on accurate identification of particles further down in the decay chain and the construction of a reverse timeline back to the original particles. The final decay products are typically in the form of photons, electrons, muons, etc, and they are detected and identified based on their characteristic interactions with matter and electromagnetic fields.

The detector is composed of sequential cylindrical segments along the same axis as the beam (barrel) and elongated disk structures (end-cap) that are composed of different materials, immersed in magnetic fields provided by solenoid and toroidal magnets. The detector geometry is discussed with respect to a cylindrical coordinate system centered around the IP and parametrized with respect to z, η and ϕ, where z is the beam propagation axis, η is the pseudo-rapidity variable, a different parameterization of the polar angle parameter θ; $\eta = -\ln(\tan(\frac{\theta}{2}))$, and ϕ is the azimuthal angle. The use of the pseudo-rapidity is motivated from the fact that it is a relativistic equivalent of rapidity, y [1]. A commonly used parameter in ATLAS that quantifies the distance between objects in the $\eta - \phi$ plane is ΔR, which is defined as: $\Delta R = \sqrt{(\Delta\Phi)^2 + (\Delta\eta)^2}$.

Starting from closest to the IP and moving outwards along radius, the first detector segment is the Inner Detector (ID) which includes three sub-systems; the pixel detector, the semiconductor tracker (SCT) and the transition radiation tracker (TRT), and is surrounded by a 2 T toroidal magnet. It has a total length of 7 m and a coverage of $|\eta| < 2.5$. The purpose of this section is to reconstruct the trajectory of charged particles. The magnets bend the trajectories of traversing charged particles, while their interaction within the segment provide information on their path. Further out lie two calorimeter detector segments, the purpose of which is to measure the energy of particles. This segment stops most of the particles that travel through it, the exceptions being neutrinos and muons due to their weak interactions, or any other weakly interacting particle

[1] Rapidity, y, is a Lorentz invariant parameter for boosts along the beam axis and is defined with respect to a particle energy, E, and its momentum along the beam axis, p_z, $y = \frac{1}{2} ln(\frac{E+p_z}{E-p_z})$.

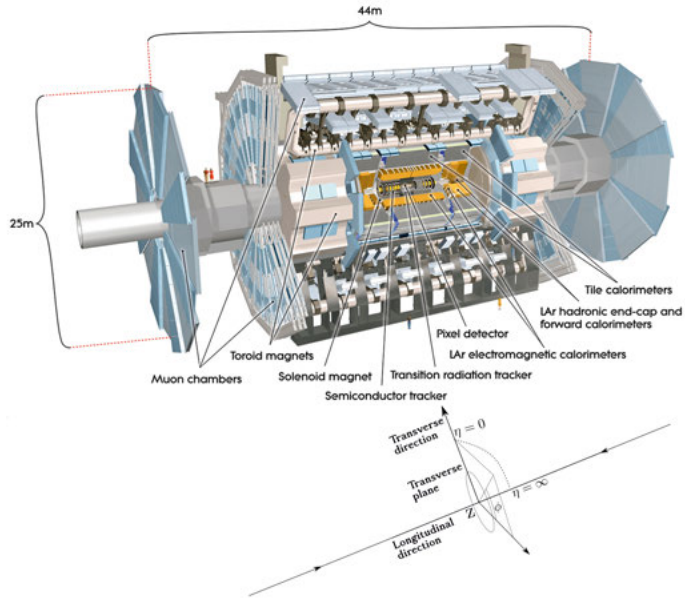

Figure 7.1. Cut-out view of the ATLAS experiment. The z-ϕ-η coordinate system is illustrated on the figure. The figure is adapted from [41].

for that matter. The outermost segment of the ATLAS detector is the muon spectrometer. It is surrounded by toroidal magnets and its purpose is to track and measure the momentum of muons.

The collisions take place at the ATLAS IP at a high pace, with 40 million bunch crossings per second. Each crossing results in number of interactions, pile-up (μ), that is dependent on the accelerator operating conditions (luminosity). The distribution of the mean number of interactions per bunch crossing during different periods of Run 2 is illustrated in Fig. 7.2. This translates into a bombardment of the detector with a vast number of particles in a short period of time, causing a large number of signals in the detector segments. It is not possible, nor desirable, to collect information on all particles from all collisions that pass through, but the goal is rather to ensure the collection of interesting data. ATLAS is relying on a two-level trigger scheme to readout interesting events, while an extended monitoring framework ensures the good quality of the collected data.

The collected data are used for analyses in areas such as SM precision studies or BSM searches. Each study has a dedicated analysis strategy, designed and optimized with respect to the particle content it relies on and the information that is available from the detector after each collision.

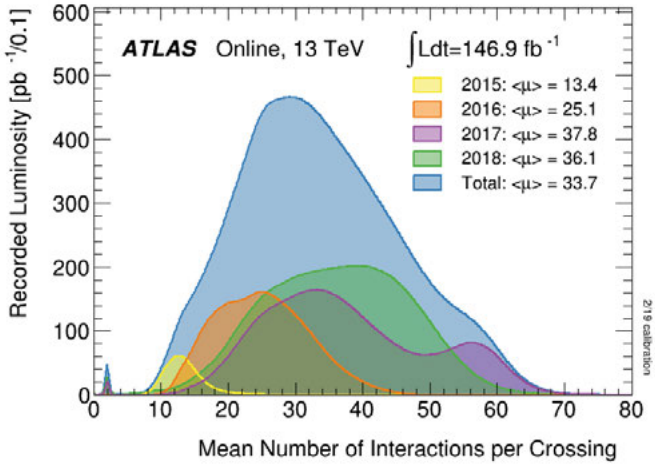

Figure 7.2. The Luminosity-weighted distribution of the mean number of interactions per bunch-crossing in ATLAS during Run 2 [52].

7.1 The inner detector

The purpose of the inner detector (Fig. 7.3) is the tracking of charged particles [53]. This concerns particles such as electrons, muons, protons and charged pions. The detector is composed of three subsections that provide an overall $\eta < 2.5$ coverage.

The innermost part is the pixel detector [53,55,56], extending from a radial distance 50.5 mm to 150 mm with respect to the beamline. The elementary building block of the detector is called a module. It has an area of 10 cm^2 and it consists of a large number of pixel elements, each making up a separate read-out channel, read out in groups by ASICs. The signal is passed on to hybrids and then to separate clock and control integrated circuits. The modules are geometrically placed on the local support structure so that they overlap with one another, ensuring hermetic coverage. They are arranged in four concentric cylinders in the barrel and three disks in the end-cap. The pixel detector holds a total of 80 million pixels (i.e. 80 million channels) and takes up an area of 1.7 m^2. The inner detector is the first detector segment that particles encounter and as such it is the one exposed to the highest radiation damage. This imposes a high radiation tolerance requirement in the materials used and in the readout systems. This is especially true for the pixel detector and it was one of the motivations[2] for including a fourth barrel layer of pixel detectors before the beginning of the Run 2 data taking period. The additional layer is called the Insertable B-Layer, or IBL, [57] and was added on the inner side of the existing layers, closer to the beam axis.

[2]Other principal motivations were the provision of tracking precision, facilitating identification for example of primarily particles containing b-quarks, and tracking robustness.

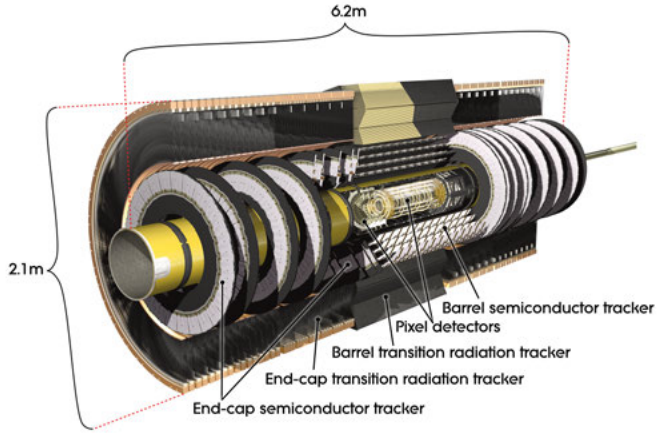

Figure 7.3. Schematic view of the ATLAS Inner Detector [54].

The SCT [53, 58] spans from a radial distance of 299 mm to 560 mm. The modules are based on silicon-strip sensors (285 μm thick high-resistivity n-type bulk silicon with p-type implants) with a hybrid (populated with ASICs) readout system. The modules are arranged in four concentric barrels and two end-cap structures, each with nine disks. The sensor positioning in the modules (two identical sensors glued back-to-back) is chosen to provide two measurements at a stereo angle of 40 mrad, thus allowing the construction of a space-point in the detector system from the measurements. This allows the SCT to provide a minimum of eight strip measurements (four space-points) when a particle originating from the IP traverses the detector.

The outermost part of the inner detector is the TRT [53, 59]. The TRT is a straw tracker and has two different geometrical arrangements of the straws for the barrel and the end-cap. It has the same operating principle as a drift chamber. When a particle passes through it ionizes the gas and the produced electrons are collected from the anode wire, producing a signal. A dedicated readout system performs the signal amplification, shaping, discrimination, and baseline restoration. The straws are made out of carbon-fibre-reinforced kapton and are 4 mm in diameter, with 70 μm walls. A 31 μm diameter gold-plated tungsten wire runs through the center and serves as the ground reference point while the straws are biased at a potential of -1530 V. The barrel section covers a radial area from 560 mm to 1080 mm and the longitudinal region $|z| < 712$ mm, while the end-cap covers the regions $644 < r < 1004$ mm and $827 < |z| < 2744$ mm. The η coverage of the TRT is $|\eta| < 2.0$. The straws are filled with a gas mixture composed of typically Xe, CO_2, and O_2. Xe was chosen due to its high efficiency in detecting transition radiation photons. During Run 2, Ar was used instead of Xe for the cases of large leak modules as a suitable alternative.

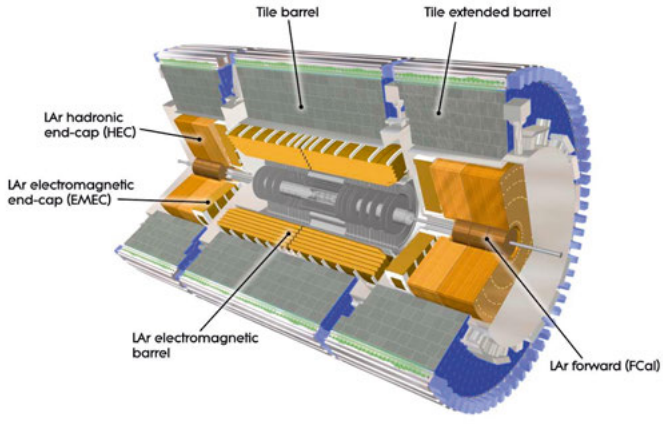

Figure 7.4. Schematic view of the ATLAS Calorimeter Detector [60].

7.2 The calorimeters

Calorimetry is an energy measurement technique that relies on the absorption of a particle's full incident energy. Calorimeters are employed to measure the energies of traversing particles through the collection of the particle showers they create in the material because of their interactions. They are very suitable for HEP experiments due to their good performance for high energies and their fast measurement. They are made from a combination of a dense absorbing element to fully stop the incident particles and an active element that will produce an output signal proportional to the measurement. Depending on whether the absorber and the acting materials are the same or not calorimeters are split into homogeneous (one material) and sampling (different materials). Homogeneous calorimeters are often made with scintillating crystals of high atomic number and density. They are very efficient in measuring charged particles and offer good response linearity across their geometry, but are costly and can be considered limited in their segmentation sampling. Sampling calorimeters are made of high density absorber layers and active readout layers, most commonly in interchanging formation. They are more cost effective and offer transverse and longitudinal segmentation of their readout. A main disadvantage in their design is that they only collect a part of the created shower, making them less precise.

The ATLAS calorimeter system [41], illustrated in Fig. 7.4, is composed of two distinct structures, the electromagnetic (EM) calorimeter and the hadronic (HAD) calorimeter. EM calorimeters measure the energies of particles interacting primarily through the electromagnetic force, while HAD calorimeters target particles that interact mainly through the strong nuclear force. Electrons and photons lose their energy within the EM calorimeter and do not travel further. Charged and neutral hadrons can deposit part of their energy to the EM

calorimeter, but get fully absorbed within the HAD calorimeter. Muons and neutrinos (and possible other weakly interacting particles) propagate through the calorimeters without being absorbed. Muons leave some of their energy in the calorimeters, while neutrinos pass through without interacting.

The EM calorimeter uses a Liquid Argon (LAr) sampling calorimeter that covers $|\eta| < 1.475$ for the barrel region and $1.375 < |\eta| < 3.2$ for the end-cap region. The HAD calorimeter also uses a LAr sampling calorimeter in the end-cap region, covering the range of $1.5 < |\eta| < 3.2$, and a scintillator-steel sampling calorimeter in the barrel region, covering the range $|\eta| < 1.7$.

The LAr calorimeters use a combination of lead, tungsten and copper as an absorber and LAr as their active material. Charged particles and photons passing through LAr ionize the material and the generated charge carriers are collected from electrodes immersed in the liquid. The scintillator-steel sampling calorimeter uses iron as an absorber and scintillating plastic tiles as its active material (justifying the common alternative name of "TileCal"). The passing of a charged particle through the scintillating tiles results in the emission of ultraviolet light that is then collected at the edges of each tile and transported to photomultiplier tubes, using wavelength shifting fibers. The readout of both structures is used as an input to the trigger system (more on Sec. 7.5).

7.3 The muon spectrometer

Spectrometers are scientific instruments used to separate and measure spectral components of a physical phenomenon and have a wide range of applications. The ATLAS muon spectrometer (MS) (Fig. 7.5) is a magnetic spectrometer that utilizes the effect of a constant magnetic field on a travelling charged particle's trajectory, specifically its deflection into a circular path due to the Lorentz force [61]. The radius, r, of the trajectory is correlated to the applied magnetic field, B, and the momentum, p, of the particle through the relation: $r = \frac{p}{q\,B}$, where q is the particle's electric charge.

The MS is the outer part of the detector assembly and aims to detect muons that are expected to have only interacted weakly in the previous detecting layers. It consists of a barrel and two end-cap sections, placed within a magnetic field. The structure is organized into four elements; the Monitoring Drift Tubes (MDT), the Cathode strip Chambers (CSC), the Resistive Plate Chambers (RPC) and the Thin Gap Chambers (TGC), and its goal is to provide tracking and momentum information. All four parts are gaseous detectors and they have specific purposes, the RPCs and TGCs are used for triggering (up to $|\eta| < 2.4$) in the barrel and the end-cap respectively, while the MDTs and the CSCs are used for the precision tracking and momentum measurement of the muons in the principal bending direction of the magnetic fields in the bending plane (up to $|\eta| < 2.7$).

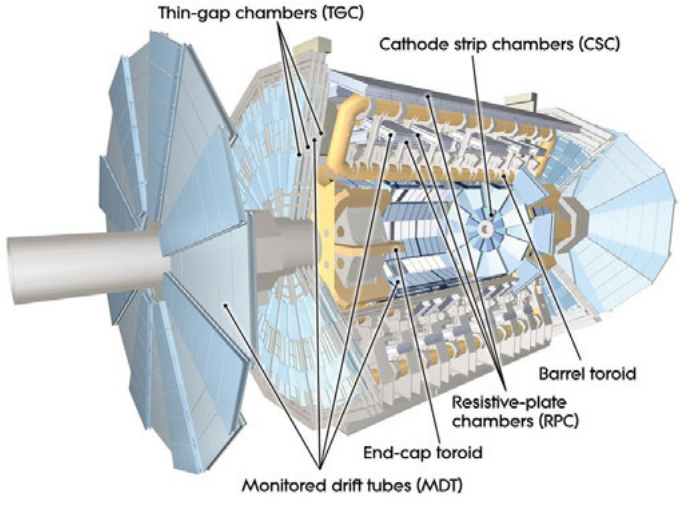

Figure 7.5. Schematic view of the ATLAS Muon Spectrometer Detector [61].

The MDTs are composed of pairs of close-packed multilayers (three or four single planes) of 3 cm diameter cylindrical aluminum drift tubes (12 to 72 tubes per plane). A 50 μm diameter anode wire runs through the tubes, while a mixture of 93% Ar and 7% CO_2 and a few hundred ppm of water vapour fill the tube as the ionization medium. They are placed in two barrel radial and two end-cap parts, except that they are omitted in the innermost ring of the inner station of the end-caps due to high particle fluxes. The MDTs cover an overall range of $|\eta| < 2.7$, except in the inner regions where the coverage is up to $|\eta| < 2$. The CSCs are multi-wire proportional chambers with segmented cathode readout and they are purposed for the precision tracking of the muons in the inner most pseudo-rapidity regions $2 < |\eta| < 2.7$ where the MDTs cannot be used. The RPCs are placed in the barrel and cover the $|\eta| < 1.05$ range, while the TGCs are in the end-cap, covering the range $1.05 < |\eta| < 2.7$.

7.4 The magnets

ATLAS uses four superconducting magnets [41] to provide the magnetic field over the four mentioned detecting layers. This full magnetic system extends 22 m in diameter and 26 m in length, with a stored energy of 1.6 GJ.

The system (illustrated in Fig. 7.6) is composed of one solenoid magnet surrounding the inner detector and three toroid magnets, one in the barrel region and two in the end-caps, for the muon spectrometer. The solenoid is aligned to the beam axis and provides a 2 T axial magnetic field for the tracker. The structure has been optimized to minimize the radiation attenuation before reaching the barrel EM calorimeter. It is composed of a high-strength Al-stabilised

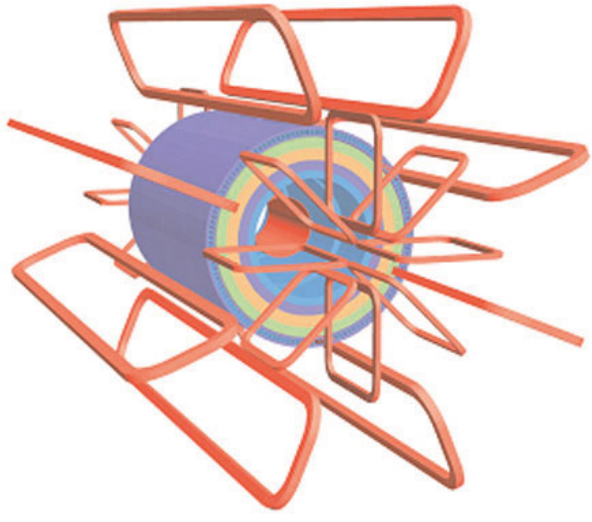

Figure 7.6. Schematic view of the ATLAS toroid magnet system [41]. The red loops correspond to the toroid magnets in end-cap (smaller structures) and barrel (elongated structures). The colorful cylindrical structure corresponds to the TileCal.

NbTi conductor wrapped around a single-layer coil and has an axial length of 5.8 m and inner and outer diameters of 2.46 m and 2.56 m respectively. The barrel toroid delivers approximately 0.5 T and surrounds the calorimeters and its end-cap equivalent structures. It extends at a length of 25.3 m, with inner and outer diameters of 9.4 m and 20.1 m respectively. The end-cap toroids generate a 1 T field and have a length of 5 m and inner and outer diameters of 1.65 m and 10.7 m respectively. The toroid magnets have a pure *Al*-stabilised *Nb*/*Ti*/*Cu* conductor winded around rectangular coils.

7.5 The trigger and data acquisition system

The purpose of the trigger system (Fig. 7.7) is to reduce the incoming 40 MHz rate of events to manageable levels for storage and later analysis [41, 62]. The trigger system in ATLAS is divided in two distinct sub-systems, an initial hardware/firmware-based trigger (referred to as level-1, or L1, trigger) and a subsequent software-based trigger (referred to as high level trigger, or HLT). The L1 and HLT triggers are optimized for specific object identification, as it will be further discussed in Sec. 7.7.

The L1 trigger collects reduced-granularity information from the calorimeters and the muon spectrometer and constructs three types of triggers; the L1Calo, the L1Muon and the L1Topo to identify regions of interest (RoIs) in the event. The L1Calo bases its RoI definition on the energy deposition in

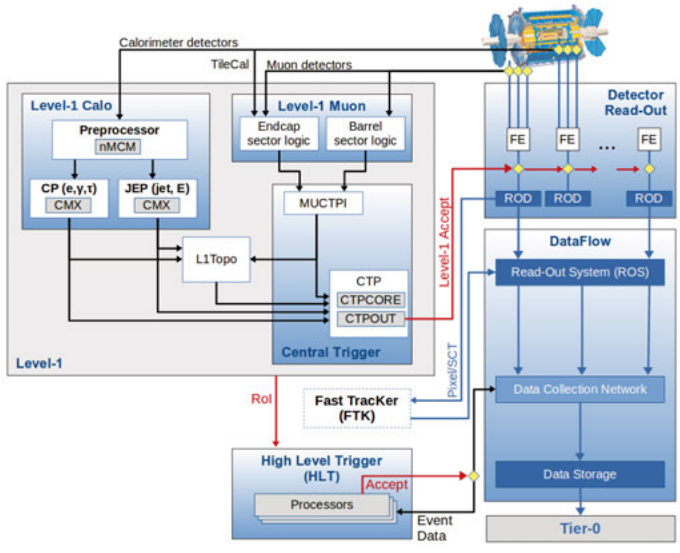

Figure 7.7. Schematic view of the ATLAS TDAQ system [41].

EM and HAD calorimeter cells, searching for local maxima on neighboring $\eta \times \phi$ cells that would indicate a possible core of energy deposition from a traversing particle. The core is typically required to have some isolation requirements around it, i.e. energy deposition below a certain threshold in the cells surrounding the core. The L1Calo is used for triggering on electrons, photons, taus and jets. The L1Muon is focused solely on muon triggering and utilizes the information from the RPCs and the TGCs, requiring spatial and temporal coincidence of the hits. The L1Topo allows the application of topological selections based on object kinematic information and event global quantities that are obtained from the outputs of the two other triggers.

The trigger decision on whether RoIs have been identified in the event is formulated within a 25 ns window at the central trigger processor, using the L1 triggers' outputs. In the case of an identified RoI, an accept signal along with LHC timing information is sent back to the subdetectors for reading out the event. The marked RoIs are forwarded to the HLT at a readout rate of 100 kHz. The HLT uses the full granularity and precision information from the inner detector, the calorimeter and the muon spectrometer to refine the trigger selections and carries out a sequential list of algorithms on the propagated RoIs to further reduce the rates down to 1 kHz. The software algorithms of the HLT are developed from trigger signature groups that focus on the reconstruction of specific physical signals. Examples are jets, missing transverse energy, taus, inner detector tracking, etc. The full workload entails the development of dedicated trigger software for specific detector subsystems and their calibration, performance validation and data quality during online data taking. Offline, the

work expands to the development and calibration of reconstruction algorithms as well as the validation of the reconstructed data.

The available trigger information can determine whether an event hosts a particle of specific interest to an analysis. Usually an analysis requires the presence of one or more particles with certain characteristics in an event to carry out their studies. This can be expressed in the form of a trigger, two examples being a single tau trigger that requires at least one tau with $p_T > 170\,\text{GeV}$, and a di-tau trigger that requires two taus in the event, one with $p_T > 40\,\text{GeV}$ and one with $p_T > 30\,\text{GeV}$. These requirements translate to specific trigger thresholds in the L1 and HLT trigger chains. Events that fire the relevant triggers for an analysis are collected in designated datasets.

7.6 Monte Carlo simulations

Monte Carlo (MC) simulations are computational algorithms used to predict the probability of different outcomes when the intervention of random variables is present and they rely on repeated random sampling to obtain numerical results. They have a wide range of applications and in the context of HEP they address vital needs in the experiments like ATLAS.

Physics searches within ATLAS are conducted based on the detector measurements, which are of the form of voltages, currents, times-stamps, etc. The interpretation of such outputs as particle signatures requires good modeling of the interactions of different produced particles within the material. Additionally one needs to be able to have a reference of the particles that are expected to be produced depending on the processes that occur after each particle collision, the results of which are not deterministic but rather rely on probability distributions.

The main steps of a MC simulation are mentioned below.

1. The first step (commonly known as "event generation") is the simulation of the collision and its outcome. This means the modelling of the quark and gluon interactions during the beam collisions and the subsequent parton showering, hadronization and decays into stable particles. The quark and gluon interactions are modeled using the parton model, where it is essentially assumed that they exist in asymptotic freedom within the proton [63]. Parton distribution functions are used to model the partons' initial momentum within the proton and the energy of the hard-scatter collision, based on quantum field theory.
2. Next is the particle tracking and detector simulation of each of the produced particles with the materials in the detector. This can be performed using for example the Geant-4 framework for a full simulation or by simulating the energy smearing for a rougher estimation, as its common in fast simulations.

3. Finally, the last step is the "digitization" of the energy deposited in the sensitive regions of the detector into voltages and currents to emulate the detector readout.

For each of the simulated hard-scattering events, it is necessary to account for the full number of expected interactions. This is addressed by assigning a pile-up value to each simulated event by randomly sampling the distribution of mean number of interactions for the relevant data-taking period.

The three steps create a simulation output that is similar to that obtained from real data. This allows, at first stage, good modeling of the detector performance and, most importantly, comparative studies between theoretical expectations on physics processes and reality (experimental observations) that make it possible to motivate any scientific result. The described simulation chain is integrated into the ATLAS software framework, Athena [64].

7.7 Object reconstruction and identification

As already mentioned the interpretation of detector measurements as particle signals is non-trivial and it relies on particle reconstruction and identification. The reconstruction and identification are in essence the reversing of electrical signals back to particles and it is a process that relies heavily on the MC simulations mentioned earlier. The procedures are performed with offline algorithms on all trigger-selected events and those produced from MC. The analysis looks the same for both real and simulated events but in MC generated events (the "truth") are available along side the reconstructed object, which is essential for the optimization of the employed algorithms.

The reconstruction is performed for each particle object individually, as it will be described in the following sections, using the same available trigger-level information. Overlaps of objects that could be potentially originating from more than one object are removed at the analysis level.

In the following, a short overview of the trigger-level selections for each object will be given, followed by the dedicated offline reconstruction and identification procedures in each case.

7.7.1 Tracks and vertices

Charged particles interact with the ID and potentially (in case of muons) the MS detector layers, allowing the extraction of information on their tracks. The focus here will be on the ID tracks, while the latter will be discussed in Sec. 7.7.3.

Track reconstruction follows linearly the steps of cluster identification, space-point definition and finally track formation. At an initial stage, clusters are defined based on pixel and SCT information using a connected-component analysis and are used to construct space-points in the detector system. Track

seeds are formed from sets of three space-points. A combinatorial Kalman filter is then used to build track candidates based on the chosen seeds, by adding compatible space-points from the pixel and SCT subsystems with respect to the preliminary trajectory. Ambiguities are resolved using a global χ^2 fit algorithm. Tracks are scored and assessed based on their fit quality, shared clusters and number of holes in their definitions. Those that successfully pass the quality requirements are extended to the TRT system and refit.

The final track candidates are characterized by the best-fit parameters of

- q/p_T: the ratio of the electric charge over the transverse momentum associated to the track,
- η_0: the pseudorapidity of the track,
- ϕ_0: the azimuthal angle at the track's closest distance from the beam line,
- d_0: the impact parameter with respect to the transverse plane and
- z_0: the impact parameter with respect to the longitudinal plane (closest approach to the beam line).

Reconstructed tracks are used to identify vertices in the detector. A seed vertex is first identified based on the maximum of the tracks' z_0 distributions. Tracks are associated with a vertex if they satisty a $d_0/\sigma(d_0) < 7$ and the vertex with the maximal sum of tracks' p_T^2 is named the primary vertex (PV) of the event.

7.7.2 Electrons and photons

The selection of electron- and photon-like events at trigger-level online (i.e. during data taking) [65] relies on the formation of L1Calo EM clusters that seed the RoIs used at the HLT.

The cluster definition within the EM and HAD calorimeters is performed using a 4×4 trigger tower sliding window, corresponding to a $\Delta\eta \times \Delta\Phi = 0.4 \times 0.4$ region, across the full range of the system. A core is singled out as a local maximum of deposited energy, surrounded by an isolation region (Fig. 7.8). The isolation region extends around the core region and is required to have a deposited energy below a certain threshold. The minimum threshold requirements on the core region are dependent on the η region, to account for different energy responses. A veto requirement on the maximum allowed deposited energy in the HAD calorimeter region behind the identified cluster is also enforced, to separate electron/photon candidates from hadrons.

The HLT algorithms of the seeded L1Calo-based RoIs are divided in fast and precise sequences. The fast sequences are designed to discard events early on, while the precise algorithms aim to distinguish between electrons and photons. The distinction between electrons and photons is carried out using track information with $p_T > 1\,\text{GeV}$ associated with the candidate's L1Calo cluster within a $\Delta\eta < 0.2$ region. The precision algorithms for photons are cut-

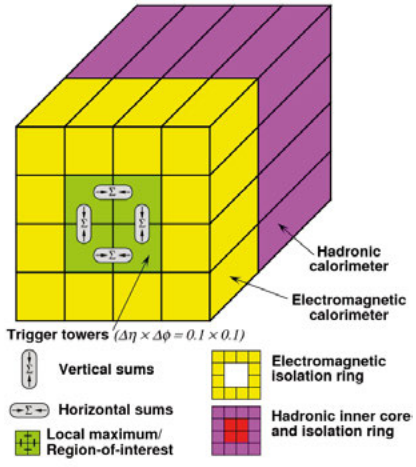

Figure 7.8. Illustration of the core and isolation region definitions in the EM and HAD calorimeters [66].

based, requiring sequential criteria on selected variables, while for electrons they are likelihood-based, where multivariate analysis (MVA) techniques are evaluating electron properties by comparing signal and background probability distribution functions (PDFs) of a list of selected discriminating variables. Depending on the requirements enforced in the precision algorithms the candidates (electrons/photons) are identified as Loose, Medium or Tight. Isolation is also enforced on the candidates based on track and calorimeter information for the electrons and calorimeter-only for the photons.

Offline, the collected data are examined again to proceed to their reconstruction and identification [67, 68]. In the offline reconstruction, the cluster definition within the EM and HAD calorimeters is performed using a 3×5 tower sliding window in η, ϕ, in steps of 0.025 in either direction. Clusters are identified if the summed transverse energy exceeds 2.5 GeV. In case of a clusters' overlap within a $\Delta\eta \times \Delta\Phi = 5 \times 9$, the cluster that prevails is the one with the highest transverse energy, if its E_T is higher by at least 10%, or the one with the highest E_T central tower, otherwise.

The defined clusters act as seeds for the rest of the reconstruction. The EM clusters are attempted to be matched to one of the identified tracks with $p_T > 0.4$ GeV. The matching requires a geometric overlap of the track, when extrapolated to the EM section, within a $|\Delta\eta| \times |\Delta\Phi| < 0.5 \times 0.1$. In the case of multiple tracks matching the cluster, one is selected to be the primary track using information on the angular distance between the tracks and the cluster, the number of hits in the ID pixel and first SCT layers. If no track is matched to the cluster, the object is reconstructed as a photon. On the other hand, if a

matched track is identified, the track is further examined for potential correlations with an additional vertex. If the object-matched track indeed matches also an additional vertex, and has no hits in the pixel layer, it is most likely that it has resulted from a photon conversion ($\gamma \rightarrow e^{-}e^{+}$) and is thus reconstruct as such. A matched track with at least four SCT hits and no correlation with any other vertices is reconstructed as an electron. The curvature of the associated track is also used to determine the charge of the electron candidate. Ambiguities on whether objects are electrons or potential photons are addressed with a final classification where the object's E/p and p_T, secondary-vertex information and number of pixel hits are examined. This is most relevant for photons, as for electrons in the identification step the number of hits in the SCT resolves any such ambiguities.

The identification of electrons is performed with a likelihood function that uses as inputs measurements from the ID, the calorimeters and combinatorial quantities from these two sub-systems. A discriminant is defined based on the likelihoods for a signal ("prompt") electron and background processes[3]. The discriminant serves the purpose of providing different levels of prompt-electron signal efficiencies and corresponding background rejection factors, optimized with respect to E_T and η, and there are four pre-set identification operating points[4]; VeryLoose, Loose, Medium and Tight (Fig. 7.9). Further distinction from background is achieved by isolation requirements around the candidate's signature. For that purpose variables are constructed to quantify the amount of activity close to the candidate. The variables are typically classified as calorimeter- and tracking-based, depending on the measurements they rely on.

Photons are identified using calorimeter information and classify the candidates as Loose or Tight. Similarly to the electron case the two identification levels offer different signal efficiency and background[5] rejection. The isolation is defined based on the transverse energy in a cone with angular size ΔR around the direction of the photon candidate, based on calorimeter- and tracking-based quantities.

Aside from the reconstruction and identification of the candidates it is also essential to quantify the isolation of their signatures. This attribute assists in the further distinction of signatures originating from electrons and photons from background processes.

[3]Background processes in this case are considered signatures from jets that mimic the ones of prompt electrons, electrons that originate from photon conversions or electrons created from the decays of hadrons

[4]In the following the identification classifications will be discussed as "operating" or "working" point interchangeably.

[5]Background signatures in this case are from non-prompt-photons originating from the decay of neutral hadrons in jets, or QCD jets depositing a large energy fraction in the EM calorimeter.

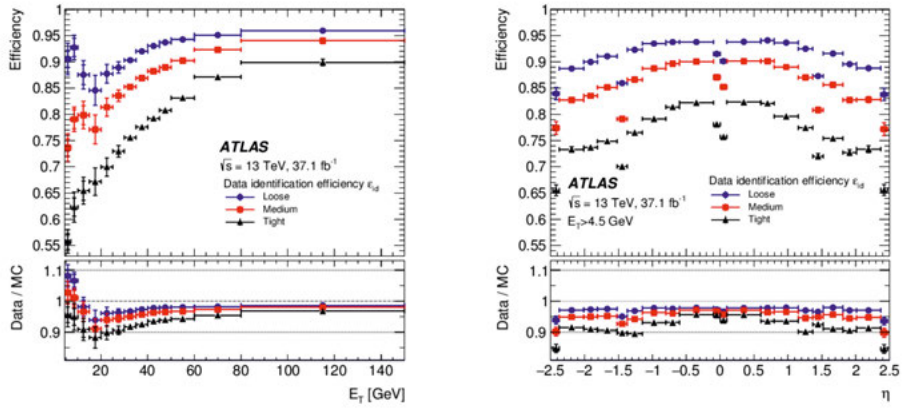

(a) (b)

Figure 7.9. (a) Electron identification efficiencies for Loose (blue circle), Medium (red square) and Tight (black triangle) operating points as a function of E_T (a) and η (b). The calculation is carried out in $Z \rightarrow ee$ samples as outlined in [67]. For both plots, the bottom panel shows the data-to-simulation ratios with statistical and systematic uncertainty.

7.7.3 Muons

At trigger-level the muon identification [69] is based on MS defined RoIs, using the information from the RPCs and the TGCs. The RoIs are determined by constructing a track direction using at least three coincident hits on the inner RPC layers and the outer layers of the TGCs, and any additional coincident hits in the remaining layers. The muon candidates' tracks need to also satisfy a baseline p_T threshold. The momentum estimation is carried out using the degree of deviation from the hit pattern of an infinite momentum assumption.

The RoI is then treated with a fast and a precise muon HLT reconstruction. Similarly to the case of electrons and photons, the fast algorithms aim to discard quickly events that will not satisfy the required criteria. The candidate's track is matched to a track in the inner tracker and its p_T is refined combining the MDTs and CSCs information with the matched inner tracker signature. The subsequent precise algorithms are closer to offline muon reconstruction and are more time consuming, achieving a finer match of the MS-defined candidate with inner detector tracks and its p_T calculation.

Offline, the muons are reconstructed using primarily information from the ID and MS tracking detectors [70]. Calorimeter information is also used in the cases where the reconstruction is based on the MS and there is no track information from the ID. The reconstruction is first performed independently in the ID and MS and then all information is combined to reconstruct the muons.

The track reconstruction in the ID follows the same approach as for any charged particle. In the MS the reconstruction starts with the identification of short track candidates, called segments, reconstructed from hits in each of the MS elements. Segments are identified using a Hough transform [71] and are then combined together into preliminary track candidates. Tracks are reconstructed if the associated hits are satisfactorily fitted using a global χ^2 fit.

At the combination stage, there are four separate muon types defined depending on the sub-detectors used for the reconstruction; combined (CB), segment-tagged (ST), calorimeter-tagged (CT) and extrapolated (ME) muons. In the case of CB muons, a global fit is performed on the separately reconstructed ID and MS tracks. The number of considered MS hits is varied to optimize the fit quality. ST muons are reconstructed based on ID tracks that, once extrapolated to the MS, are associated with at least one local track segment in the MDT or CSC elements of the MS. In the case of CT muons a track in the ID is identified as a muon if it can be matched to an energy deposit in the calorimeter compatible with a minimum-ionizing particle. Finally, ME muons are reconstructed solely from MS tracks, with a very loose requirement on originating from the IP. In the case where two reconstructed types share the same ID track, CB muons are prioritized, with ST following next and CT muons last. If an overlap with ME muons occurs, the track with better fit quality and larger number of hits is selected.

Similarly to the cases of electrons and photons, identification and isolation requirements are imposed to reduce the contamination from background processes, which in this case are expected to be originating from pion and kaon decays. Background signatures are expected to have poorer fit quality in the combined track and incompatibilities between the momentum measurements in the ID and MS. Four standard identification types are designed, Loose, Medium, Tight and High-p_T, based on discriminating variables that can distinguish between signal and non-signal muons. An example of the muon reconstruction and identification performance is shown in Fig. 7.10.

7.7.4 Jets

Jets are cone-shaped hadronic showers that are generated from a number of underlying sources, such as quarks, gluons, hadronically-decaying boosted $W^{\pm}$, Z bosons, etc, motivating the necessity for distinguishing among them and "tagging" their origin (jet tagging). At trigger-level, their identification starts using L1Calo information for identifying local maxima, above a certain threshold of summed E_T within a central $\Delta\eta \times \Delta\Phi = 0.4 \times 0.4$ region. The formed RoIs are seeded to the HLT, which performs a sequence of algorithms in two stages. The first stage concerns the calculation of the jet energy and position through an iterative procedure, identifying topologically

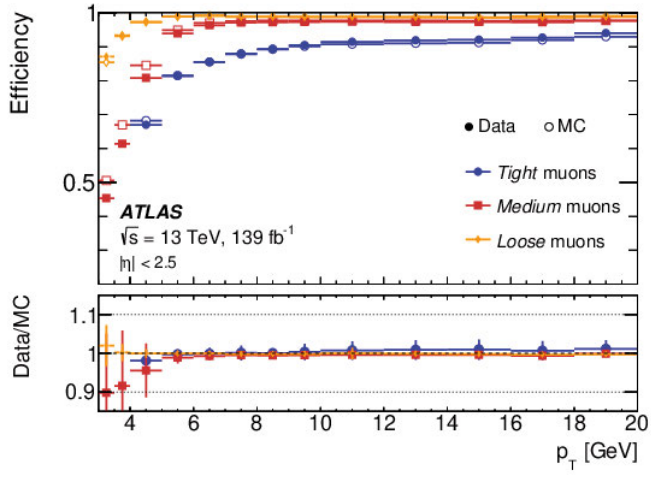

Figure 7.10. Muon reconstruction and identification efficiencies for Loose (orange triangle), Medium (red square) and Tight (blue circle) operating points as a function of p_T. The calculation is carried out in $J/\psi \to \mu\mu$ samples as outlined in [72]. The bottom panel shows the data-to-simulation ratios with statistical and systematic uncertainty.

clustered calorimeter cells, topo-clusters, in the EM and HAD calorimeters. The topo-clusters are reconstructed from the combination of neighboring cells that have an energy deposition above a predefined threshold. The addition of secondary and tertiary neighboring cells is also allowed if the cell energies are high enough.

Once the topo-clusters have been defined, they are used as an input to the anti-k_t [73] jet reconstruction algorithm for the formation of calorimeter jets. Subsequently, an energy calibration is performed to restore the correct jet energy scale (JES), as well as a direction recalculation, pointing at the hard-scatter primary vertex of the jet.

Offline, the jet identification is based on the anti-k_t algorithm with a nominal[6] distance parameter $R = 0.4$, which uses information from the calorimeter and ID systems or a combination of both for the reconstruction [74]. In the majority of the cases the algorithm needs to rely on calorimeter information to identify the jets, "calorimeter jets", because of wider η coverage. The inputs for calorimeter jets reconstruction are the topo-clusters which are defined with a clustering algorithm [75]. The clustering is performed starting from seed cells that have energies above a predefined threshold[7], with iterative addition

[6] In the case of very energetic particles, the jets that are produced during their decay can be spatially overlapping. These are captured as one "large-R" jet, using a distance parameter of $R = 1.0$.

[7] The threshold is defined to be four times higher than the total noise in the calorimeter cells.

of neighboring cells if they satisfy relevant threshold requirements (similarly to the trigger-level case).

The jet candidates at this stage need to undergo additional steps that correct and recalibrate them. The jets are initially reconstructed to point to the center of the detector and therefore an origin correction is applied to the four-momentum of the jet to point to the hard-scatter PV. The measured jet transverse momentum is highly biased by pile-up and a correction procedure is applied to address this, based on the jet average energy density and area. An additional calibration is introduced to account for differences in the calorimeter energy response and granularity. This is done as jet energy and η calibrations to correct the reconstructed jet to the particle-level energy scale and are performed in MC. Dependencies of the jet response on the flavour of the initiated-jet parton are addressed with the so-called global sequential correction (GSC) [76], which is designed to reduce the jet response dependence. Finally, an in situ JES calibration is applied to jets in data to account for differences in jet response between data and MC.

Jets originating from b-quarks can be identified among other jets, because of the b-hadrons long lifetimes and characteristic secondary vertex. A multivariate discriminant combining impact parameter information with the explicit identification of secondary and tertiary vertices within the jet is used to identify the b-quark jets. One of the most widely used MVAs for b-tagging in ATLAS (which is also used in the analysis described in Ch. 10) is the MV2c10 algorithm. Different efficiency working points offer respective rejection efficiencies against c- and light-quark jets (Fig. 7.11).

7.7.5 Taus

Tau leptons are heavier than electrons and muons, making them short lived with a proper decay length of roughly $87\,\mu$m. The identification of taus is solely possible via their decay products. Taus decay with a 35% branching ratio to lighter leptons and a 65% branching ratio to hadrons (dominantly pions) and they are reconstructed using different procedures.

The leptonically-decaying taus produce electrons or muons and neutrinos in the detector, and the electrons/muons are reconstructed and identified following the same procedures mentioned earlier.

The identification of taus in ATLAS is done based on hadronically-decaying taus, using a dedicated trigger and offline reconstruction and identification procedures. At trigger-level [78], the L1Calo trigger seeds the RoI definition, using EM and HAD calorimeter information. Similarly to the described procedure for the electron and photon definition, core and isolation regions are defined for the visible hadronic tau candidate. The E_T of the candidate is defined as the E_T sum in the two most energetic neighboring central towers in the EM calorimeter and in the $\Delta\eta \times \Delta\Phi = 0.2 \times 0.2$ space in the HAD calorime-

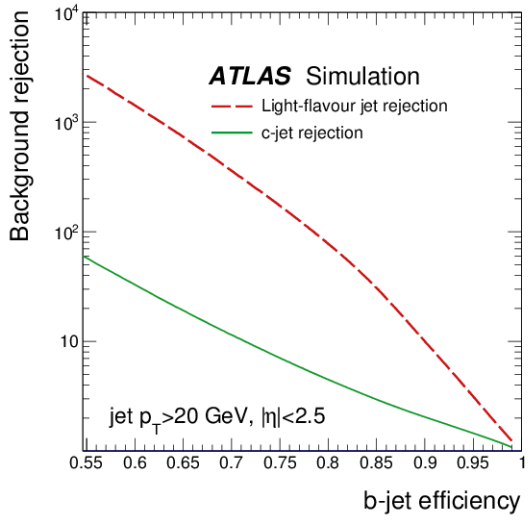

Figure 7.11. Background rejection efficiency of the MV2c10 b-tagging algorithm against c- (green solid line) and light-quark (red dashed line) as a function of the b-tagging efficiency. The performance evaluation is carried on $t\bar{t}$ events as described in [77].

ter. An isolation requirement of energy deposition below $E_T[\text{GeV}]/10+2\,\text{GeV}$ around the core, in an annulus of $0.2 < \Delta R < 0.4$, is required for candidates with $E_T < 60\,\text{GeV}$ to reduce background.

The regions that satisfy these requirements constitute the RoIs that go to the HLT algorithms. The HLT algorithms are applied in increasing order of CPU intensity, optimizing the total processing time. An initial candidate preselection is performed using the RoIs' L1Calo information. The calorimeter clusters of interest are calibrated with a local hadronic calibration and their vectorial sum is used to define a "jet seed". The second HLT step is called Fast Track Finding and it searches for tracks in the inner detector by performing a two-stage pattern recognition algorithm on the "jet-seed". The first stage consists of a scan in a narrow $\Delta R = 0.1$ region around the candidate, along the full length of the considered beamline portion (Z), in search for a lead track. If a lead track is found, a second scan is performed in a larger $\Delta R = 0.4$ cone and narrower Z region around the lead track, in search for additional tracks. The selected candidates pass to the last step of the HLT where precision tracking algorithms are executed. The precise track information is used along with the candidate's calorimeter information for the calculation of a list of input variables to Machine Learning algorithms (Boosted Decision Trees (BDT), or Recurrent Neural Networks (RNN)) trained to produce a visible hadronic tau identification score that is used for the final candidate selection. During the precision tracking stage, the candidate's tracks are counted and are required to be one to three tracks (BDT) or up to three (RNN) depending on the identifi-

cation algorithm. A tau candidate is associated with a "Loose", "Medium" or "Tight" working point, depending on its tau identification score.

Offline, tau reconstruction is performed in stages. It is initially seeded by jets identified with the anti-kt algorithm [79] using $R = 0.4$, that satisfy $p_T > 10\,\text{GeV}$ and $|\eta| < 2.5$. Topological clusters in the calorimeters that fall within $\Delta R < 0.2$ of the seed are used for a preliminary energy calibration. Next, an algorithm is employed to identify the primary vertex corresponding to the tau candidate, tau vertex (TV), using as inputs all the associated tracks within $\Delta R < 0.2$ around the seed direction.

The identification of the TV marks the first milestone and based on that it is possible to determine the candidate's direction, associate more tracks, and construct a tau-centric coordinate system for the definition of relevant variables. The track association is performed by scanning the $\Delta R < 0.2$ region surrounding the seed and selecting tracks that have $p_T > 1\,\text{GeV}$, ≥ 2 hits in the pixel detector and ≥ 7 hits in the pixel and SCT detectors combined and have $|d_0| < 1.0\,\text{mm}$ and $|\Delta z_0 \sin(\theta)| < 1.5\,\text{mm}$, with respect to the TV. Reconstruction of the correct number of tracks means reconstruction of the correct charged particle multiplicity in the tau decay and is thus essential to have high performance in this regard. The reconstruction efficiency is evaluated separately for taus with one and three associated tracks (often abbreviated as 1- and 3-prong respectively). For 1-prong taus the reconstruction efficiency can be affected at high-p_T because of two reasons; higher probability of decay before the pixel layers (without creating any hits in the ID) and higher probability of falsely reconstructing photon-converted electrons as tau candidate. In the 3-prong taus case, at low-p_T the efficiency can be affected by the $p_T > 1\,\text{GeV}$ requirement, while at high-p_T there is a high probability of reconstructing all tracks as one because of collimation.

The identification is performed with an MVA and it is used to discriminate against background, which in this case is pre-dominantly non-tau jets, originating from quarks and gluons. The used MVAs are either BDT [79] or RNN [80] algorithms that use input variables based on ID and calorimeter measurements and are trained separately for 1- and 3-prong. The output is of the form of a discriminant that can provide four identification working points; VeryLoose, Loose, Medium and Tight, in increasing order of background rejection. The performance of the MVAs is presented in Fig. 7.12 and Fig. 7.13.

7.7.6 Missing transverse energy

The collisions at the IP are considered to be in the longitudinal direction, without carrying momentum on the transverse plane. This allows the claim that the momentum in the transverse plane post-collision should sum up to zero due to momentum conservation. Based on this assumption and taking advantage

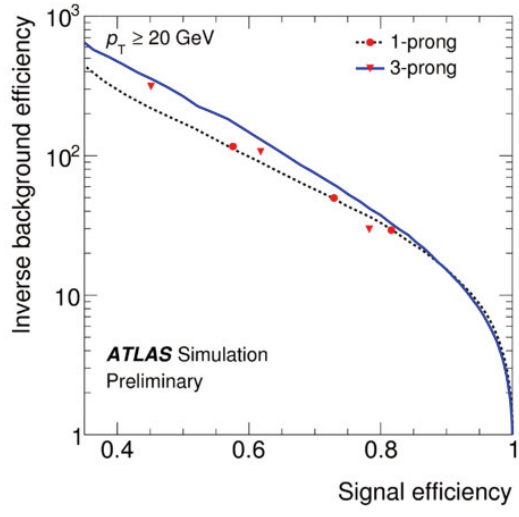

Figure 7.12. Performance of the BDT algorithm in terms of background (quark- and gluon-initiated jets) rejection as a function of the signal efficiency for hadronically-decaying tau candidates ($\tau_{\text{had-vis}}$) with one (solid line and red circles) and three (dashed line and red triangles) associated tracks ("prongs"). The working points (circles/triangles) correspond to the Loose, Medium and Tight identification criteria, in order of ascending background rejection, as they appear from left to right on the figure. The efficiency estimation procedure is described in [79].

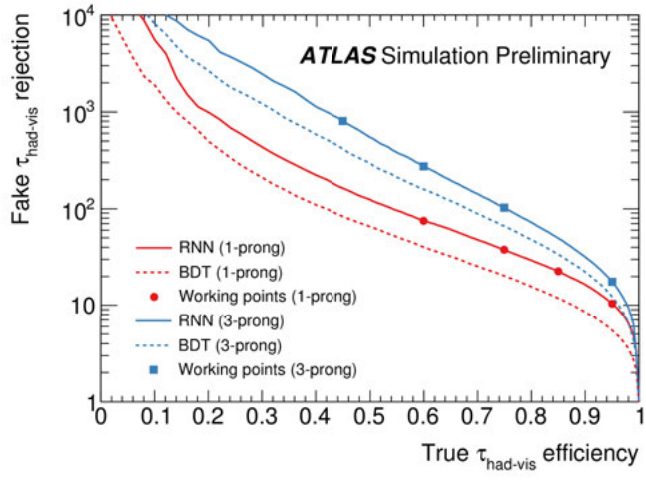

Figure 7.13. Performance of the BDT (dashed) and RNN (solid) algorithms in terms of background (quark- and gluon-initiated jets) rejection as a function of the signal efficiency for hadronically-decaying tau candidates ($\tau_{\text{had-vis}}$) with one (red) and three (blue) associated tracks ("prongs"). The markers indicate the four defined identification working points; VeryLoose, Loose, Medium and Tight, in order of increasing background rejection efficiencies. The figure is also available in [80].

of the hermetic structure of the ATLAS detector it is possible to identify imbalances in the system's reconstructed energy. Any missing transverse energy is attributed to neutrinos that are known to travel through the detector unrecorded, or other weakly interacting particles. The imbalance in momentum in the transverse plane is called missing transverse momentum and is defined by its magnitude (E_T^{miss}) and its azimuthal direction. The E_T^{miss} in the detector is reconstructed as the negative sum of p_T of all other visible objects in the event. It is calculated separately for each of the objects (electron, photon, muon, tau, jets and soft contributions) and for each cartesian (x,y) coordinate. The soft term contribution accounts for tracks or calorimeter deposits that have not been associated with reconstructed objects. Typically it is calculated using track information, because of their robustness against pile-up.

8. Statistical analysis of data

HEP searches can draw meaningful conclusions only after comparisons of the experimentally collected data to the yields and shapes expected from theoretical predictions. A significant deviation between the two could potential be a new discovery, if it is statistically significant.

The comparison between experimental data and theoretical expectations requires a common ground setting. This is addressed by expressing the theoretical expectations in a similar format as that of experimental data through Monte Carlo (MC) simulations, as it was briefly discussed in Sec. 7.6. A short overview of the staging for the data and MC comparison will be presented in Sec. 8.1, which will be followed by a discussion on how one extrapolates results using the method of hypothesis testing in Sec. 8.2.

8.1 Data analysis

Statistical analyses rely on two resources; experimentally obtained datasets, that reflect reality, and simulated distributions and their corresponding uncertainties (statistical or systematic) that express theoretical expectations. Typically these are parametrized with respect to parameters of interest, such as the contribution of an investigated process to the observed measurements (referred to as signal strength, μ), as well as nuisance parameters, θ_i, whose true values, $\theta^{\text{true}} = (\theta_1^{\text{true}}, \theta_2^{\text{true}}, ..., \theta_{\text{p}}^{\text{true}})$, are unknown and they are determined from fits to the data. The objective of a data analysis is to estimate the parameters of interest (eg. μ in this context) and the values of each of the θ_i^{true} parameters. This is achieved by examining the data samples through discriminating parameters that are suitable for the study at hand. A function is used to fit the data in that binning and the parameters of the best fit act as estimators for the determination of μ and the θ parameters.

There are different ways to identify a good estimator. Two popular methods are the maximum likelihood (ML) and the chi-squared (χ^2) methods. The ML method is thoroughly used in HEP experiments and will be outlined a bit further.

All events that are produced in the detector are considered to be independent from one another. Assuming that the discussed theoretical predictions, that depend on the parameters θ, are of the form $f(x;\theta)$, where x reflects an observed value, and building on the independence of the events, it is straightforward to state that the probability of observing a measurement x, given a

certain θ is: $P(x;\theta) = \Pi_i(f(x_i;\theta))$, where i ranges over all events. Once data measurements have been collected, x is replaced by the measurement values x_0 and the probability is no longer a probability distribution function, but consists what is known as a likelihood function: $L(\theta) = P(x_0;\theta)$.

Circling back to the estimators that are of interest to be identified, the principle of maximum likelihood states that the maximum likelihood estimator $\langle\theta\rangle$ is the value of θ for which the likelihood L becomes maximum. In practice this is equivalent to maximizing a parameter λ, defined as:

$$\lambda(\mu) = \frac{L(\mu, \hat{\theta}(\mu))}{L(\hat{\mu}, \hat{\theta})}, \tag{8.1}$$

called profile likelihood ratio, where μ is the signal strength, $\hat{\mu}$ is the maximum likelihood estimator of μ, $\hat{\theta}$ is the maximum likelihood estimator of θ overall and $\hat{\theta}(\mu)$ is the conditional maximum likelihood estimator of θ for a signal strength μ. In this parametrization it is possible to see the correlation of the optimal fit for the θ parameters to the examined signal strength.

The defined profile likelihood ratio, or in some cases a function q of the parameter:

$$q = -2\ln(\lambda(\mu)), \tag{8.2}$$

serves as a suitable test statistic for determining whether experimental data support a given theory or not within the scope of hypothesis testing, as it will be discussed in the following section.

8.2 Hypothesis testing

Hypothesis testing is a commonly used tool for deciphering collected experimental data. The method relies on the formulation of hypotheses that are then tested based on experimental observations. In the context of HEP studies described in this thesis, a null, $H0$, hypothesis can be formed stating that the collected data are compatible with SM-only interactions (which is also referred to as a background-only hypothesis), while an alternative, $H1$, hypothesis could on the other hand state that the observations also include contributions from a specific BSM scenario (also referred to as a signal-plus-background hypothesis). Once the null and alternative hypotheses have been defined, hypothesis testing addresses the questions of whether experimental findings are compatible with $H0$ or if it could be rejected based on these findings.

The studies are typically carried out in dedicated regions, referred to as control (CR) and signal regions (SR) that are defined using discriminating parameters which are considered sensitive in distinguishing between $H0$ and $H1$. CRs are defined to evaluate the analysis approach in a 9parameter space where no $H1$ events are expected to occur, while SRs are chosen to maximize the possibility of observing a deviation from the $H0$ expectations.

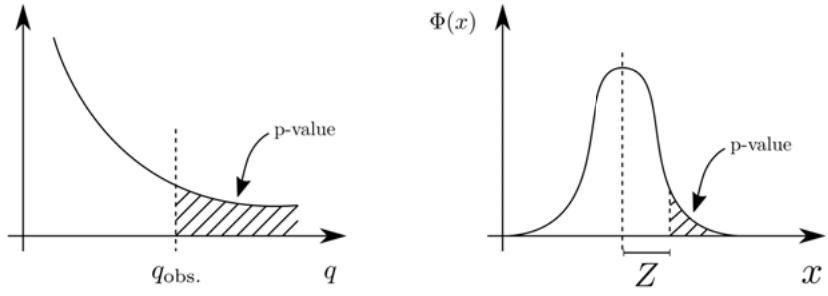

Figure 8.1. Illustration of the relation between the p-value obtained from an observed value of the test statistic q (left) and the standard normal distribution $\Phi(x)$ showing the relation between the significance Z and the p-value (right).

The collected measurements are compared to the theoretical expectations of each hypothesis through a common parameter, m, defined as a correlation of the expected events from $H0$, b, and $H1$, s: $m = b + \mu \cdot s$, where μ is the aforementioned signal strength. If $H0$ is true, μ will be 0, while if $H1$ holds, μ will be 1.

The evaluation of the data agreement to each of the considered hypotheses is done with the computation of the probability, under assumption of a hypothesis H, of finding data of equal or greater incompatibility with the predictions of H. This is encapsulated in the p-value parameter:

$$p = \int_{q_{\text{obs.}}}^{\infty} f(q|q_{\text{obs.}})\, dq, \tag{8.3}$$

where $q_{\text{obs.}}$ is the observed value of the test statistic and $f(q|q_{\text{obs.}})$ is the distribution of the test statistic in data. Incompatibility in this context means a p-value lower than a pre-defined threshold or, in other words, a low probability of observing a test statistic value of $q_{\text{obs.}}$ (or higher) in the data. In HEP it is most common to perform the same type of hypothesis testing using the concept of equivalent significance, Z. Assuming a Gaussian distribution of a variable, Z is defined as the number of standard deviations above the distribution's mean that will result in an upper-tail probability (area) equal to the p-value. Z is parametrized as:

$$Z = \Phi^{-1}(1 - \text{p value}), \tag{8.4}$$

where Φ^{-1} is the quantile (inverse of the cumulative distribution) of the Gaussian distribution. The described concepts are illustrated in Fig. 8.1.

There are two important error classifications that come into play during hypothesis testing that need to be accounted for; false rejection of a true null hypothesis (classified as Type-I) and failure to reject a false null hypothesis (classified as Type-II). The Type-I error is also referred to as the size of the

test, α, and is the main parameter used for the quantification of the test statistic decision. An examined statistical significance is established when the p-value of a hypothesis is less than the test size α [81], as this implies that the hypothesis is rejected with a probability of 1-p.

Based on the described concepts one can examine the results for a discovery, where the objective is to reject the background-only hypothesis, or evaluate the confidence level at excluding a signal hypothesis [82]. For a discovery claim one in principle tests the $\mu = 0$ hypothesis, assuming that $\mu \geq 0$ and the test statistic in this case is defined as:

$$q = \begin{cases} -2ln(\lambda(\mu = 0)), & \hat{\mu} \geq 0 \\ 0, & \hat{\mu} < 0 \end{cases} . \tag{8.5}$$

Lack of agreement with the background-only hypothesis is considered only if $\hat{\mu} \geq 0$. Deviations in $\hat{\mu} \leq 0$ are not attributed to the signal process, but rather statistical errors and are accounted for in the nuisance parameters. To ensure high-confidence in the claim α (i.e. the p-value) is required to be less than 2.87×10^{-7}, which in turn means a $Z = 5$ statistical significance.

If such a deviation is not encountered, $H0$ cannot be rejected, and exclusion limits are set instead on the signal strength. In this case one examines the compatibility of the signal strength, μ, with the observed data. One way to evaluate this is by defining the test statistic as:

$$q = \begin{cases} -2ln(\lambda(\mu)), & \hat{\mu} \leq \mu \\ 0, & \hat{\mu} > \mu \end{cases} , \tag{8.6}$$

where one can see that the statistics' values grow larger with higher discrepancies of expectations and observations. Here, $q = 0$ for $\hat{\mu} \geq \mu$ as any deviations in that regime cannot justify any claim on incompatibility with the data. This can be limiting in the exclusions, as one can derive limits even in cases where the signal is not expected to be evident.

A more prudent approach is to do the evaluation using the modified frequentist's approach. The discriminating parameter in this case is the CL_s confidence level, defined as:

$$CL_s = \frac{\text{p-value}_{H1}}{1 - \text{p-value}_{H0}}. \tag{8.7}$$

This definition normalizes the p-value confidence level expected from the $H1$ hypothesis to that expected from $H0$. thus avoiding the exclusion of hypotheses when there is no sensitivity. Typically signal exclusion limits are examined at a 95% confidence level, meaning that α (i.e. the CL_s value) is required to be less than 0.05. The CLs method is also employed for the results of the analysis described in Ch. 10.

Part III:
Tau lepton based analyses

9. Fake τs; the Fake Factor method and building towards a universal fake τ estimation approach within ATLAS

Tau leptons, and specifically their hadronic decays, are interesting signatures in many important SM measurements and BSM searches. The hadronic τ signature, $\tau_{\text{had-vis}}$, relies on the identification of the visible products of the decay, which contains one (72%) or three (22%) charged pions and at least one neutral pion in 68% of the cases. Pions appear as collimated hadronic jets in the detector, which introduces the challenge of differentiating them from non-τ hadronic jets (Fig. 9.1).

The main background for hadronic τs are quark- or gluon-initiated jets, as they both produce particle showers in the electromagnetic and hadronic calorimeters. The main distinctions between the two are the deposited energy fraction in the EM calorimeter (larger for τs because of the produced neutral pions that later decay to photons during their cascade decays) and their collimation structure (narrower for τ-initiated jets), which motivate the τ identification requirements outlined in Sec. 7.7.5.

Even with this requirement however it is known that several non-τ jets pass the τ selection requirements of SRs in analyses, faking the τs that the analyses rely on. This is addressed with various techniques in order to estimate accurately the spectra of fake τs that sneak into the SR of interest. The employed techniques rely mostly on data, since MC simulations are not reliable enough for these studies. One of the most common techniques used is the Fake Factor (FF) method, discussed further in the text.

The popularity of hadronic τ jets in analyses searches and the associated need to estimate the fake τ contamination in the analysis SR have given rise

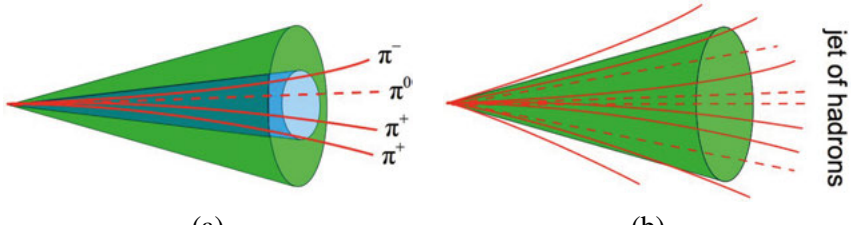

Figure 9.1. Typical signatures of hadronic (a) τs and (b) QCD jets in the ATLAS Calorimeter.

to a motion within ATLAS to develop a uniform method for the application of these techniques. The Fake Tau Task Force (FTTF) was initiated in 2018 and has as its main mandate to provide common methods, components and tools for the determination of the fake-τ background due to misidentified jets. The goal is to develop a universal method of determining fake τs and associated systematic uncertainties through a dedicated tool (Tau Fake Factor Tool or TFFT).

The present focus of the FTTF is to prepare the tool for the FF method, such that analyses will be able to use the tool to derive the FFs that apply to their specific SRs.

This chapter gives an overview of the FF method (Sec. 9.1) and the main principles employed for the universal fake τ treatment approach (Sec. 9.2). A brief mention on the FTTF tool is given in Sec. 9.3 and lastly an overview of the MC studies needed for the FF tool is given in Sec. 9.4.

9.1 The Fake Factor method

Typically MC simulations cannot give an accurate representation of the non-τ jets faking the signatures of true τ candidates. The FF method is a widely used technique for the modeling of this type of background. The method relies on the assumption that the probability of a jet to be misidentified as a $\tau_{\text{had-vis}}$ is a general property of the jet. Under this assumption it follows that the ratio of the number of non-τ jets that manage to pass the $\tau_{\text{had-vis}}$ identification criteria over the number of those that fail them is something that characterizes jets of specific dispositions (p_T, η, number of associated tracks, origin, etc). The FF is defined as this ratio:

$$\text{FF} = \frac{\text{\# non-}\tau\text{ jets; pass }\tau\text{-ID}}{\text{\# non-}\tau\text{ jets; fail }\tau\text{-ID}}, \tag{9.1}$$

and is typically expressed as a function of parameters that affect the jet composition. Most typically the FFs are binned with respect to the $\tau_{\text{had-vis}}$ p_T and number of associated tracks.

This assumption on the jet composition dependence of the FF allows to perform the FF calculation in designated CRs, that share the same disposition, and then extrapolate the results to the analysis SR in order to estimate the number of fakes that fulfill the signal selection. The application of the FF to the SR can be expressed as:

$$\text{N}^{\text{SR}}_{\text{\# non-}\tau\text{ jets; pass }\tau\text{-ID}} = \text{N}^{\text{SR}}_{\text{\# non-}\tau\text{ jets; fail }\tau\text{-ID}} \times \text{FF}. \tag{9.2}$$

"Failure" to pass the $\tau_{\text{had-vis}}$ identification criteria in this procedure is typically an inverted identification (BDT or RNN) requirement on the $\tau_{\text{had-vis}}$ candidate, and will be referred to as "anti-τ SR" in later parts of the chapter.

Some form of loose τ identification or tau vertex requirement is typically still enforced in order to ensure that all considered jets share a similar composition.

The CRs for the calculation of the FFs are chosen such that they are enriched in a specific background process, while being close to the SR topology and uncontaminated (as much as possible) by any signal events. The presence of true $\tau_{\text{had-vis}}$ candidates in the CRs are accounted for and subtracted based on MC simulations. Aside from kinematics, the FF is also affected by the origin of the jet that is misidentified; namely if it is originating from a quark or a gluon. The contribution from the two cases will be different and they need to be addressed separately.

Depending on the analysis, the processes that create the non-τ jets making up the fake τ background are different and have distinct quark/gluon compositions. The FFs can in principle be calculated for each of these processes (as it is commonly done from many analyses currently) in CRs with compatible quark/gluon compositions to that of the SR. The results can then be extrapolated to the SR using the equations listed previously.

A different approach is to shift the focus on the non-τ jet origin fractions in the considered regions. Employing the dependency of the FF on this fraction could allow the development of a universal method for treating fake τs. The main principles for the development of such a universal FF method are discussed in the following section.

9.2 A universal Fake Factor method

The development of a universal method for FF estimation relies on the dependence of the FF on the quark-gluon fraction in a region of interest. Moving forward the quark-gluon fraction will be examined through the quark fraction.

Ideally one would like to be able to measure the pure FFs of quark- and gluon-initiated jets. Let p_q and p_g be the probabilities of a quark- and gluon-initiated jet to pass a given $\tau_{\text{had-vis}}$ identification criterion, then the pure corresponding fake-factor can be expressed as:

$$\begin{aligned} FF_{\text{q}} &= \frac{N_{\text{q, pass}}}{N_{\text{q, fail}}} = \frac{p_q}{1-p_q} \\ FF_{\text{g}} &= \frac{N_{\text{g, pass}}}{N_{\text{g, fail}}} = \frac{p_g}{1-p_g}, \end{aligned} \tag{9.3}$$

where $N_{\text{q/g, pass/fail}}$ is the number of quark/gluon-initiated jets that pass/fail the $\tau_{\text{had-vis}}$ identification criterion.

The fraction of quark-initiated jets that fail a given $\tau_{\text{had-vis}}$ identification criterion, can be represented as q_f in any given sample:

$$q_f = \frac{N_{\text{q, fail}}}{N_{\text{fail}}}, \tag{9.4}$$

while the respective fraction of gluon-initiated jets can be expressed as: $1-q_f$. This formulation allows the expression of the FFs as:

$$\begin{aligned} FF_q &= \frac{N_{\text{q, pass}}}{q_f \times N_{\text{fail}}} \\ FF_g &= \frac{N_{\text{g, pass}}}{(1-q_f) \times N_{\text{fail}}} \end{aligned} \tag{9.5}$$

Based on this expression one can derive the total number of QCD jets that successfully pass a given $\tau_{\text{had-vis}}$ identification criterion as:

$$N_{\text{pass}} = N_{\text{q, pass}} + N_{\text{g, pass}} = N_{\text{fail}} \times \left[q_f \times FF_{\text{q}} + (1-q_f) \times FF_{\text{g}}\right] \tag{9.6}$$

Given that it is not possible to identify data regions that contain such a pure jet origin content, one needs to rely on regions that are enriched in one over the other and express the fraction with respect to one of the two origins. Keeping the convention of using the quark fraction, q_f, the quark and gluon FFs in any region can be expressed through the pure FFs as follows:

$$FF_{\text{i}} = q_{f,i} \times FF_{\text{q}} + (1-q_{f,i}) \times FF_{\text{g}}, \tag{9.7}$$

where i represents a generic region with $q_{f,i}$ quark fraction. Eq. 9.7 illustrates the linear dependence of the FF on $q_{f,i}$.

In the case where two dedicated CRs are used for the measurement of the FFs, each with different quark-gluon fractions, the respective FFs are expressed as:

$$\begin{aligned} FF_{\text{CR,1}} &= q_{f,1} \times FF_{\text{q}} + (1-q_{f,1}) \times FF_{\text{g}} \\ FF_{\text{CR,2}} &= q_{f,2} \times FF_{\text{q}} + (1-q_{f,2}) \times FF_{\text{g}} \end{aligned} \tag{9.8}$$

and the pure FFs can be derived as follows:

$$\begin{aligned} FF_{\text{q}} &= \frac{(1+q_{f,2}) \times FF_{\text{CR,1}} - (1+q_{f,1}) \times FF_{\text{CR,2}}}{q_{f,2} - q_{f,1}} \\ FF_{\text{g}} &= \frac{q_{f,2} \times FF_{\text{CR,1}} - q_{f,1} \times FF_{\text{CR,2}}}{q_{f,2} - q_{f,1}}. \end{aligned} \tag{9.9}$$

Two CRs that serve as good regions for the calculations of the FFs are the gluon-dominated multi-jet region and quark-dominated $Z+$jets region. Calculating the FFs is one of the prerequisites in the approach. Additionally, one needs to estimate the quark fraction in each of the CRs. There are different ways that one can approach this and the current investigated method is by using MC templates.

The templates are based on a jet variable that is sensitive to its origin. An identified variable that offers good separation for the universal approach is the jet-width variable. The variable relies on kinematic attributes of the jet

constituents, identified using tracking information, and is defined as the p_T-weighted ΔR of objects associated to the jet:

$$j = \frac{\Sigma_i \Delta R^i p_T^i}{\Sigma_i p_T^i}, \tag{9.10}$$

where i ranges over the seed jet associated tracks [1].

The distributions of quark- or gluon-initiated jets with respect to this variable are the templates of reference. They can then be used to fit the distributions of the misidentified jets in each of the CRs to derive their respective quark fractions, denoted as $q_{f,1}$ and $q_{f,2}$ respectively. The same approach is used in the analysis fail-$\tau_{\text{had-vis}}$ identification region to derive the quark fraction, $q_{f,\,\text{SR}}$.

Once $FF_{\text{CR,1}}$, $FF_{\text{CR,2}}$, $q_{f,1}$, $q_{f,2}$ and $q_{f,\,\text{SR}}$ are obtained it is possible to derive the FF in the analysis SR using interpolation:

$$FF_{\text{SR}} = q_{f,\,\text{SR}} \times FF_{\text{q}} + (1 - q_{f,\,\text{SR}}) \times FF_{\text{g}}. \tag{9.11}$$

The interpolation needs to be performed separately for each of the parameters that the FF is binned in (ex. p_T and number of associated tracks.). The derivation of FF_{SR} allows the estimation of the number of jets that pass a certain $\tau_{\text{had-vis}}$ identification criterion in the signal region:

$$N_{\text{SR,\,pass}} = N_{\text{fail}} \times FF_{\text{SR}}. \tag{9.12}$$

The interpolation approach is also illustrated in Fig. 9.2.

The universal method described here is presently being embedded in a tool. The basic principles of applying the method through the tool are briefly described in the following section.

9.3 The Tau Fake Factor Tool

The tool that realizes the universal fake factor estimation method is still under development, therefore the present section aims to present simply the basic notions behind it.

The tool requires two kinds of inputs, from the tool users and from the developers. The inputs from the users' side are jet-width and p_T distributions in the dedicated analysis anti-τ SR. The distributions need to be provided in specified bins of p_T and number of tracks associated to the τ candidate. The binning has been chosen to match the one used for the fit.

The developers' inputs are information from the two data interpolation regions and the MC templates. The first one concerns the FFs for the multi-jet

[1] The track-association here is with respect to the event's primary vertex.

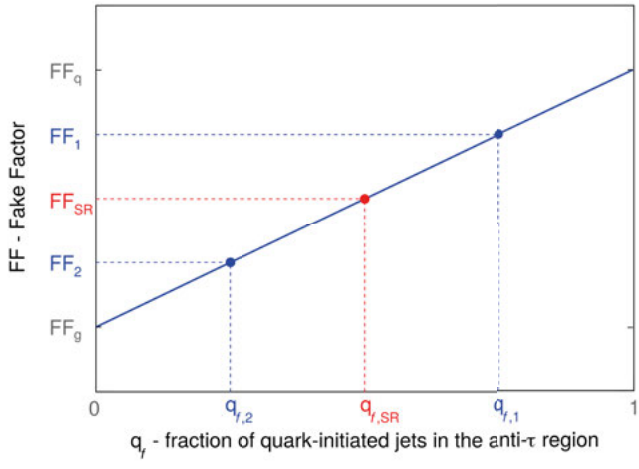

Figure 9.2. Fake factors vary linearly with respect to the quark fraction, q_f, of the non-τ jets that compose a certain region.

and $Z+$jets regions and their respective quark-gluon fractions, while the latter concerns simulated distributions (templates) of p_T and jet-width for the considered fake types.

The tool uses these inputs to first reweight the templates with respect to the provided user inputs. The reweighting is done with respect to the user-provided p_T distributions and is implemented to alleviate any bias from kinematics. Next, the jet-width distributions are fit with respect to the MC templates of the various fake types. The fit is based on the maximum likelihood method, and, when only considering statistical effects, the likelihood can be expressed as:

$$\mathscr{L} = \Pi_b \text{Pois}\left(N_b | \Sigma_i \alpha_i \nu_{i,b}\right) \tag{9.13}$$

where b ranges over the bins of the jet-width template, N_b are the data events in bin b, i ranges over the considered fake types, α_i is the respective fake type fraction and $\alpha_i \times \nu_{i,b}$ is the total number of fakes of origin i in bin b. The effect of statistical and systematic uncertainties will also be taken into account, with each systematic uncertainty inserting a constraint term into the likelihood. Examples of systematic uncertainties that will be included are uncertainties associated with the choice of MC generators for the templates, the p_T reweighting scheme[2] and the calculation of the FFs in the multi-jet and $Z+$jets regions. The considered fake types will be discussed in more detail in the next section.

The only free parameter in the fit is the quark fraction in the user defined anti-τ SR region and thus the derived optimal fit determines the quark fraction

[2]The templates themselves can vary within MC statistical uncertainties, affecting the template shape systematics and this should be reflected as an uncertainty.

in that region. Once the quark fraction is known the tool applies the equations mentioned in the previous section to interpolate the FF in the user defined anti-τ SR and derive the associated systematic uncertainties. The final output of the tool is in the form of a binned FF in terms of p_T and number of tracks associated to the τ candidate, along with its uncertainties.

9.4 Monte Carlo templates

The present section will give more details on the MC jet-width and p_T templates, with mentions of possible opportunities to further improve the capabilities of the tool.

The templates aim to serve as representative distributions of a specific fake type. Two distributions are of interest in this case; the p_T and the jet-width distributions of the fake τ jets. The latter is the variable capable of discriminating among the considered fake types, while the p_T distributions are needed for reweighting the jet-width templates to remove any kinematic bias.

The original concept of the tool was that it would rely on two templates for the determination of the quark fraction in the regions of interest. These were the quark and gluon templates. While the templates demonstrated similar distributions, as a function of track-based jet-width, across different samples, there were some discrepancies that necessitated a change of tactics. In MC studies, the origin of a fake τ candidate can be identified based on its truth matching information. A number of jets appeared to be unmatched to any known origin and therefore a new type was introduced, with the same name. The unmatched objects, are considered to be mostly originating from pileup jets, but because ATLAS MC does not store truth pileup jets it is not possible to match them to any stored object. Another observation was that b-quark jets have larger average jet-width distributions compared to other quarks, which caused a shift in the templates. To overcome this, the quarks were split to b-quark and non-b-quark jets (also referred to as "light-quarks[3], as they do not include t-quarks which decay before hadronization). The templates therefore consider four fake types; b-quark jets, non-b-quark jets, gluons and unmatched objects and the TFFT was adapted to use a four parameter fit to determine the non-b-quark fractions. The critical part of the FTTF mandate is the provision of reliable non-b-quark and gluon MC templates and FFs and the demonstration of a reliable tool operation with these objects. In that regard the work is progressing towards a useful outcome, yet there is a lot of work ahead (for example in the treatment of the systematic uncertainties) for the conclusion of the study.

Each of the fake τ candidate types is examined for different τ identification requirements. The most important identification threshold considered is

[3]The term "light-quark" includes u-/d-/s-/c-quarks.

the "Medium" τ identification requirement, as it is the most commonly used among ATLAS analyses. The distributions are derived in bins of p_T, with finer binning in lower p_T regions[4], and are considered separately for objects with one and three associated tracks.

The studies are performed in $Z+$jets, $W+$jets, $t\bar{t}$ and di-jet MC samples, to have good statistics for all fake types. The templates are not expected to differ across processes and any observed discrepancies will be treated as systematic uncertainties within the tool. The choice of MC sample generator has been observed to have an effect on the template distributions, especially on the gluon templates. The effects are under consideration and as a first solution they will be treated as an uncertainty.

An example of the jet-width templates from a $t\bar{t}$ sample is shown in Fig. 9.3 for the three finest p_T bins, for fake τ candidates with one (left) and three (right) associated tracks.

A further extension of the considered fake types is being investigated, by splitting the non-b quark jets further, into c- and light-quark[5] jets. In Fig. 9.4 one can see an example of such templates. The study is still ongoing, and no clear conclusions can be drawn at the moment. The split can at a primary stage provide information on how different quarks alter the jet-width fit shape and possibly further studies may provide the option of extracting information on the b- and c-quark initiated fakes fractions through the fit.

[4] $p_T \in \{20, 30, 40, 60, 90, 150, \infty\}$ GeV

[5] The term "light quark" in this case includes u-/d-/s-quarks.

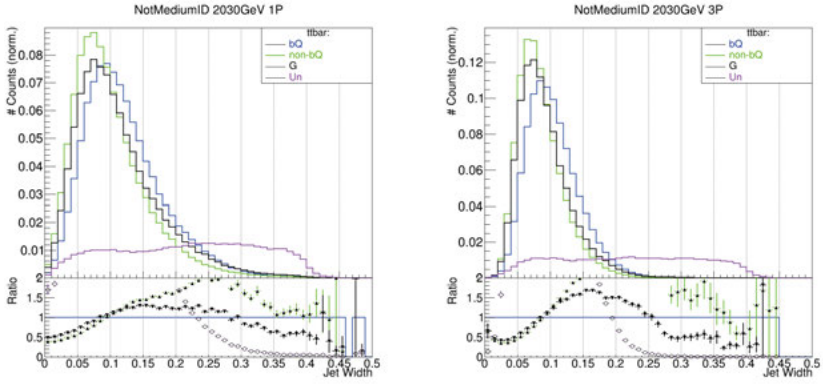

(a) (b)

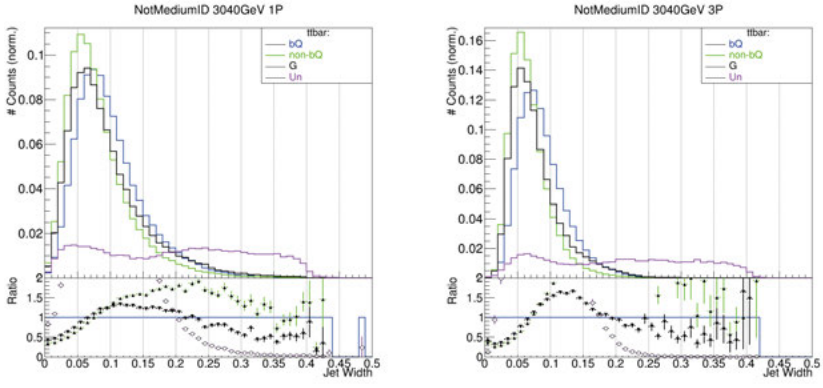

(c) (d)

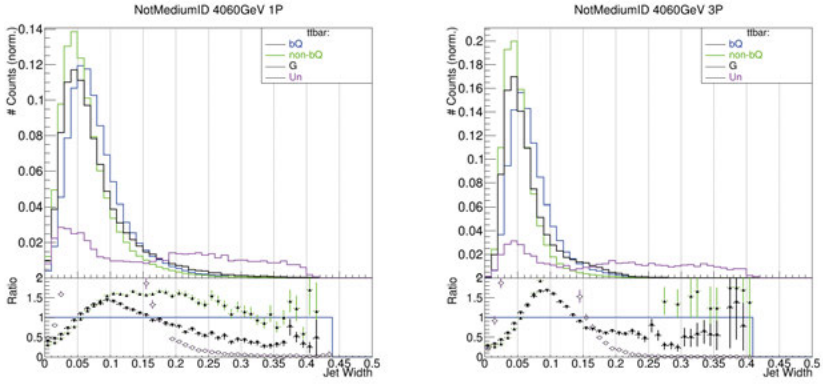

(e) (f)

Figure 9.3. Templates of the jet-width distributions for the four considered fake types (b-quark jets, non-b-quark jets, gluons and un-matched objects) failing the medium RNN τ identification requirement. The templates concern the three finest p_T bins (lowest) for candidates with one (left) and three (right) associated tracks and were derived from a $t\bar{t}$ sample.

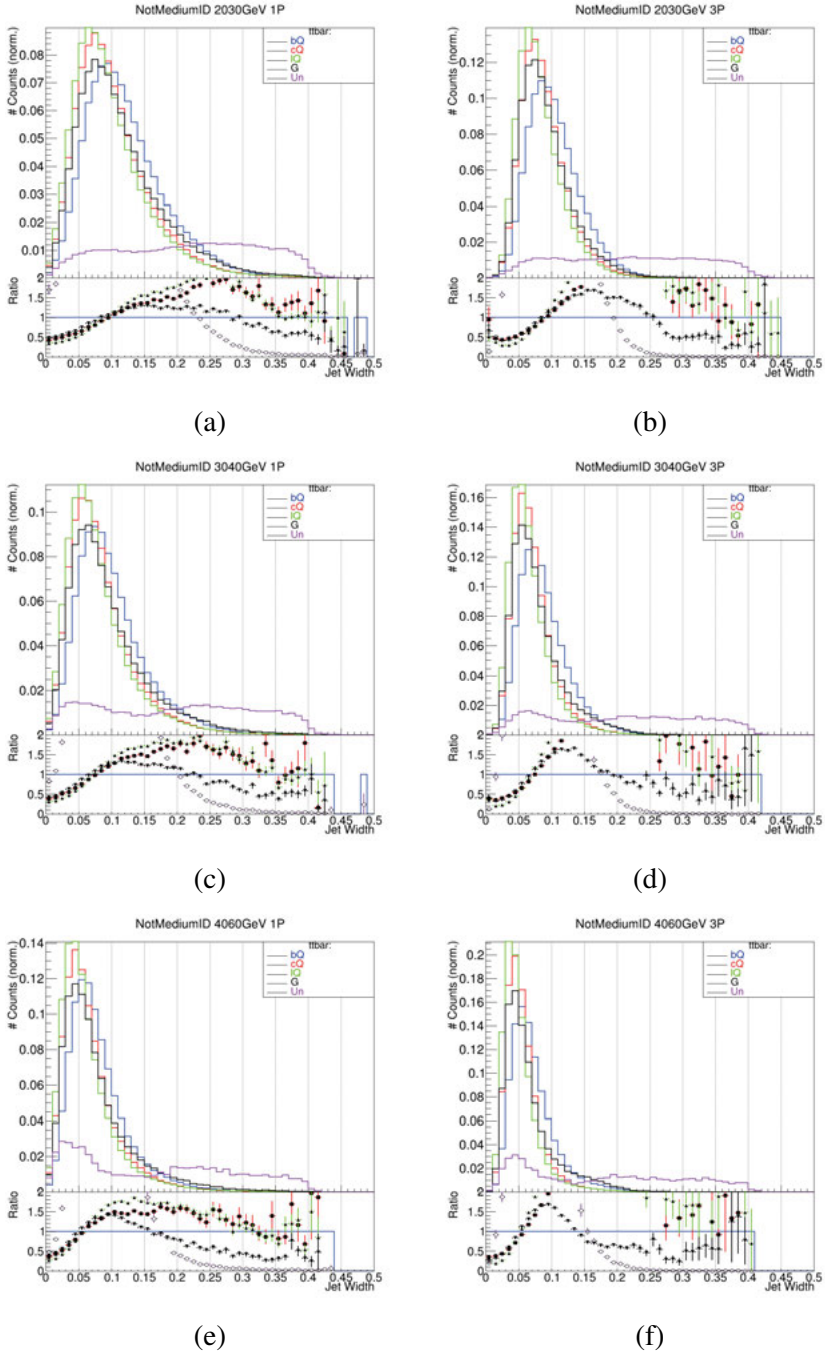

Figure 9.4. Templates of the jet-width distributions for the five considered fake types (b-quark jets, c-quark jets, light-quark jets, gluons and un-matched objects) failing the medium RNN τ identification requirement. The templates concern the three finest p_T bins (lowest) for candidates with one (left) and three (right) associated tracks and were derived from a $t\bar{t}$ sample.

10. Charged Higgs boson searches

Singly charged Higgs particles, $H^{\pm}$, are predicted in a number of BSM theories, such as the 2HDM, that were already discussed in Ch. 4, and several searches have been conducted by ATLAS [83–86] and CMS [87–91] all yielding exclusion limits. The studies probed a wide mass regime through the $\tau\nu$, cs, tb and $W^{\pm}/h/A$ predicted decay modes, yet no evidence of charged Higgs bosons have been found so far.

Here a search for charged Higgs bosons through the $H^{\pm} \to \tau\nu$ decay, with a subsequent hadronic decay of the τ lepton ($\tau_{\text{had-vis}}$), in the mass range $90 - 2000\,\text{GeV}$, is presented. The study was carried out using a partial ATLAS Run 2 dataset collected in 2015-2016, with $36.1 \pm 0.8\,\text{fb}^{-1}$ of data.

The theoretical motivations driving the searches are introduced in Sec. 10.1. The supporting elements of the study (MC samples and object reconstruction) are discussed in Sec. 10.2 and Sec. 10.3 and the analysis overview is given in Sec. 10.4. A dedicated discussion of the followed trigger strategy is provided in Sec. 10.5. Then, Sec. 10.6 describes the background modeling. A brief overview of the systematic uncertainties is given in Sec. 10.7, while the results and conclusions are discussed in Sec. 10.8.

10.1 Introduction

Within the scope of a CP-conserving type-II 2HDM, which is the Higgs sector of the Minimal Supersymmetric Standard Model (MSSM), the production and decay of charged Higgs bosons depend on its mass, $\text{m}_{\text{H}^{\pm}}$, and the ratio of the two predicted Higgs doublets' vacuum expectation values (Sec. 4.2), expressed through the parameter $\tan(\beta)$. In the MSSM, a number of benchmark scenarios have been defined. An example (as mentioned in Sec. 4.3) is the hMSSM model [21], which assumes the lighter of the two CP-even scalars to have a mass of 125 GeV and uses it to predict the remaining Higgs boson masses and couplings. The model also accounts for the (so far) non-observation of supersymmetric particles by setting the SUSY-breaking scale to masses above 1 TeV.

In MSSM scenarios, in the mass region below the top quark mass (specifically when $\text{m}_{\text{H}^{\pm}} + \text{m}_{\text{b}} < \text{m}_{\text{top}}$), denoted also as "low mass", the dominant production mechanism is through the decay of a top quark, $t \to bH^{\pm}$. In the LHC conditions, this type of decay is predominantly expected to occur

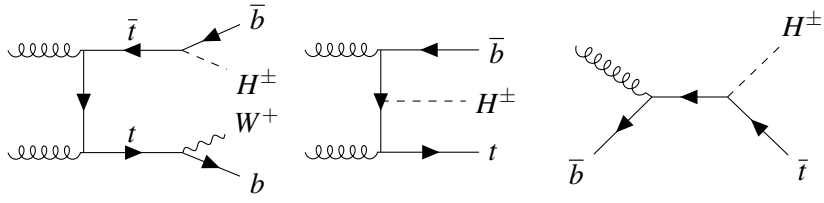

Figure 10.1. Leading-order Feynman diagrams for light (*left*) and 4FS (*middle*) and 5FS (*right*) heavy charged Higgs boson production.

in $t\bar{t}$ processes. $t\bar{t}$ is produced via QCD interactions and when it's kinematically allowed one of the top quarks could decay to a charged Higgs boson and a bottom quark (Fig. 10.1). In the mass regime above the top quark mass ($m_{H^{\pm}} + m_b > m_{top}$), "high mass", the leading production mechanisms are predicted to be in association with a top quark described through the $gg \to tbH^{\pm}$ or $gb \to tH^{\pm}$ processes, which are complementary (Fig. 10.1). The first is also known as the 4-flavor scheme (4FS), where the b-quark appears only in the final state, while the latter corresponds to the 5-flavor scheme (5FS), where the b-quark is included in the inital state. In principle both schemes correspond to the same production mode, but they assume a different b-quark origin[1]. In the mass regime close to the top quark mass the interactions between top-quark resonant and non-resonant diagrams and finite top-width effects need to be accounted for and the full $pp \to H^{\pm}W^{\mp}b\bar{b}$ process needs to be considered [92] (Fig. 10.2).

The $H^{\pm}$ is therefore expected to be produced in a topology that includes a top quark, in all possible mass ranges. The $H^{\pm}$ can then decay through different decay channels and their sensitivity differs with respect to the considered mass and $\tan(\beta)$ value (Fig. 10.3).

In the scope of hMSSM, $H^{\pm} \to \tau\nu$ is a sensitive channel over a large range of $H^{\pm}$ masses, especially for large $\tan(\beta)$ values where it is dominant at low masses and subleading at high masses. The presented study is focused on the $\tau\nu$ decay channel, where the produced τ proceeds to decay hadronically. The expected detector signatures for this decay are hadronic τ jets and missing transverse energy (E_T^{miss}) from the presence of neutrinos. The presence of the associated top quark can be utilized in the analysis to allow for a cleaner signature. A top quark decays though a b quark and a W boson and depending on the decay mechanism of the W, two distinct topologies are expected to

[1] In the 4FS, the bottom quark is treated as a massive object and is not attributed a parton distribution (PDF). This implies that QCD calculations do not include the b-quark, but rather only the four lightest quark flavors (justifying the "four-flavor" naming convention) and the gluons. Conversely, in the 5FS, the bottom quark is treated similarly to other quark flavors and is attributed a PDF, which in turn means that it is included in the QCD calculations ("five-flavor").

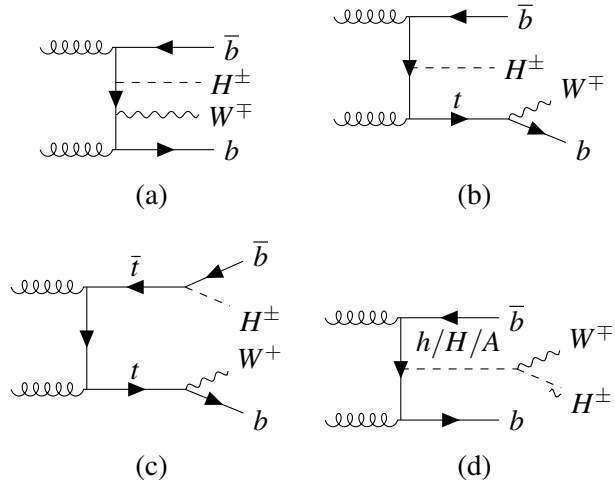

Figure 10.2. Leading-order Feynman diagrams for the full $pp \to H^{\pm}W^{\mp}b\bar{b}$ process. (The illustration includes only the parts of the process relevant for the discussion.) (a) non-resonant top-quark contribution; (b) single-resonant top-quark contribution; (c) double-resonant top-quark contribution; (d) contribution involving neutral scalars. The contribution of the neutral scalars is not included in this case, due to its small impact [92].

arise. A W boson can decay to either a charged lepton and a neutrino of the same generation, which would register in the detector as a lepton and MET, or to a quark and anti-quark pair, which would register as two jets (Fig. 10.4).

Two distinct analysis channels are considered based on the produced topologies; the "tau plus lep" channel (where the lepton is an electron or a muon), focusing on the topology resulting from the leptonic decay of the W boson, and the "tau plus jets" channel, resulting from the hadronic decay of the W boson. Only the latter will be discussed here.

The investigated mass regime covers the range $90 - 2000\,\text{GeV}$, which is split in three sub ranges; the low mass range $90 - 150\,\text{GeV}$, the high mass range $200 - 2000\,\text{GeV}$ and the intermediate region $160 - 180\,\text{GeV}$. The searches in the intermediate mass regime were investigated for the first time in the presented work, as it was the first time that precise and theoretically consistent predictions at next-to-leading order (NLO) were available for the full $pp \to \text{H}^{\pm}\text{W}^{\mp}b\bar{b}$ process [92]. The full extent of the study is published inclusively with the work conducted on the "tau plus lep" channel in [94].

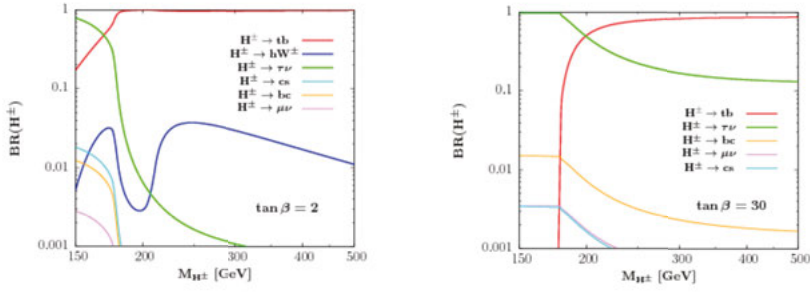

(a) (b)

Figure 10.3. The branching ratios of the charged Higgs boson as a function of its mass for $\tan(\beta) = 2$ (a) and $\tan(\beta) = 30$ (b) for the hMSSM with the assumed constraint of $m_h = 125\,\text{GeV}$. Figure from [93].

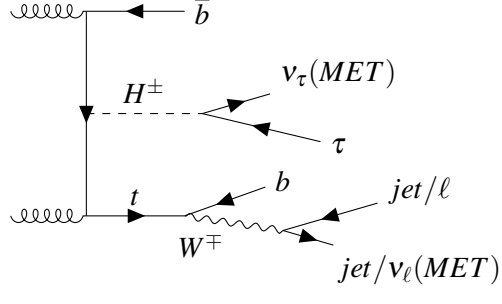

Figure 10.4. Example of the investigated analysis topology in the 4FS heavy charged Higgs boson production scheme. MET stands for the missing transverse energy (E_T^{miss}).

Sample	Generator + Parton Shower
Signal	MadGraph5 + Pythia v8
Background	
$t\bar{t}$	Powheg v2 + Pythia v6
Single-top-quark	Powheg v1 + Pythia v6
$W \to \tau\nu$	Sherpa
$Z \to \tau\tau$	Sherpa
Diboson (WW, WZ, ZZ)	Powheg v2 + Pythia v8

Table 10.1. *List of employed generators and parton showers for the signal and background modeling. Details on the generator versions, PDFs and tunes can be found in [94].*

10.2 Data and simulations

The study was carried out with data collected from pp collisions at $\sqrt{s} = 13\,\text{TeV}$ during the ATLAS data taking periods of 2015 (integrated luminosity of $3.2\,\text{fb}^{-1}$) and 2016 (integrated luminosity of $32.9\,\text{fb}^{-1}$), corresponding to a total integrated luminosity of $36.1 \pm 0.8\,\text{fb}^{-1}$. MC samples were generated for the modeling of both the background processes and the predicted signals (Tab. 10.1) and were subsequently normalized to match the integrated luminosity of the dataset. The signal simulations were done independently for the three targeted mass regions (low, intermediate, high) using MadGraph5_aMC@NLO [95] for the event generation and Pythia v8 [96] for the parton showers. In the low and intermediate mass regions, the dominant production mechanisms ($t\bar{t}$ and $pp \to \text{H}^{\pm}\text{W}^{\mp}b\bar{b}$ respectively) were simulated at leading-order (LO). At high masses the dominant production mechanism, $gg \to tbH^{\pm}$, was simulated at NLO. In the investigated scenarios the $\text{H}^{\pm}$ width is dominated by experimental effects (detector resolution), motivating the performance of the studies under the narrow width approximation. Under this approximation, the employed analysis method can been designed in a model-independent way, without any restrictions from specific theoretical models. It should be noted that the results in this study have been interpreted in the context of the hMSSM scenario, as it will be discussed in later sections.

The main background processes include $t\bar{t}$ (dominant in the low and intermediate masses), single-top quarks, $W+$ jets, $Z/\gamma^{\star}+$ jets, $WW/WZ/ZZ$ and multi-jet events. The event generation and parton shower modeling is done as mentioned in Tab. 10.1[2]. The processes are later categorized based on the object that gives rise to the identified $\tau_{\text{had-vis}}$; namely true hadronically decaying τs, misidentified light leptons (e or μ), or misidentified quark/gluon jets. The background modeling will be discussed in more detail in Sec. 10.6.

[2]More details on the generator versions, PDFs and tunes can be found in [94]

10.3 Object reconstruction

The analysis relies on several of the ATLAS reconstructed physics objects; electrons and muons, hadronic τs ($\tau_{\text{had-vis}}$), jets and E_T^{miss}, each of which is reconstructed based on the procedures outlined in Sec. 7.7. The "tau plus jets" decay channel, which is of interest here, uses $\tau_{\text{had-vis}}$, jets and MET.

Only reconstructed jets with $p_T > 25\,\text{GeV}$ and $|\eta| < 2.5$ are considered. Jets with $p_T > 60\,\text{GeV}$ and $|\eta| < 2.4$ are subdued to more stringent selections, using tracking and vertexing information, in order to select those associated with hard-scattering and reject jets from pile-up. In this analysis b-quark jets are identified using a 70% defined working point based on the MV2c10 algorithm (Sec. 7.7), offering rejection factors of 13, 56 and 380 against c-quark jets, $\tau_{\text{had-vis}}$ and light-quark or gluon jets respectively.

Taus are required to have a $p_T^{\tau_{\text{had-vis}}} > 30\,\text{GeV}$ and $|\eta| < 2.3$ (excluding the region between the barrel and end-cap calorimeters). Tau candidates suffer from possible misidentification from quark and gluon initiated jets (as discussed in the previous chapter) or light leptons. A medium BDT working point on the identification requirements is required for candidates with one and three associated tracks to suppress the first type of misidentification, while a likelihood-based veto is applied to address the latter. The applied working points offer a 75% and 60% signal efficiency and a $30-80$ and $200-1000$ rejection factor, against quark- and gluon-initiated jets in multi-jet events, for the one and three associated track cases respectively. The object identification can result in more than one object being associated with the same detector signatures. In these cases a well-established prioritisation of detector objects is done, in order to ensure that no double-counting is performed.

The last object that is reconstructed is the MET, following the procedures mentioned in Sec. 7.7.

10.4 Analysis overview

The expected signatures for the investigated

$$pp \to t\bar{t} \to [b\mathrm{H}^{\pm}][\bar{t}] \to [b\tau_{\text{had-vis}}\nu][jjb],$$

at low masses, and

$$pp \to [b]t\mathrm{H}^{\pm} \to [b][jjb][\tau_{\text{had-vis}}\nu],$$

at high masses, are four jets, E_T^{miss} and one hadronic tau.

Events that could potentially match these processes are collected using an E_T^{miss} trigger, with three different offline thresholds (70 GeV, 90 GeV and 110 GeV) depending on the considered data taking period. The efficiency and the general strategy surrounding the trigger are discussed in Sec. 10.5. Events

collected with the E_T^{miss} trigger are first evaluated with respect to their jet content; if jets are correlated to instrumental effects or non-collision background processes then the event is discarded, and the remaining events are required to consist of:

- a leading p_T reconstructed $\tau_{\text{had-vis}}$ with $p_T > 40\,\text{GeV}$, passing the medium BDT tau identification criteria requirements,
- at least three jets with $p_T > 25\,\text{GeV}$, where at least one of them is tagged as originating from a b-quark,
- no leptons (electrons or muons) with $p_T > 20\,\text{GeV}$ and
- $E_T^{\text{miss}} > 150\,\text{GeV}$.

Events passing these requirements make up the signal region (SR) of the analysis. The charged Higgs boson transverse mass is reconstructed from the $\tau_{\text{had-vis}}$ and the E_T^{miss} in the event:

$$m_T = \sqrt{2 p_T E_T^{\text{miss}} (1 - cos(\Delta\phi_{\tau,\text{miss}}))}, \tag{10.1}$$

where $\Delta\phi_{\tau,\text{miss}}$ is the azimuthal angle between the two objects.

Events that pass the SR requirements can be originating from either a charged Higgs boson signal or other (background) processes. Each of the background processes need to be properly accounted for in terms of their contribution to the SR. A method needs to be derived thereafter for their discrimination against the signal events.

The chosen discrimination method here is the use of an MVA where several variables are combined, each offering some distinction between signal and background events, to provide a stronger discriminating effect. Individual variables are used as an input to the chosen MVA method, which here are BDTs, to construct a single multivariate discriminant, commonly referred as BDT score. Tab. 10.2 lists the discriminating kinematic variables that were used in this study as inputs to the BDTs. The E_T^{miss}, p_T^{τ} and $\Delta\phi_{\tau,\text{miss}}$ variables are the ones included in the definition of m_T in Eq. 10.1. m_T was the main discriminating variable used in the previous iteration of the analysis [83] and is the most powerful discriminating variable at high masses. The list of variables has been extended, with respect to the previous iteration of the study, to include more variables that improve the discrimination against the background processes especially in the low and intermediate mass regimes. The variables do not exhibit any noteworthy correlations. An important addition to the discriminants is the Υ variable, which is only defined for the case where the τ candidate has only one associated track, as:

$$\Upsilon = \frac{E_T^{\pi^\pm} - E_T^{\pi^0}}{E_T^{\tau}} \simeq 2\frac{p_T^{\tau\text{-track}}}{p_T^{\tau}} - 1, \tag{10.2}$$

where $p_T^{\tau\text{-track}}$ is the transverse momentum of the track associated with the $\tau_{\text{had-vis}}$ candidate. The variable reflects the polarization of the $\tau_{\text{had-vis}}$ can-

didate, offering differentiation between $t \to bH^{\pm}$ and the $t \to bW$ SM background. The two processes have very similar kinematic topologies for low masses, but the polarity of the $\tau_{\text{had-vis}}$ is different as it is generated from a vector boson in the SM case, rather than a scalar in the signal case.

The investigated mass range is split in five distinct subranges for the BDT training, allowing a uniform event topology and kinematic distributions among the BDT input variables. The bins are chosen as: $90-120\,\text{GeV}$, $130-160\,\text{GeV}$, $160-180\,\text{GeV}$, $200-400\,\text{GeV}$ and $500-2000\,\text{GeV}$. The training is done independently for the cases where the $\tau_{\text{had-vis}}$ candidate has one (1P) or three (3P) associated tracks in each mass region, except for the heaviest range. This is related to the variables that are expected to be most sensitive for the separation of signal from background in each range. As mentioned, at the high masses the three variables included in the definition of m_T are the most discriminant, but at lower masses the ranking of the Υ variable becomes increasingly important. Conversely, for the highest mass range, Υ does not contribute significantly compared to the other variables, and is thus omitted from the training.

BDT input variable	$\tau_{\text{had-vis}}$+jets	$\tau_{\text{had-vis}}$ + lepton
E_T^{miss}	y	y
p_T^{τ}	y	y
$p_T^{\text{b-jet}}$	y	y
p_T^{ℓ}	n	y
$\Delta\phi_{\tau,\text{miss}}$	y	y
$\Delta\phi_{\text{b-jet,miss}}$	y	y
$\Delta\phi_{\ell,\text{miss}}$	n	y
$\Delta R_{\tau,\ell}$	n	y
$\Delta R_{\text{b-jet},\ell}$	n	y
$\Delta R_{\text{b-jet},\tau}$	y	n
Υ	y	y

Table 10.2. *Table listing the BDT input variables for the five mass bins. The tables is also available in [94].*

10.5 Trigger strategy

The triggering of potentially interesting events for the analysis is carried out with the E_T^{miss} trigger. An alternative choice of trigger could have been a combined $\tau + E_T^{\text{miss}}$ trigger, similarly to an older iteration of this study [83], but during Run 2 the two triggers shared the same E_T^{miss} thresholds. The standalone E_T^{miss} trigger requires a simpler efficiency estimation procedure and avoids performing any cuts on the $\tau_{\text{had-vis}}$ properties, singling out this trigger as the better choice.

The analysis sensitivity is closely related to the trigger efficiency, as it defines the amount of data that can be collected from the searched signal and the expected background processes. The discussed trigger is poorly modeled in MC, mandating the measurement of its efficiency in data. The efficiency measurements need to be carried out in a data CR that has a similar kinematic topology to that of the SR, so that it is possible to extrapolate the results with as low systematic errors as possible. The event selection for the chosen CR is orthogonal to that of the SR as it relies on using a single electron trigger with a $p_T > 24\,\text{GeV}$ threshold and a loose likelihood identification requirement. Additionally the CR definition imposes:

- at least one reconstructed $\tau_{\text{had-vis}}$ with $p_T > 30\,\text{GeV}$, passing loose BDT tau identification criteria requirements,
- one electron with $p_T > 26\,\text{GeV}$, passing loose identification criteria requirements,
- no muons with $p_T > 20\,\text{GeV}$ and
- at least two jets with $p_T > 25\,\text{GeV}$, where at least one of them is tagged as originating from a b-quark,

The loose identification criteria requirement for the e and $\tau_{\text{had-vis}}$ objects is motivated by the need to optimize the statistical precision of the E_T^{miss} efficiency fit.

The calculation of the E_T^{miss} trigger efficiency in the CR is done as a function of the offline value of the event E_T^{miss}. The efficiency ε of the trigger is defined as the number of events that pass the CR requirements and additionally pass the L1 and HLT requirements of the E_T^{miss} trigger that is used in the SR, over the number of events that only pass the CR requirements.

$$\varepsilon = \frac{\text{Pass CR selection \&\& Pass L1 Trigger \&\& Pass HLT Trigger}}{\text{Pass CR selection}} \tag{10.3}$$

The binning will inevitably introduce a bias in the estimated efficiency. The derived efficiency is transformed into a continuous efficiency, to remove this bias, through a parametric fit. The fit uses the error function, with four floating parameters:

$$F(x) = p_0 \times (1 + erf(\frac{x - p_1}{p_2})) + p_3 \tag{10.4}$$

The outlined procedure is followed for each of the triggers that were used in this analysis and the respective calculated efficiencies are applied to the events of the relevant MC samples as weights, depending on their offline E_T^{miss} values. The weight reflects the efficiency of the trigger to identify this event in the considered kinematics topology.

The stability of the approach is evaluated by varying the allowed error in the fitted points (increase by a factor of 4). The difference from the nominal error is used as a systematic uncertainty of the fit. The variation of the efficiency curves with respect to different identification requirements for the $\tau_{\text{had-vis}}$ and the e, as well as the number of required jets in the CR selection criteria, are also

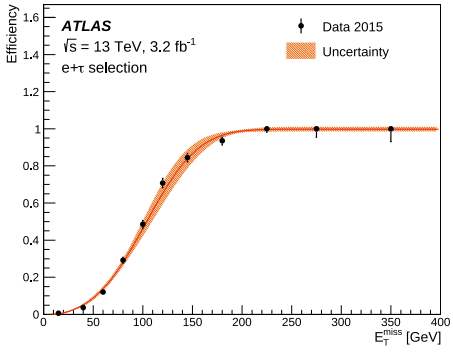

(a) Threshold at 70 GeV.

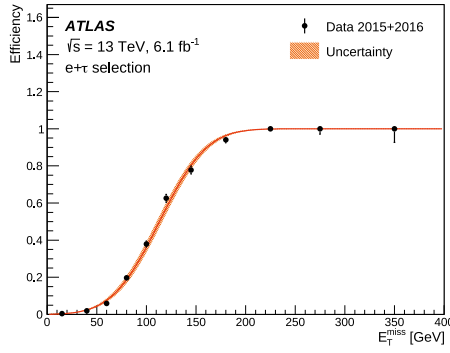

(b) Threshold at 90 GeV.

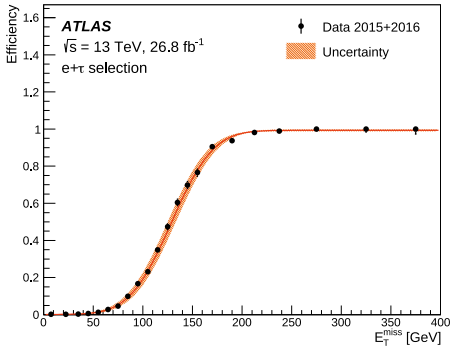

(c) Threshold at 110 GeV.

Figure 10.5. Efficiency curves of the E_T^{miss} triggers used in the analysis. The threshold values correspond to the relevant software threshold that is applied to each of them. The uncertainty bands include the total systematic uncertainties that are discussed in the text.

evaluated and taken into account as a systematic uncertainty. The calculated efficiencies are shown in Fig. 10.5 and the effects of the variations in Fig. 10.6.

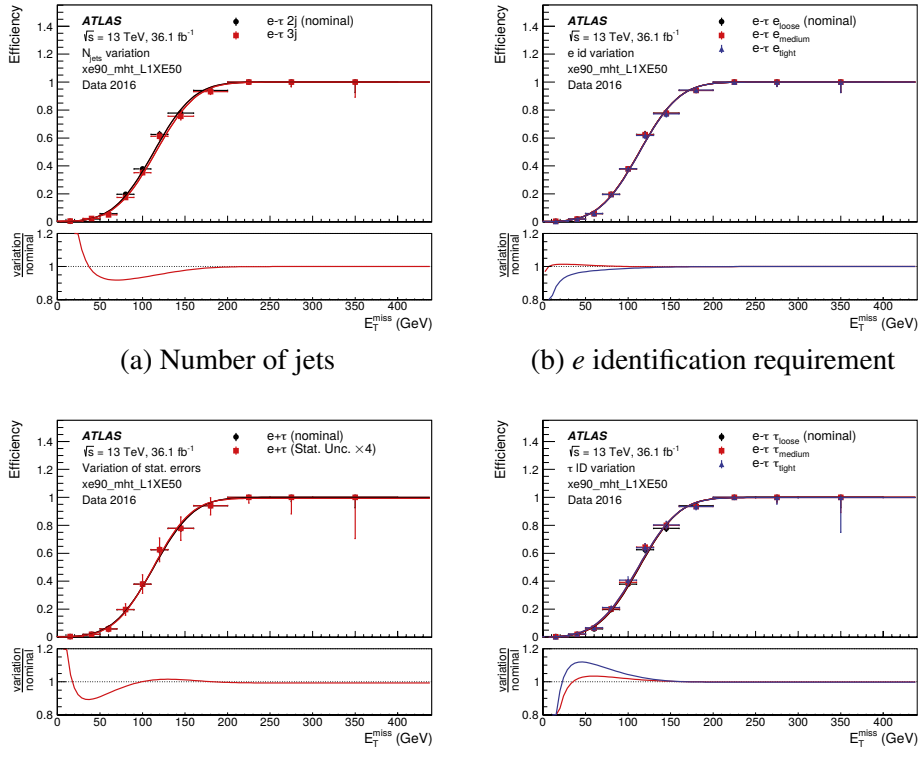

(a) Number of jets

(b) e identification requirement

(c) Statistical uncertainty

(d) τ identification requirement

Figure 10.6. Effects of variations to the trigger efficiencies for the E_T^{miss} trigger with software threshold at 90 GeV. The differences are used as systematic uncertainties of the calculated efficiency curve.

10.6 Background modeling

The analysis needs to account for the dominant background processes that are expected to enter the SR. These are primarily $t\bar{t}$ (dominant in the low and intermediate masses), single-top-quark, $W+$ jets, $Z/\gamma^{\star}+$ jets, $WW/WZ/ZZ$ and multi-jet events. The background processes are treated collectively depending on the object resulting in the $\tau_{\text{had-vis}}$ signature.

The contributions from background processes that produce true τs are modelled and evaluated in MC. Events where an electron or a muon are misidentified as a $\tau_{\text{had-vis}}$ can come from $t\bar{t}$, single-top quark, $W/Z+$jets and di-boson processes. This type of background makes up for 3% of the total background and is modelled in MC. Studies in $Z \to e^{+}e^{-}$ events in data allow the measurement of the electron-induced $\tau_{\text{had-vis}}$ misidentification and the computation of a correction factor that is then applied to the MC samples to account for differences.

Backgrounds from quark and gluon initiated jets that are misidentified as $\tau_{\text{had-vis}}$ are modelled with the data driven FF method, which was discussed in the previous chapter. The processes contributing to this background have different quark-gluon fraction compositions, each of which need to be accounted for separately. This is addressed with an approach that resembles the one discussed in Ch. 9, for the unified method approach.

The SR FF is interpolated from the calculated FFs in two dedicated CRs with different quark-gluon fractions[3]. The FF calculation in each of the CRs is binned with respect to the p_T and number of associated tracks of the candidate. The two regions are the gluon-initiated-jet dominated "multi-jet" CR and the quark-initiated-jet dominated "W plus jets" CR. The "multi-jet" CR is based on the "tau plus jets" selection criteria but with an $E_T^{\text{miss}} < 80\,\text{GeV}$ requirement and a b-quark-jet veto in the event selection. To remove any biases from the E_T^{miss} trigger efficiency turn-on curve, the triggering is performed using a combination of multi-jet triggers instead of the E_T^{miss} trigger. The "W plus jets" CR is based on the same selection criteria as the "tau plus lep" SR, where the nominal selection requires:

- exactly one lepton (e or mu) with $p_T > 30\,\text{GeV}$, matched to a trigger [4],
- exactly one τ candidate $p_T > 30\,\text{GeV}$, passing the medium BDT tau identification criteria, with a charge opposite to that of the lepton,
- at least one jet tagged as originating from a b-quark with $p_T > 25\,\text{GeV}$ and
- $E_T^{\text{miss}} > 50\,\text{GeV}$.

[3]The FF method employed here relies on the FF calculation in the two CRS and does not perform a calculation of the quark fraction in the SR, as in universal FF method described in Ch. 9.

[4]The "tau plus lep" channel event selection is based on single-lepton triggers. The trigger strategy relies on combining low ($26/24\,\text{GeV}$, for both e,μ) trigger thresholds with tight isolation requirements and high ($60-140\,\text{GeV}$ for e and $50\,\text{GeV}$ for μ) trigger thresholds with loose isolation requirements through a logical OR to maximize efficiency.

The "W plus jets" definition follows the same selection but does not include any cut on the E_T^{miss} during event selection, while it applies a b-quark-jet veto and the requirement $60\,\text{GeV} < m_T(\ell, E_T^{miss}) < 160\,\text{GeV}$, where $m_T(\ell, E_T^{miss}) = \sqrt{2 p_T E_T^{\text{miss}} (1 - cos(\Delta\phi_{\ell,\text{miss}}))}$. The "fail" $\tau_{\text{had-vis}}$ identification criterion in the FF calculation is an inverted BDT requirement on the SR $\tau_{\text{had-vis}}$ candidate ("not-Medium"), where a loose identification requirement is still enforced on the candidates to ensure a similar composition of jets entering the CR. True $\tau_{\text{had-vis}}$ candidates that enter the CRs (5% for the "multi-jet" CR and 10% for the "W plus jets" CR) are accounted for and subtracted with MC simulations.

Similarly to the approach described in Sec. 9.2, the interpolation relies on the knowledge of the quark-gluon composition in each of the CRs, as well as the SR. A discriminating parameter that is sensitive to the quark-/gluon-initiated jet fraction in each region can be used to derive templates in the two CRs and to estimate the respective fraction in any other region from a fit of the relevant distribution in that region. In this analysis the identified discriminating parameter for candidates with one associated tracks (1-prong or 1P) is the $\tau_{\text{had-vis}}$ width:

$$w_\tau = \frac{\Sigma \left[p_T^{\text{track}} \times \Delta R_{(\tau_{\text{had-vis,track}})} \right]}{\Sigma \left[p_T^{\text{track}} \right]} \tag{10.5}$$

for $\Delta R_{(\tau_{\text{had-vis,track}})} < 0.4$, and the $\tau_{\text{had-vis}}$ BDT output score for candidates with three associated track (3-prong or 3P).

The distribution of the relevant discriminant parameter in the SR, f(x), is used to perform a fit to the two templates of known quark/gluon-initiated jet fractions as follows:

$$f(x|\alpha_{\text{MJ}}) = \alpha_{\text{MJ}} \times f_{\text{Multi-Jet CR}}(x) + (1 - \alpha_{\text{MJ}}) \times f_{\text{W+Jets CR}}(x) \tag{10.6}$$

where α_{MJ} is the free parameter of the fit and represents the quark/gluon-initiated jet fraction in the SR as a percentage to the similarity of the fraction present in the "multi-jet" CR. The optimal fit, and therefore the most suited α_{MJ} value, is derived through the χ^2 fit, separately for each FF bin.

The combined FF that represents both quark- and gluon-initiated jet fakes in the SR is expressed as:

$$\text{FF} = \alpha_{\text{MJ}} \times \text{FF}^{\text{Multi-Jet CR}} + (1 - \alpha_{\text{MJ}}) \times \text{FF}^{\text{W+Jets CR}} \tag{10.7}$$

and is binned with respect to p_T and the number of associated tracks (Fig. 10.7). The FF is then applied to the SR as:

$$\text{N}^{\text{SR}}_{\text{\# non-}\tau\text{ jets; pass }\tau\text{-ID}} = \text{N}^{\text{SR}}_{\text{\# non-}\tau\text{ jets; fail }\tau\text{-ID}} \times \text{FF}, \tag{10.8}$$

to obtain the number of fakes passing the SR selection.

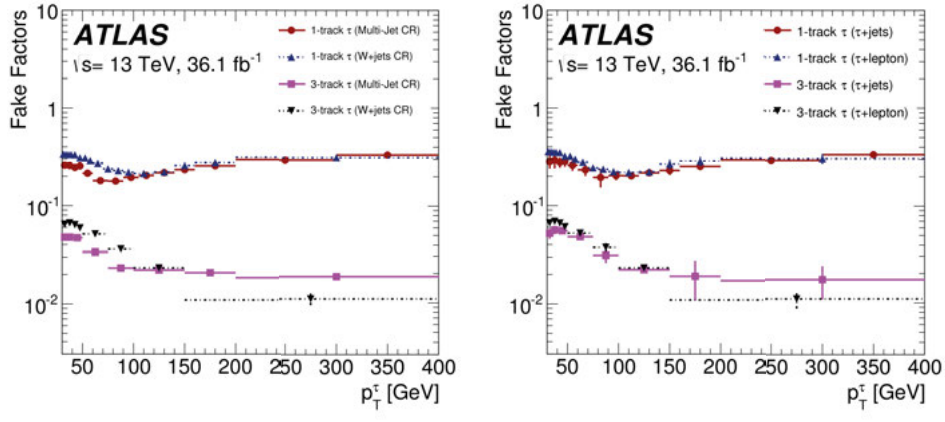

(a) (b)

Figure 10.7. Fake factor distributions as a function of p_T and the number of associated tracks of the $\tau_{\text{had-vis}}$ candidate, in (a) the multi-jet and $W+$jets CRs and (b) in the "tau plus jets" and "tau plus lep" SRs, after the reweighting with α_{MJ}. The figures are also available in [94].

It should be noted that this data-driven method introduced a mismatch in the modeling of the Υ and a Smirnov transformation [97] was employed to address this and remodel the shape of the distribution.

The background modelling is validated in signal-depleted CRs. The CRs aim to validate mostly the $t\bar{t}$ and the fake τ background.

The first background validation region is the $t\bar{t}$-enriched CR, and as it is more dominant in the "tau plus lep" decay channel, it is based on the same selection requirements that were mentioned earlier in the text. The $t\bar{t}$-enriched CR shares the same selection requirements, with the requirement of consisting of an oppositely-charged with different flavor lepton instead of the $\tau_{\text{had-vis}}$ (i.e. an $e\mu$ pair in place of the $e\tau_{\text{had-vis}}$ or $\mu\tau_{\text{had-vis}}$). The dedicated background CR is important also for the full analysis as it is included as a single-bin distribution in the statistical analysis described in Sec. 10.8 to constrain the $t\bar{t}$ normalization.

The second background CR is again defined with the same criteria as the "tau plus lep" SR except that additional b-quark tagged jets are vetoed and it aims to validate the quark/gluon-initiated-jet misidentification background modeling.

The validations are carried out by comparing the distribution of the BDT score in each of the regions against the expected one. The BDT distributions (Fig. 10.8 and Fig. 10.9) appear to be in good agreement with the expectations.

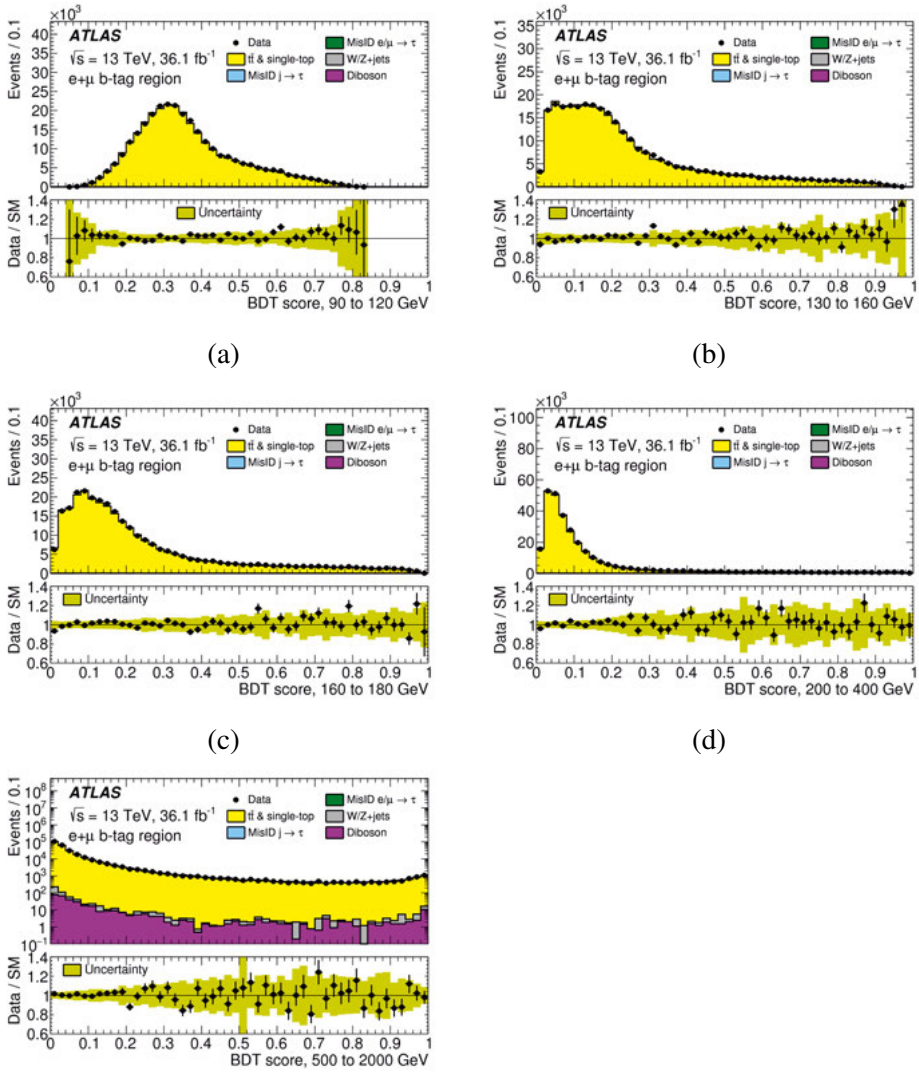

(a) (b)

(c) (d)

(d)

Figure 10.8. Distributions of the BDT score for the predicted backgrounds and data in the $t\bar{t}$-enriched CR. The distributions are shown for each of the five $H^{\pm}$ training mass regions. The lower panel of each plot shows the ratio of data to the SM background prediction. The uncertainty bands include all statistical and systematic uncertainties. The figures are also available in [94].

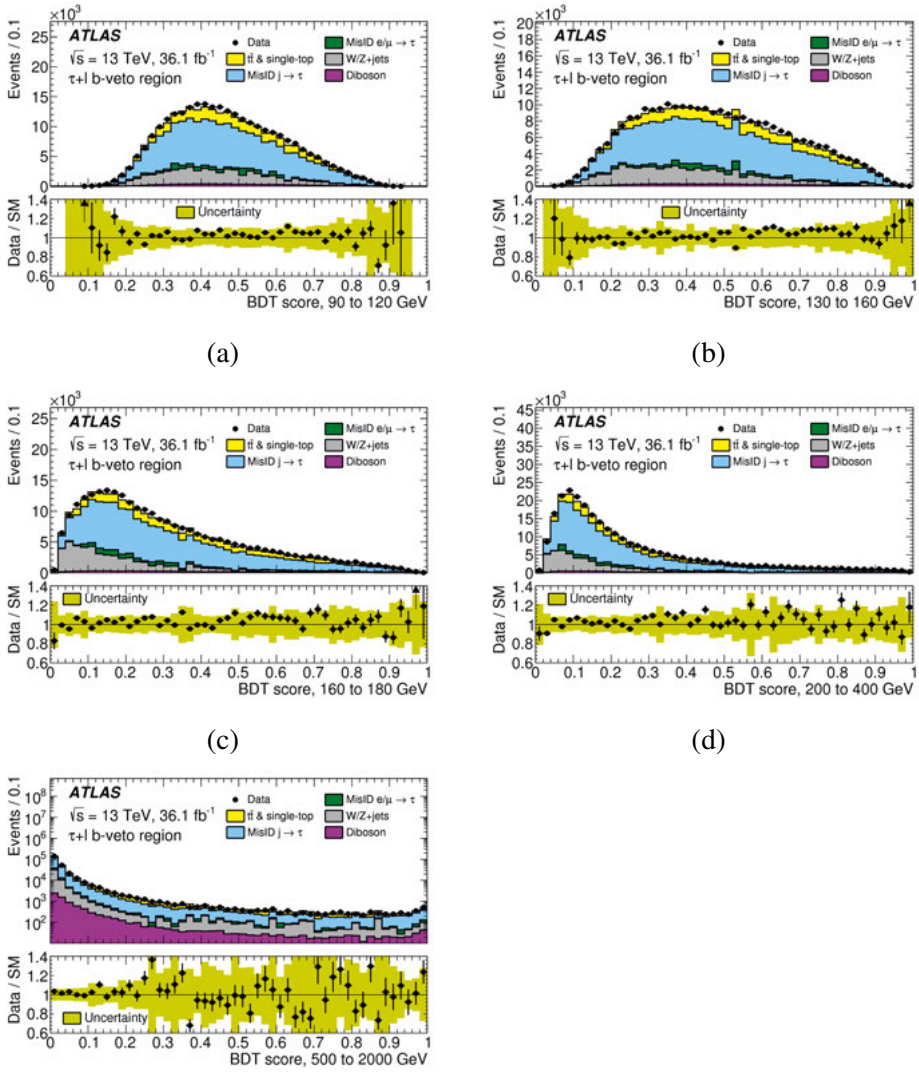

(a) (b) (c) (d) (d)

Figure 10.9. Distributions of the BDT score for the predicted backgrounds and data in the misidentified-jet-as-τ background CR. The distributions are shown for each of the five $H^{\pm}$ training mass regions. The lower panel of each plot shows the ratio of data to the SM background prediction. The uncertainty bands include all statistical and systematic uncertainties. The figures are also available in [94].

10.7 Systematic uncertainties

Systematic uncertainties from sources such as the detector, the background modeling and the signal generation inevitably affect the study. They are expected to affect the normalisation of the signal and background processes, and the shape of the BDT score distribution that is used as the final discriminant, making it essential to be aware of their impact with respect to the sensitivity of the analysis. Each of the sources are assumed to be uncorrelated, but when applicable, the correlations of a given systematic uncertainty are maintained across all processes. Additionally all systematic uncertainties are assumed to be symmetrical with respect to the nominal value.

Sources of instrumental systematic uncertainty are the reconstruction and identification efficiencies and the energy scales and resolutions of the particles involved in the study, as well as their impact on the reconstruction of the E_T^{miss} in the events. The most important are the impacts from the JES (ranging between 1% and 4.5% depending on the jet p_T), the b-tagging (ranging between 2% and 10% depending on the jet p_T) and the $\tau_{\text{had-vis}}$ reconstruction and identification efficiencies (3% and 6% for the "tau plus lep" and "tau plus jets" channels respectively), and their energy scale ($2-3\%$) Additionally, the impact of the E_T^{miss} trigger uncertainties is also included, as described in the Sec. 10.5.

Several sources of systematic uncertainties are also introduced from the background modeling. In the modeling of the jets misidentification background, one source of uncertainty is the requirement of a Loose identification for the "fail" $\tau_{\text{had-vis}}$ objects in the background modeling CRs. The requirement modifies the corresponding fractions of quark- and gluon- initiated jets and the event topology and its impact is evaluated by considering the shape of the final discriminant for different identification thresholds (symmetric around the nominal threshold). The FF calculation also contributes to the systematic uncertainties because of statistical uncertainties in the events entering the FF calculation regions, in each bin of their parameterisation and for each control region. The true $\tau_{\text{had-vis}}$ background modeling, the shape of the $t\bar{t}$ background (that is also included in the BDT), the choice of parton shower and hadronisation models, as well as matrix-element generators and the heavy-flavour jet modelling, are all further contributing sources to the systematic uncertainties.

In the signal ($H^{\pm}$) modeling the main sources of systematic uncertainties are from missing higher-order corrections. This is also referred to as the QCD scale uncertainty and is assessed by varying the factorisation and renormalisation scales up and down by a factor of two. The largest variation of the signal acceptance is symmetrized and kept as the scale uncertainty. The impact is of the order of $4-8\%$ depending on the considered signal mass. Other sources of systematic uncertainties that are taken into account originate from the choice of parton shower and underlying-event tune or different parton distribution function sets.

The contribution of the systematic uncertainties to the analysis sensitivity is different depending on the mass of the charged Higgs boson. The dominant sources of systematic uncertainties in the low and intermediate mass regime are related to the reconstruction, the identification and the misidentification background modelling of the $\tau_{\text{had-vis}}$ candidate, while in the high mass regime the prevailing systematic uncertainties come from the low event yield, the signal modelling and the misidentification background modelling of the $\tau_{\text{had-vis}}$ candidate.

Sample	Event yields				
True $\tau_{\text{had-vis}}$					
$t\bar{t}$	6900	$\pm$	60	$\pm$	1800
Single-top-quark	750	$\pm$	20	$\pm$	100
$W \to \tau\nu$	1050	$\pm$	30	$\pm$	180
$Z \to \tau\tau$	84	$\pm$	42	$\pm$	28
Diboson (WW, WZ, ZZ)	63.2	$\pm$	4.6	$\pm$	7.2
Misidentified $e, \mu \to \tau_{\text{had-vis}}$	265	$\pm$	12	$\pm$	35
Misidentified $jet \to \tau_{\text{had-vis}}$	2370	$\pm$	20	$\pm$	260
All backgrounds	11500	$\pm$	80	$\pm$	1800
$H^{\pm}$ (170 GeV), hMSSM, $tan(\beta) = 40$	1400	$\pm$	10	$\pm$	170
$H^{\pm}$ (1 $mathrmTeV$), hMSSM, $tan(\beta) = 40$	10.33	$\pm$	0.06	$\pm$	0.78
Data	11021				

Table 10.3. *Expected yields in the analysis SR from background processes, as well as the predictions for signal yields from a charged Higgs boson with a mass of* $m_{H^{\pm}} = 170\,\text{GeV}$ *and* $m_{H^{\pm}} = 1\,\text{TeV}$ *with cross-section times branching fraction corresponding to* $tan(\beta) = 40$ *in the hMSSM benchmark scenario. The third and fourth columns list the statistical and systematic uncertainties of the nominal values. The table is also available in [94].*

10.8 Results and conclusions

The previous sections covered the definition of the analysis SR, the modeling of the expected backgrounds, the choice of a suitable MVA discriminant and the type of systematic uncertainties that limit the search. These set the basis for carrying out a statistical analysis on the data to test their compatibility with the SM-only and signal-plus-background hypotheses.

A rough conclusion on the analysis results can be made from the obtained yields in the SR and their comparison to the expected yields from background processes and signal events. These are summarized in Tab. 10.3.

The numbers are consistent with the SM-only hypotheses. This approach however is not expected to be very sensitive for the charged Higgs boson searches, motivating the use of more tailored techniques, relying on the BDT score shape, and the use of a log-likelihood minimisation fit to the signal-plus-background hypothesis for evaluating the results in this study.

As outlined in Ch. 8 the data can be subjected to a fit using the likelihood method to identify parameters of interest that are unknown in the study. In this case the parameters of interest are the charged Higgs production cross section times the $\tau\nu$ branching ratio ($BR(H^{\pm} \to \tau\nu)$), commonly referred to as signal strength, which is encapsulated in the parameter $\mu = \sigma(pp \to tbH^{\pm}) \times BR(H^{\pm} \to \tau\nu)$, and the nuisance parameters associated to statistical and systematic uncertainties. The likelihood is expressed as a function of the signal strength and the nuisance parameters, and is constructed as the product of Poisson probability terms over all the bins and regions con-

sidered in the analysis. The number of events in these bins and regions are directly correlated to the signal strength and nuisance parameters and the best fit points to the most probable values for these parameters. The results of the fit are quantified into a test statistic quantity q, as defined in Eq. 8.2, which allows the assessment of how well one can reject the signal-plus-background hypothesis.

The results are interpreted inclusively for both the "tau plus lep" and "tau plus jets" channels and the log-likelihood minimisation fit is performed simultaneously on the relevant SR regions and the $t\bar{t}$ enriched control region.

The fit in the SRs is based on the BDT score distributions for each of the five mass regions. The binning needs to be optimised with respect to the statistical uncertainties in each bin as well as the granularity of the distribution. The most efficient binning was identified to be a reversed logarithmic bin spacing, with coarser bins at low BDT score and finer binning at high BDT scores where the signal is expected. The CR is included in the fit as one single bin, as its purpose is to constrain the $t\bar{t}$ yield, and the shape of the BDT is not relevant.

The BDT score distributions after the fit for the "tau plus jets" channel is shown in Fig. 10.10. The distributions from the "tau plus lep" analysis channels are shown in Fig. 10.11 and Fig. 10.12.

The results are expressed in terms of limits from the hypothesis testing, using the modified frequentist or CLs approach on the signal strength for the full investigated mass range, at a 95% confidence level. The same procedure is employed for the branching ratio of the $t \to bH^{\pm}$ production process times the $\tau\nu$ decay branching ratio, $BR(t \to bH^{\pm}) \times BR(H^{\pm} \to \tau\nu)$, for the low mass regime. The results are shown in Fig. 10.13.

The limits range between 4.2 pb and 2.5 fb depending on the charged Higgs boson mass. The limits are interpolated between the considered mass regions and the bias introduced from such as interpolation is smaller than the statistical uncertainty.

The systematic uncertainties affecting the analysis are listed in Tab. 10.4. The derivation of each of the systematics is discussed in more detail in [94].

Finally exclusion limits are also set on the values of $tan(\beta)$ in the context of the hMSSM over the full range of the investigated charged Higgs boson masses. Only the values of $tan(\beta) < 60$ are considered in the limit setting, given the availability of reliable theoretical calculations. The results are shown in Fig. 10.14. All the areas above the observed limits are excluded.

In summary, the conducted study using a 36.1 fb^{-1} dataset of pp collisions at $\sqrt{s} = 13$ TeV yielded results compatible with the SM-only hypothesis, yet it successfully set new upper limits on the charged Higgs boson signal strength over the mass range of $90 - 2000$ GeV, which corresponds to observed limits of $0.25 - 0.031\%$ for $BR(t \to bH^{\pm}) \times BR(H^{\pm} \to \tau\nu)$[5]. The exclusion limits

[5]This limit setting is under the assumption that the production cross-section is equal to the $t\bar{t}$ production.

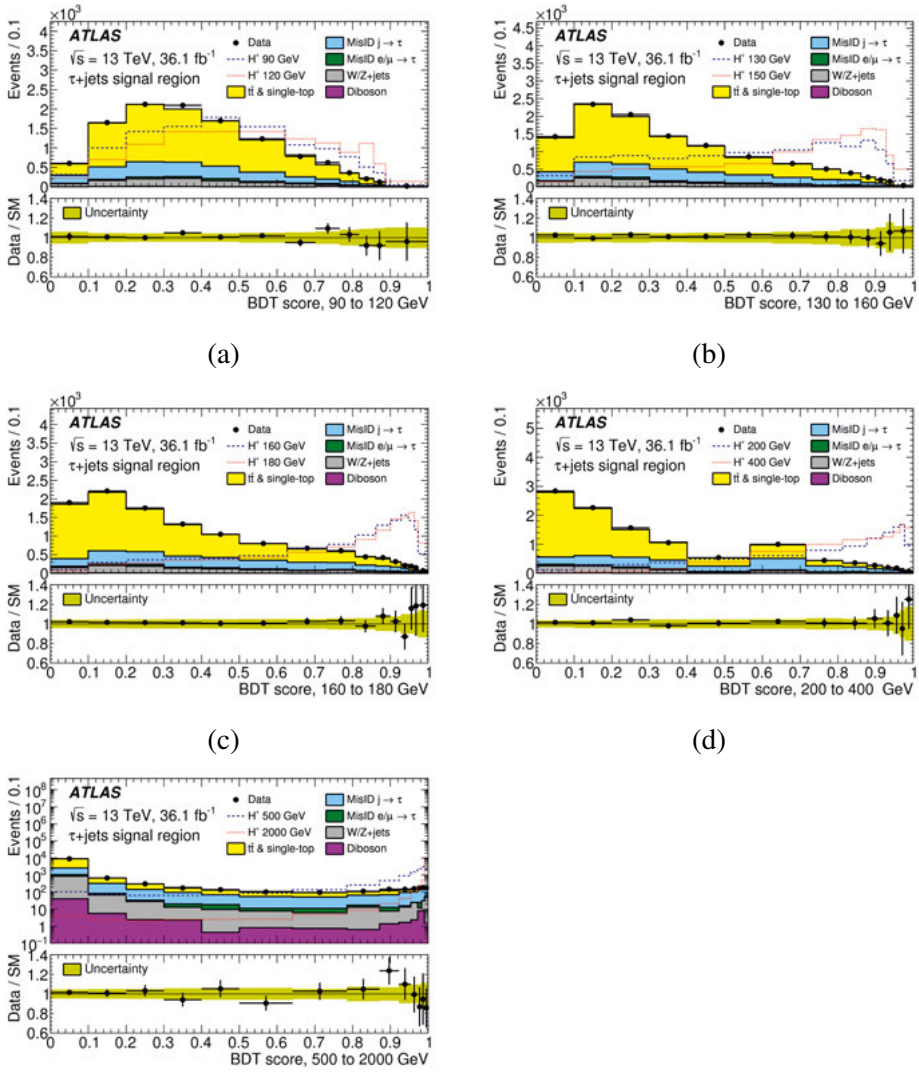

Figure 10.10. Distributions of the BDT score in the SR of the "tau plus jets" subchannel, in the five mass ranges used for the BDT trainings, after a fit to the data with the SM-only hypothesis. The lower panel of each plot shows the ratio of data to the SM background prediction. The uncertainty bands include both statistical and systematic uncertainties. The displayed signal is normalised to match the integral of the background. The figures are also available in [94].

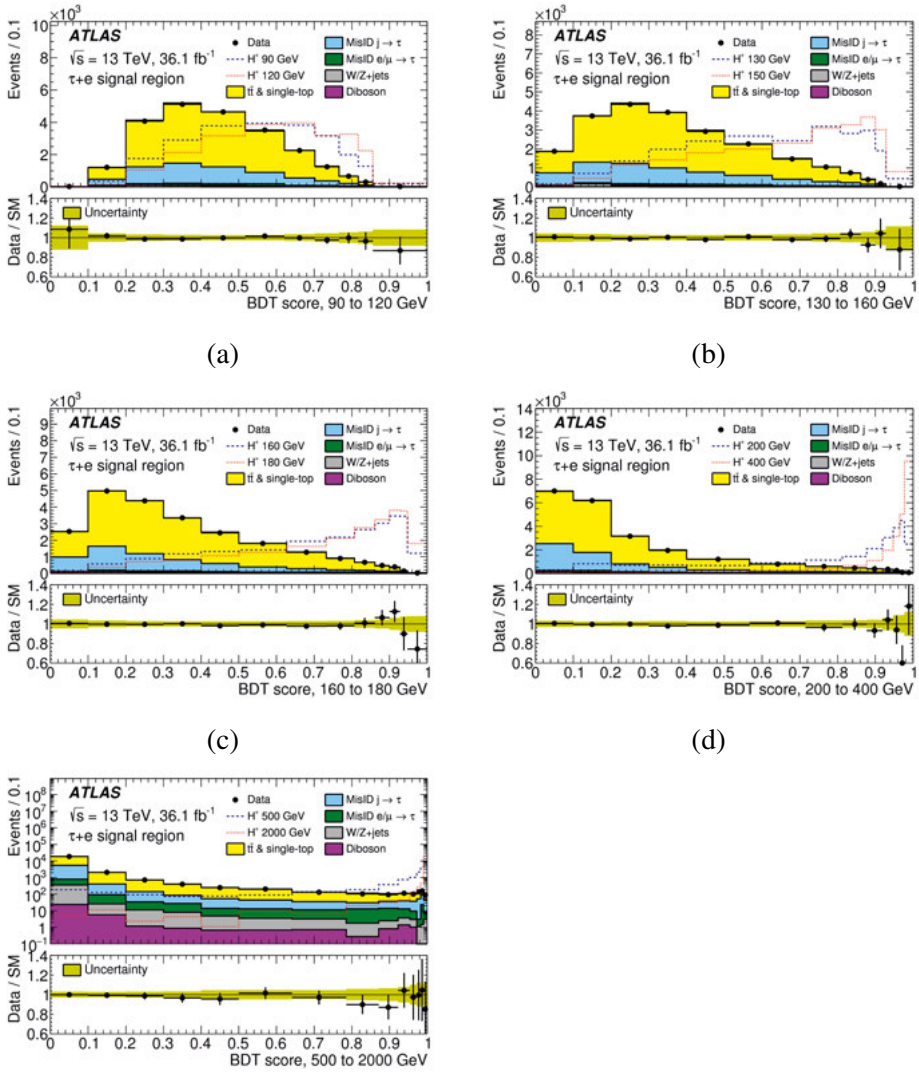

Figure 10.11. Distributions of the BDT score in the SR of the "tau plus lep(e)" subchannel, in the five mass ranges used for the BDT trainings, after a fit to the data with the SM-only hypothesis. The lower panel of each plot shows the ratio of data to the SM background prediction. The uncertainty bands include both statistical and systematic uncertainties. The displayed signal is normalised to match the integral of the background. The figures are also available in [94].

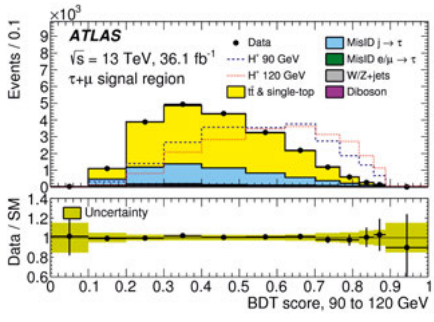

(a)

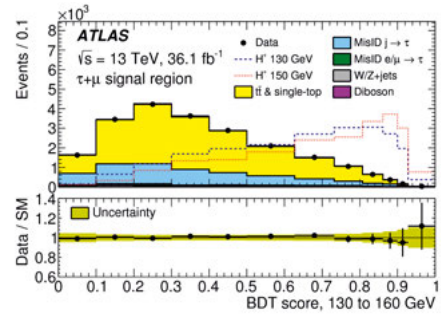

(b)

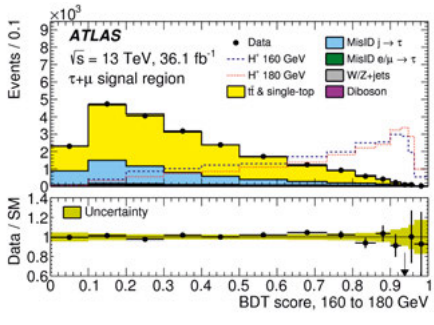

(c)

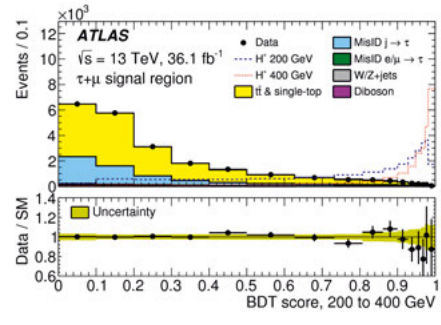

(d)

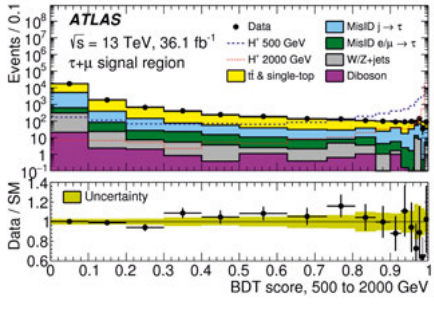

(e)

Figure 10.12. Distributions of the BDT score in the SR of the "tau plus lep(μ)" subchannel, in the five mass ranges used for the BDT trainings, after a fit to the data with the SM-only hypothesis. The lower panel of each plot shows the ratio of data to the SM background prediction. The uncertainty bands include both statistical and systematic uncertainties. The displayed signal is normalised to match the integral of the background. The figures are also available [94].

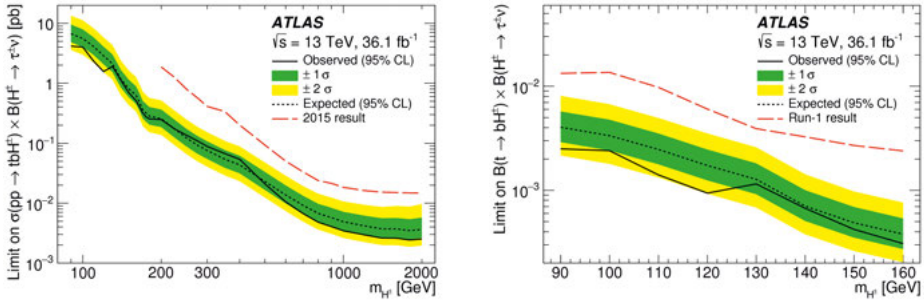

(a) (b)

Figure 10.13. Observed (*solid line*) and expected (*dashed line*) 95% confidence level exclusion limits on (a) $\sigma(pp \to tbH^{\pm}) \times BR(H^{\pm} \to \tau\nu)$ and (b) $BR(t \to bH^{\pm}) \times BR(H^{\pm} \to \tau\nu)$ with respect to the charged Higgs boson mass. The uncertainty bands of one and two standard deviations from the expected limits are plotted in green and yellow respectively. The areas above the observed limits are excluded. The dashed red line illustrates the obtained limits from a previous iteration of the study [83] for (a) and [98] for (b). The figure is also available in [94].

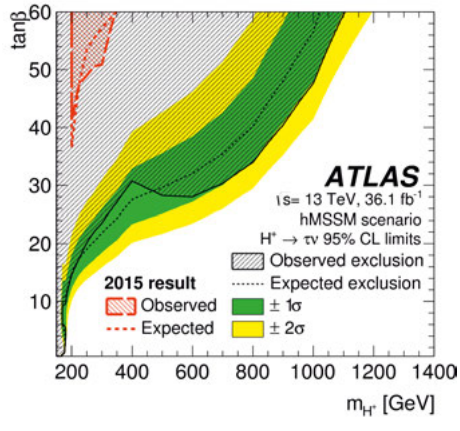

Figure 10.14. Observed (*solid line*) and expected (*dashed line*) 95% confidence level exclusion limits on the $tan(\beta)$ values, within the scope of the hMSSM scenario, as a function of the charged Higgs boson mass. The uncertainty bands of one and two standard deviations from the expected limits are plotted in green and yellow respectively. The areas above the observed limits are excluded. The dashed red line illustrates the obtained limits from a previous iteration of the study [83]. The figure is also available in [94].

Source of systematic uncertainty	Impact on the expected limit (stat. only) in % $m_{H^\pm} = 170\,\text{GeV}$	$m_{H^\pm} = 1\,\text{TeV}$
Experimental		
luminosity	2.9	0.2
trigger	1.3	< 0.1
$\tau_{\text{had-vis}}$	14.6	0.3
jet	16.9	0.2
electron	10.1	0.1
muon	1.1	< 0.1
E_T^{miss}	9.9	< 0.1
Fake-factor method	20.3	2.7
modelling	0.8	-
Signal and background models		
$t\bar{t}$ modelling	6.3	0.1
W/Z+jets modelling	1.1	< 0.1
cross-sections ($W/Z/VV/t$)	9.6	0.4
$H^\pm$ signal modelling	2.5	6.4
All	52.1	13.8

Table 10.4. *Impact of systematic uncertainties on the expected 95% CL limit on* $\mu = \sigma(pp \to tbH^\pm) \times BR(H^\pm \to \tau\nu)$. *The values have been calculated for two charged Higgs boson mass hypotheses:* 170 GeV *and* 1000 GeV. *The impact of each source of uncertainty is derived by comparing the expected limit if only statistical uncertainties (stat. only) were considered, with the expected limit when a specific set of systematic uncertainties is added in the limit-setting procedure. The last row of the table ("All") expresses the all-inclusive systematic uncertainties in the case where no correlations are expected between the systematic error sources and their uncertainties were Gaussian. The values were obtained by summing in quadrature (linearly) the individual contributions of the systematic uncertainties if these were much larger (smaller) than the statistical uncertainties. The table is also available in [94].*

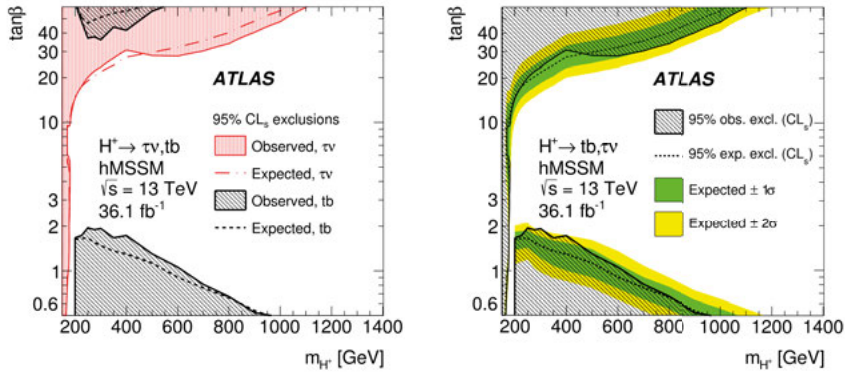

Figure 10.15. Expected and observed limits on $\tan(\beta)$ as function of $m_{H^\pm}$ in the hMSSM scenarios of the MSSM. The limits for each of the two final states are illustrated separately in (a); $\tau\nu$ in red dash-dotted curve and tb in black diagonally hatched areas. The 68% and 95% on the combined limits are illustrated in (b) as yellow and green bands respectively. The figures are also available in [84].

are $5-7$ times more stringent than earlier studies in the low and high mass regimes, and are the first limits set in the intermediate mass regime. In the context of the hMSSM scenario, the study concluded in an exclusion of all $tan(\beta)$ values for $m_{H^\pm} \leq 160\,\text{GeV}$, while for $tan(\beta) = 60$ all $m_{H^\pm} < 1100\,\text{GeV}$ masses are excluded.

The excluded range of $m_{H^\pm}$ and $tan(\beta)$ values from this study were also superimposed with the results from the ATLAS $H^\pm \to tb$ analysis [84] providing a summary of the ATLAS sensitivity to $H^\pm$ through the two decay modes. The limits from the $\tau\nu$ analysis presented here exclude a larger portion of the parameter space at high $\tan(\beta)$ values and low charged Higgs boson masses than the tb limits alone. The combination of the two analyses resulted in the 95% CL exclusion limits on $\tan(\beta)$ for the hMSSM as illustrated in Fig. 10.15.

Part IV:
High Luminosity LHC and the ATLAS detector upgrade

11. The High Luminosity LHC upgrade

The LHC has demonstrated excellent performance over its years of operation, and the amount of data acquired (Fig. 7.2) have made possible numerous studies from the experiments placed around the ring.

The current design however is limited for more sensitive physics studies that are still ongoing, such as the investigation of the SM shortcomings, the probing of BSM searches, etc. These types of studies require more data, to reduce systematic uncertainties, and higher energies, to reach more exotic processes at a significant sensitivity.

Both of these requirements motivate an upgrade to the current accelerator complex, leading to the conception of the High Luminosity LHC (HL-LHC) project. The project includes a large set of upgrade activities, the time-plan of which is illustrated in Fig. 11.1, that target to reach [99]:

- a peak luminosity of $5 \times 10^{34} cm^2 s^{-1}$ (with leveling[1]) allowing,
- an integrated luminosity of 250 fb^{-1} per year, aiming for a total 3000 fb^{-1} over the following twelve years of data taking.

Figure 11.1. The LHC upgrade plan towards the HL-LHC [100]. The collisions energy and the instantaneous luminosity values at the various phases are plotted with red lines in the upper and lower part of the plot respectively.

The upgrade is expected to benefit a large number of physics searches [101–104], building exciting prospects for what will be within reach in the upcoming years.

[1] "Leveling" implies that the design will aim for a "virtual" peak luminosity, limiting the event pileup while maximising the integrated luminosity.

The increase in luminosity however is also expected to strain the current detector systems placed around the LHC ring. Each of the experiments needs to redesign and upgrade parts of their detectors to be able to operate under the harder conditions and benefit from the rich physics prospects.

11.1 The ATLAS upgrade

The ATLAS detector will have to operate under much more demanding conditions, as the upgrade will result in more proton-proton interactions per bunch crossing at the detector's IP (pile-up) at higher luminosities. Presently the detector is faced with a mean of 55 pile-up events at a luminosity of $2 \times 10^{34}\,\mathrm{cm}^{-2}\mathrm{s}^{-1}$, while at the HL-LHC the number of mean pile-up will rise to 140 interactions at $5 \times 10^{34}\,\mathrm{cm}^{-2}\mathrm{s}^{-1}$, with a peak pile-up at 200 interactions. The conditions will result in higher particle fluxes (stressing the current detector in terms of occupancy and radiation damage) and larger collected data volumes, requiring operation at higher trigger rates.

A list of detector upgrades is planned to ensure its proper operation after the final HL-LHC upgrade phase. The upgrades include the replacement of the inner detector system by a new all-silicon detector system, referred to as the Inner Tracker (ITk) detector, the installation of a new detector system that will add high precision time information to the tracks registered in the forward ITk region [105], the addition of new chambers in the inner barrel Muon detector region and the design of a new trigger and data acquisition system [106]. The ITk is of high importance for this thesis and will be discussed thoroughly in Ch. 12. The upgrades on the TDAQ system are motivated by both the increase in rates and event sizes and will influence the upgrades in all other systems, and will be introduced in more detail.

The TDAQ changes aim to facilitate the physics goals, which require the triggers to maintain the same or better thresholds; especially for electrons and muons ($20-25\,\mathrm{GeV}$), while at the same time abiding to any constraints from the detector subsystems side (eg. constraints on the hardware trigger accept rate, the total latency, the buffering capacity, etc). The new TDAQ system will employ a hardware-based first trigger ($L0$) and a higher-level trigger (Event Filter), which relies on software algorithms running on CPU-based processing farms and a hardware-tracking system meant to share the load of charged particles' trigger level reconstruction. The L0 will operate at the collision rate of 40 MHz ("real time") and will rely on the new DAQ system (a combination of custom readout and commercial-off-the-shelf hardware components) to issue a trigger accept for the further readout at a rate of 1 MHz. The Event Filter will be running at the 1 MHz input rate and will provide its final output at a 10 kHz rate. All detector subsystems need to redesign their respective readout schemes to match the L0 real time operation.

A lot of exciting work is presently ongoing, bringing the ATLAS detector step by step closer to its final design. While preparing for what is to come, a lot of effort has been put into estimating the performance of the new ATLAS detector [107], in the unprecedented conditions of the HL-LHC, and set benchmarks for upcoming searches (some examples can be found in [108–115]).

12. The ATLAS Inner Tracker for the Phase-II upgrade

The ID is the first detector system encountering the products of the beam collisions at the ATLAS IP. The system was designed to operate efficiently for conditions of up to 23 pile-up events (much lower than the ones presently delivered) at $1.0 \times 10^{34}\,\mathrm{cm}^{-2}\mathrm{s}^{-1}$ instantaneous luminosity and it is already faced with limitations because of this design and the accumulated radiation on its aging components[1]. Looking ahead to fluences expected after the HL-LHC upgrade, the current ID will be retired and a new all-silicon (pixel and strip) detector system will be installed, composing the ITk system.

This chapter will cover the limitations of the current ID (Sec. 12.1), motivating the chosen ITk layout and design (Sec. 12.2). The focus will be on the strip detector systems (Sec. 12.3) and the production of the module units that will be placed on the end-cap section of the ITk (Sec. 12.4).

12.1 Challenges on the Inner Detector

The shortcomings of the ID system can be attributed to radiation damage, bandwidth saturations and occupancy in the subsystems.

Starting from the first on the list, while the subsystems of the ID were designed to withstand high amounts of radiation, the expected induced dose will render them inefficient. The pixel and SCT systems of the ID were designed for fluences up to $10^{15}\,n_{eq}/\mathrm{cm}^2$ and $2 \times 10^{14}\,n_{eq}/\mathrm{cm}^2$ respectively, which translates to a capacity of dealing with an integrated luminosity of $400\,\mathrm{fb}^{-1}$ in the pixel and $700\,\mathrm{fb}^{-1}/400\,\mathrm{fb}^{-1}$ in the SCT barrel/end-cap regions. In the same regard, the IBL can operate for up to $850\,\mathrm{fb}^{-1}$. This underlines the fact that, even without the upgrade, the components of the ID have an expiration date. The intrinsic efficiencies of the detectors would decrease below acceptable points in the next few years, affecting the pattern recognition capabilities of the system. Additionally, the high fluences are expected to lead to higher leakage currents, heating the system beyond the cooling systems capabilities and exceeding the allowed power supplies' limits.

The readout electronics on the pixel and SCT subsystems will face bandwidth saturations when attempting to cope with additional tracks per bunch

[1] The ATLAS detector saw its first event in 2008. At the proposed beginning of Run 4, following the HL-LHC upgrade, the components will be more than 15 years old.

crossing. The systems were designed to accommodate up to 50 pile-up events at a luminosity of roughly $2 \times 10^{34}\,\mathrm{cm}^{-2}\mathrm{s}^{-1}$, but beyond that threshold it is expected that they will be inefficient. From the pixel side, problems would arise from insufficient buffering of the data-links connecting the front-end pixel module electronics to the local read-out drivers, while from the SCT side the respective optical links would saturate, causing loss of data.

Lastly, the higher values of pile-up implies the presence of more tracks in the systems. The current SCT will not be able to resolve nearby tracks, while the TRT will reach its maximum occupance limit. These inefficiencies will affect the pattern recognition and track finding efficiencies, resulting also in an increase of recorded fake signatures.

These shortcoming already motivate changing the ID into a more robust and efficient design, solely from the perspective of detector capabilities, assuming the current readout system of the tracker. Operations in the HL-LHC conditions however will require, as already mentioned, the addition of a trigger output from the system that will be used as an input to the Event Filter trigger. The new readout scheme will necessitate additional changes in the tracker.

12.2 Inner Tracker layout and design

The ITk will use all the gathered knowledge and experience from the ID operation to overcome the limitations of the ID and serve as a more robust and efficient system. Its design is based on new technologies, more radiation tolerant than the ones used for the current system, and will use a new read-out scheme that will allow the implementation of the new track trigger.

The new detector needs to additionally meet all the requirements from the physics searches point of view for Run 4 and beyond, within a realistic cost plan. This extends over: hermeticity in the design, high reconstruction efficiencies, good track parameter resolution over a high p_T range, vertex reconstruction, jet flavor tagging, pile-up jet rejection and fake track suppression. Maintaining high reconstruction efficiencies and good nearby-track resolution at the high pile-up conditions is among the main mandates of the ITk. Both are essential for measurements of the transverse momentum and direction of isolated particles, i.e. electrons, muons, pions, etc, hard-scattering vertex reconstruction, b-quark jet identification, reconstruction of tracks within the core of high energy jets or from converted photons, as well as fake rate suppression. The reconstruction of vertices in the HL-LHC environment will be especially difficult close to the interaction point, due to the density of particles, which will complicate the tracking resolution. One way to address this is to optimize the layout in order to minimize the material budget; additional material deteriorates the tracking performance due to multiple scatterings and creates photon conversions and energy loss of particles.

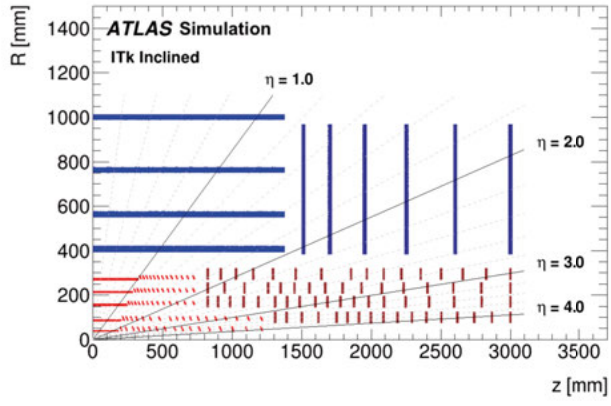

(a)

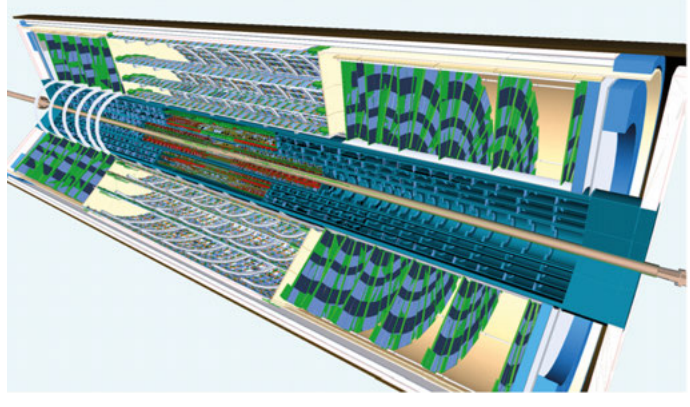

(b)

Figure 12.1. Schematic depictions of the ITk Layout [34].

The detector (Fig. 12.1) is built from pixel [116] and strip [34] detector layers covering a pseudorapidity area of $|\eta| < 4$ and $|\eta| < 2.7$ respectively. The pixel system is composed of five barrel layers, starting from a radius of about 34 mm, and an inclined section in the forward region, complemented by four ring layers in the end-cap section. The two innermost pixel barrel layers are expected to receive very large radiation doses over the full HL-LHC data-taking period and have been designed to be replaceable after roughly 2000 fb^{-1} (5 yrs.). The strip system (Sec. 12.3) is made of four barrel layers starting at a radial distance of 400 mm from the IP and six end-cap petal-design disks. The pixel and strip detectors combined provide a total of minimum 13 hits for $|\eta| < 2.7$ (except the barrel/end-cap transition region of the strip detector, where the hit count is 11).

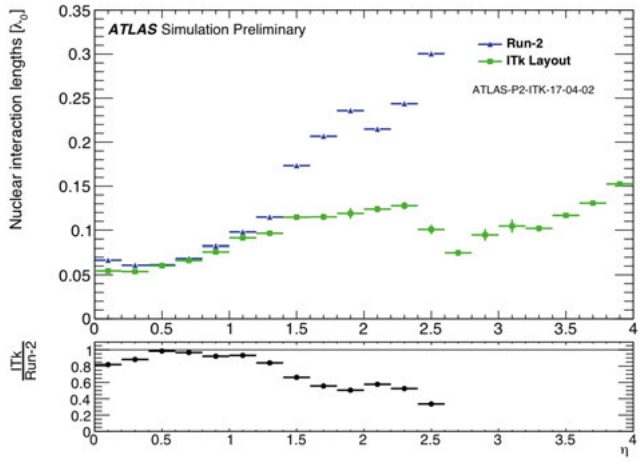

Figure 12.2. Number of nuclear interaction lengths encountered by a particle as a function of pseudorapidity for the ITk layout (green) and the Run 2 inner detector (blue). The figure is also available in [117].

The layout was chosen taking into consideration the overall cost of the structure and also the CPU needs for the subsequent reconstruction. The cost was minimized as much as possible by reducing the silicon surface in the detector (which also addressed the material budget concern mentioned earlier), without compromising the hit coverage, and by choosing less complex solutions whenever possible. The number of nuclear interaction lengths encountered by a particle in the ITk layout is plotted in comparison to those encountered in current ID during Run 2 conditions, as a function of pseudorapidity, in Fig. 12.2.

Simulation studies with the final layout and reconstruction methods of the ITk have been carried out for the expected pile-up conditions on $t\bar{t}$ decays, to evalute its performance. The results demonstrate comparable track reconstruction efficiency for hard-scatter tracks with $p_T > 1\,\text{GeV}$ with respect to the one achieved with the Run 2 detector for $\mu = 20$ (Fig. 12.3) and much better fake rate suppression (Fig. 12.4).

12.3 The Strip detector sub-system

The strip detector covers an overall silicon area of roughly $165\,\text{m}^2$. The four cylinders composing the strip barrel region extend up to $|z| < 1.4\,m$, while the six end-cap disks (on either side) extend up to $|z| < 3\,\text{m}$.

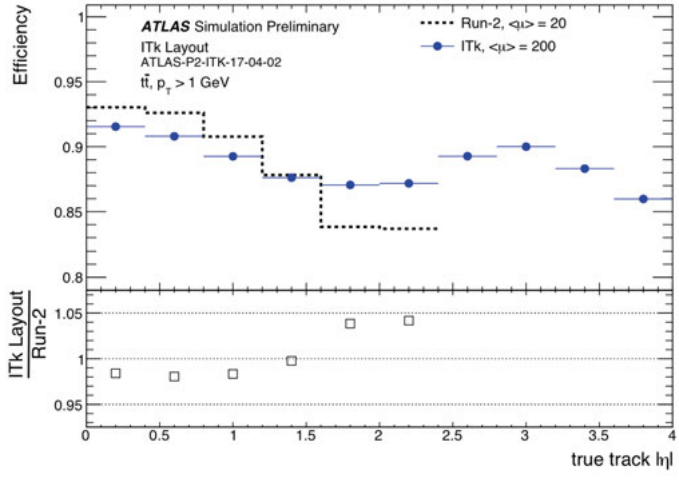

(a)

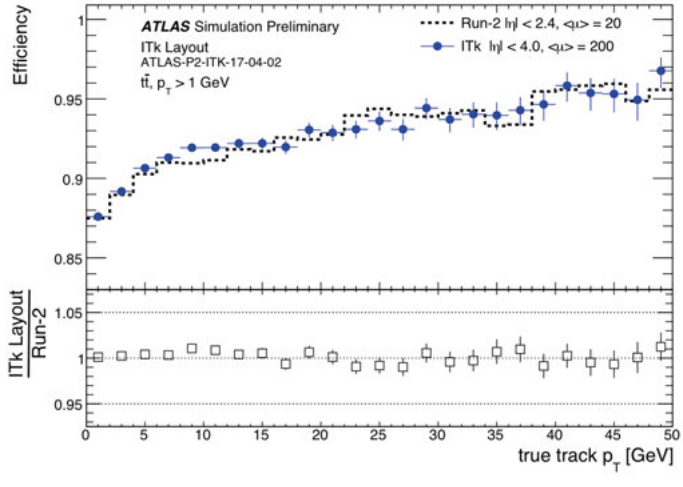

(b)

Figure 12.3. Track reconstruction efficiency of the ITk detector for hard-scatter tracks with $p_T > 1\,\text{GeV}$ from $t\bar{t}$ decays at $<\mu> = 200$ with respect to η (a) and p_T (b). The efficiency is compared to the achieved ID Run 2 efficiency at $<\mu> = 20$. The bottom plots include the ratio of the expected/achieved (ITk/ID) efficiencies from the two systems in their respective pile-up conditions. The figure is also available in [117].

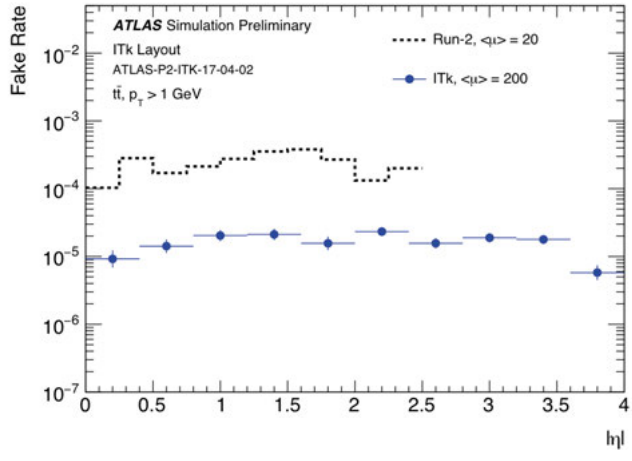

Figure 12.4. Fake rates of the ITk detector for hard-scatter tracks with $p_T > 1\,\text{GeV}$ from $t\bar{t}$ decays at $<\mu> = 200$ with respect to η. The efficiency is compared to the achieved ID Run 2 efficiency at $<\mu> = 20$. The figure is also available in [117].

12.3.1 Support structures

The two strip regions share a similar structural philosophy and share the same basic unit, called a module, yet the module shapes differ to match the needs of each region. The module (discussed in more detail later in the text) is the combination of a microstrip silicon sensor, one or two polyimide based multi-layer flexible PCBs that carry custom readout ASICs ("hybrids") and a powerboard. The modules are placed in local structures, which are then combined on the corresponding global structures. Starting from the full detector picture and breaking the structure down, the strip subsystem has three global structures; one for the barrel and two for the end-cap regions (Fig. 12.5). The barrel global support is composed of local support units called Staves (392 in total), while the end-cap equivalents are called Petals, (384 in total, i.e. 32 per disk). The format of the Staves and Petals are illustrated in Fig. 12.6.

The Staves host two types of module geometries; the "short strip" (or "SS") geometry in the inner two layers, with four rows of 24.1 mm length strips, and the "long strip" (or "LS") geometry in the outer two, with two rows of 48.2 mm length strips. Both geometries share the same size of $97.54 \times 97.54\,\text{mm}^2$ and have a strip pitch[2] of $75.5\,\mu\text{m}$ and are arranged as illustrated in Fig. 12.6. The modules are mounted on either side of the Stave, with a $26\,\mu\text{rad}$ angle rotation, offering a total stereo angle of $52\,\mu\text{rad}$.

The Petal hosts six different geometries in order to provide hermetic coverage, named as $R0$, $R1$, ... and $R5$ to differentiate them according to their

[2] "Pitch" refers to the distance between the strips.

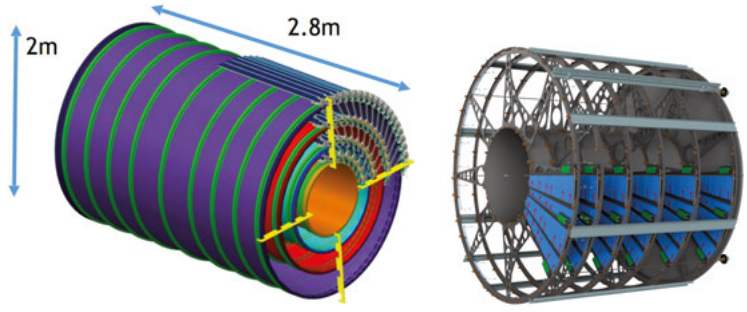

(a) (b)

Figure 12.5. Global structures of the ITk strip subsystem in the barrel (a) and the end-cap (b) regions [34].

placement, since the module shape changes depending on the radius. The sensor sizes change according to the radius, yet they all share a wedge-like shape (which offers a sensitivity in hit measurements with respect to ϕ), where both the lower and upper edges are designed as parallel arcs to allow for equal strip lengths. Similarly to the Staves, the modules are mounted on either side of the Petals, but the module strips are arranged to be perpendicular with respect to the beam axis, within a stereo angle offset. Each module offers a 20 mrad stereo angle (40 mrad total angle from the modules on either side) measurement, which is built into the strip layout (Fig. 12.7)[3]. The strip pitch is as close to 75.5 μm as possible.

The length of the strips in all types (barrel/end-cap) of modules is correlated to the expected occupancy in that location. Closer to the beam region the expected hits per collision is larger than further away and shorter strips are employed to accommodate the occupancy levels.

12.3.2 Modules

Sensors

The core of the module is the sensor; which in this case are microstrips with n-type implants in a p-type float-zone silicon bulk (n-in-p FZ), produced by Hamamatsu Photonics. The structure was described in detail in Sec. 5.2 and only a short overview will be given here for continuity.

In the discussed design, electrons act as the charge carriers and are collected from the implant side, which is readout via a metalization layer on top of the implants. The signal is transferred to the metal layer via a capacitive coupling through the SiO_2 isolation layer (AC coupling). The strips are biased with

[3]The rotation cannot be achieved by positioning the modules at an angle due to space constraints.

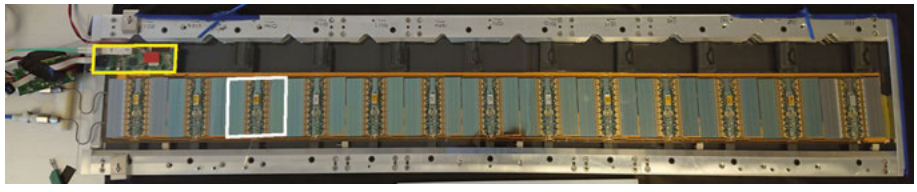

(a)

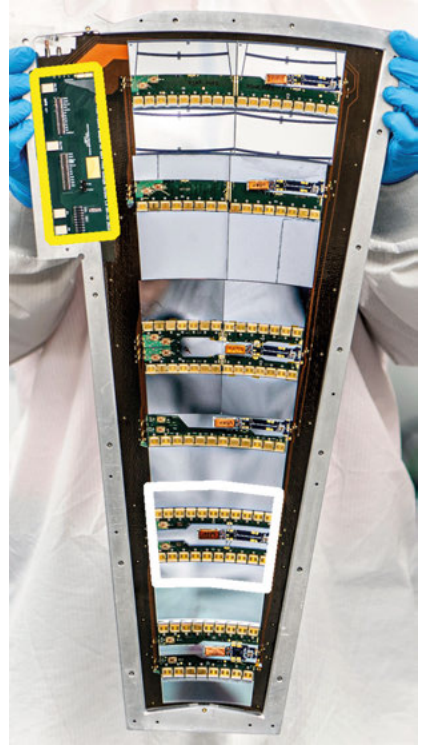

(b)

Figure 12.6. Local structures of the ITk strip subsystem; “Staves” in the barrel (a) and “Petals” in the end-cap (b) regions. The white rectangles mark the modules that are mounted onto the local supports. The yellow rectangles mark the end-of-substructure cards for each structure. Details can be found in the text. The pictures are also available in [118].

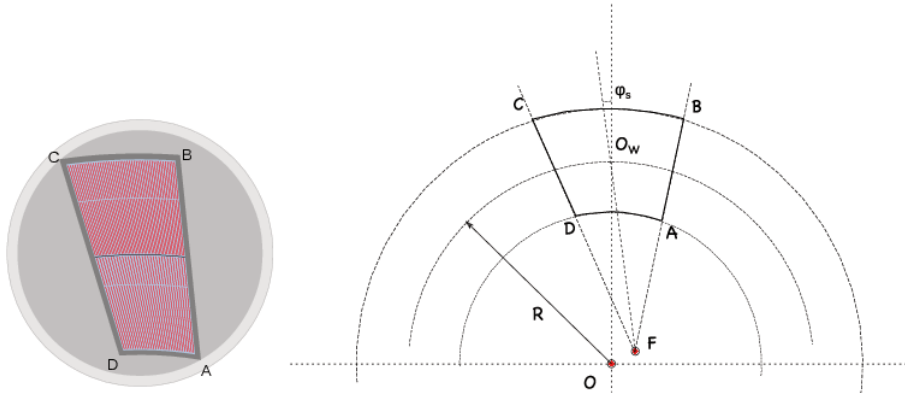

Figure 12.7. Illustration of strip end-cap sensor geometry. The sensor are laid out in a 6-inch wafer to achieve maximal area employment (left). Points A, B, C and D indicate the corners of the sensor. The strips in the sensor are laid out with a built-in, small stereo angle, $\phi_s = 20\,\text{mrad}$, and point to a common focal point, F, as do the lateral sides of the sensor to avoid truncated strips. The figure is also available in [119].

polysilicon resistors and an inter-strip isolation is achieved by the addition of p-stop implants. The physical thickness of the sensor is $320 \pm 15\,\mu\text{m}$.

The big advantage of the n-in-p sensor type is that they do not suffer from radiation induced type inversion, which was an essential requirement during the R&D phase. Additionally, the charge collection is based on drifting, allowing operation in partial depletion conditions and also faster signal collection (largely due to the collection of electrons), which in turn implies lower trapping effects. One caveat of this sensor type if the requirement to apply the bias on the sensor edge, but this has been taken into account in the design of the biasing and support scheme.

Hybrids & ASICs

The readout of the sensors is performed in a hybrid form, as it relies on additional external components for the readout of the signal. The collected charge is transferred through wire bonds to custom made ASICs mounted (glued) on low mass flexible PCBs, named "hybrids". The ASICs are procuded by Global Foundries and are of two types; the ones responsible for converting the measured charge deposition on the detector, called ATLAS Binary Chips (or ABC in short) and equipped with 256 readout channels[4], and the ones responsible for the collection and further transmission of the collected information from the individual ABCs on the local structures, called Hybrid Controller Chips (or HCC in short).

Two ABC/HCC ASICs have been developed; the ABC130/HCC130 ASICs, which are being used during the prototyping phase, and the ABC-

[4]Each readout channel corresponds to the readout of an individual strip on the sensor

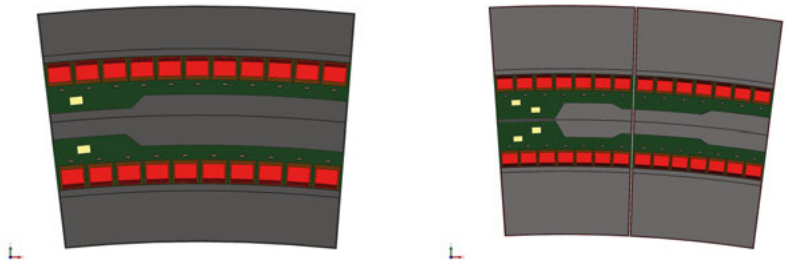

(a) (b)

Figure 12.8. Illustration of the R1(a) and R3 (b) end-cap module types [34].

Star/HCCStar ASICs, aimed for the final module production. Both are based on CMOS technology but they have different readout architectures. The Star versions improved observed problems in the 130 ASICs, such a susceptibility to single-upset event errors and demonstration of TID-effects. A triple-vote logic was adopted to address the first, while a different logic circuitry was developed to address the latter.

Concerning the ABC ASICs, the first part of the readout architecture is the front-end block. The front-end block is responsible for the reception of the analog sensor signal (collected charge) and its amplification, shaping and discrimination, converting it into a final binary hit or no-hit information. The front-end consists of an amplification stage where a charge sensitive preamplifier converts the analog input charge signal into a voltage signal, and a subsequent discrimination stage where the voltage amplitude is compared to a threshold, yielding the hit/no-hit information. The threshold values can be trimmed for each individual channel, allowing to take deviations into account and resulting in a uniform response over all channels. One limitation of this type of binary system, is that the pure charge information from the hit is lost. The discrimination approach only focuses on the number of strips above the threshold, without retaining any information on the ones below. The analog response can be studied with a statistical method called threshold scan[5]. The outputs of the discriminator are sampled at the bunch crossing rate and stored in a designated buffer for a fixed (programmable) latency. If an L0 accept signal is received, the data are transferred into subsequent logic blocks, which differ between ABC130 and ABCStar. Details on the logic block sequence can be found in [34]. The final output of the ASIC are transmitted to the HCC (after the HCC issues a request) at a 160 Mbit/s rate through a bus on the hybrid. The data flow communication among the ASICs is done in series and "daisy-chained" for the ABC130/HCC130 case and in parallel for the ABCStar/HCCStar case (Fig. 12.9).

[5] Appendix B.

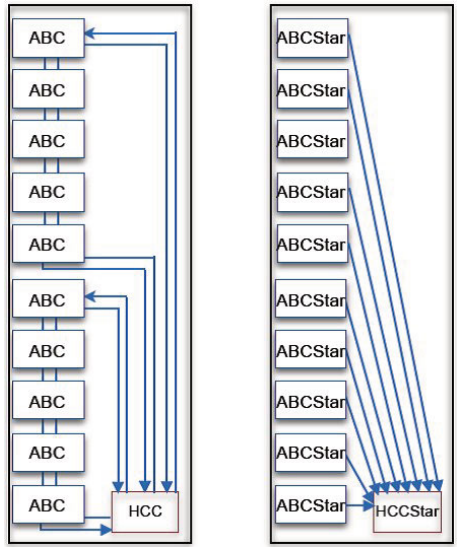

Figure 12.9. Data flow for the 130 (left) and Star (right) ASIC types [34].

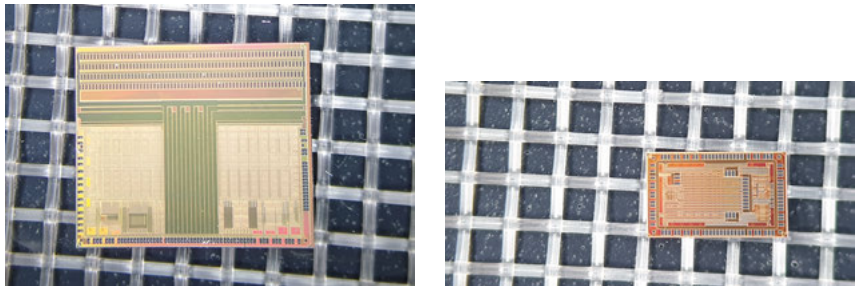

(a) (b)

Figure 12.10. Pictures of the ABC130 (a) and HCC130 (b) ASICs.

Once the HCC collects the ABC outputs, it processes the collected hit information and proceeds to transfers it to the EoS bus card, at a 640 Mbit/s rate through a bus tape. The EoS collects the outputs of all the HCCs on the local support structure (Stave/Petal) and transfers them though optical links to the global support structure. Conversely the EoS card provides Trigger, Clock and Control (TTC) signals to the HCCs, which are distributed to the ABCs.

Powerboards

The powerboard is responsible for the powering of the electronics hosted on the hybrids. The final design consists of a DC-DC converter, a custom Autonomous Monitoring and Control ASIC (AMAC), and a high voltage bias filter. The prototype version is similar but is lacking the AMAC ASIC

Module types	Num. of Sensors	Num. of Strips	Num. of Hybrids	Num. of ABC ASICs (/hybrid)	Num. of HCC ASICs (/hybrid)
Barrel - SS	1	5120	2	10+10	1+1
Barrel - SS	1	2560	1	10	1
EC - R0	1	4352	2	8+9	1+1
EC - R1	1	5376	2	10+11	1+1
EC - R2	1	3072	1	12	2
EC - R3	2	7168	(2)+(2)	(7+7)+(7+7)	(0+2)+(0+2)
EC - R4	2	4096	(1)+(1)	(8)+(8)	(0)+(2)
EC - R5	2	4608	(1)+(1)	(9)+(9)	(0)+(2)

Table 12.1. *Strips sensor modules composition. The Table lists the number of sensors, readout strips, hybrids and ASICs consisting each type of module. "EC" stands for "end-cap". In the case of the outer ring end-cap modules (R3, R4 and R5) the modules require 2 sensors and the numbers in the respective columns are listed in parentheses to indicate the sensor they correspond to.*

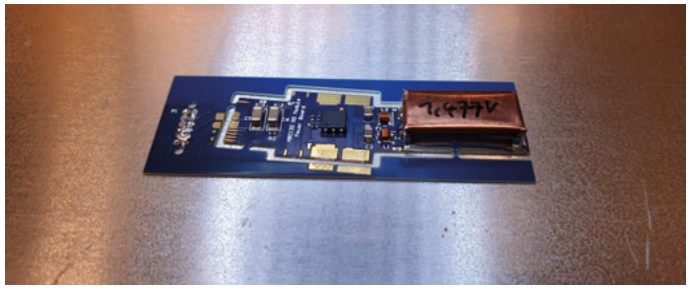

Figure 12.11. Picture of a prototype powerboard.

(Fig. 12.11). The bus tape connecting the modules to the local structures provides a low-voltage supply of 12 V on each module. The DC-DC converter is used to deliver the 1.5 V necessary for the ASICs operation. The AMAC is carrying out measurements of temperature, voltages and currents. Additionally it is in charge of the low voltage control and the high voltage switch. The high-voltage switch is an important feature as it allows the isolation of potential ill-operating sensors.

12.4 Production of end-cap strip detector modules

The production of the Staves and Petals is distributed across different sites. Here the focus will be on Petals and more specifically on the workflow required for the production of the modules.

The load of the full ITk end-cap global assembly has been divided among two institutes; DESY and NIKHEF. The two sites will be receiving loaded

Petals from four distinct clusters of institutes. Each cluster is responsible for sharing the workload of producing the individual modules required for the Petal.

The work described in this thesis is seeding one of these four clusters, the "Valencia" cluster, and will thus be used as an example. The cluster will perform the Petal loading at the Instituto de Fisica Corpuscular (IFIC) in Valencia (which motivates the name). The $R0$ and $R5$ module types are prepared in the same institute, while the $R2$ and $R4$ are prepared at the Institute of Particle and Nuclear Physics (IPNP) of Charles University in Prague. The $R1$ and $R3$ module types are prepared by the Scandinavian group of institutes. The Scandinavian group of institutes is consisted of Uppsala (UU) and Lund (LU) Universities in Sweden, the Niels Bohr Institute (NBI) in Denmark and the University of Oslo (UiO) in Norway. The hybrids necessary for the module production are provided by external institutes in the case of IFIC and IPNP, while the Scandinavian group prepares them within its own workflow. The powerboards will be centrally provided and the sensors will be distributed by IPNP.

The focus here will be on the module assembly procedures within the Scandinavian group of institutes. The workflow is unique, when compared with other sites, because of its collaborative nature among multiple institutes and, most importantly, its collaboration with an industrial partner. The Scandinavian group has decided to collaborate with an electrical and electronic manufacturing company called NOTE[6], located close to UU, for the assembly and partial bonding and testing of all hybrids and modules. The development of the industrial production workflow is expected to benefit greatly the parallelization of the work, while offering high-standard machines and trained personnel for the various procedures during production.

All produced detector components need to operate reliably over the full expected lifetime of the detector and thus a series of Quality Assurance (QA) and Quality Control (QC) test procedures need to be followed throughout the production. First, the general module production steps will be introduced, followed by an overview of the Scandinavian group workflow and the adaptations needed for moving the procedures in industry.

The step-by-step procedure for preparing a full module is broken down to the following tasks:

1. Reception of bare components (sensors, hybrid PCBs, ASICs, powerboards) and testing.
2. Assembly of hybrids (gluing and bonding of the ASICs) and testing.
3. Assembly of modules (gluing and bonding of loaded hybrids and powerboard) and testing.
4. Shipment to the Petal loading site.

[6] `https://www.note-ems.com/en/`.

A common, collaboration-wide, database has been developed for the monitoring and log-keeping of procedures and will be used during production. All steps listed in the following are logged in to the database.

Step-1: ***Reception of components***
The sensors are shipped to the module production sites in groups within a common box but with individual packaging for each sensor. Upon reception, a module production site should first perform a visual inspection of the external packaging for any damages. The inspection should be performed within the first seven days and any problems need to be reported and documented. The external packaging is then removed and the ESD-safe wrapping is also examined for any potential defects. The sensor at this stage is transported into the cleanroom facilities[7] for its further examination and storage. The shipment packaging includes a humidity sensor and the humidity should not have exceeded 10% during transport. The reception tests include a visual inspection, looking for clear scratches, deposits or defects (especially along the edge or bias/guard rings) and a reverse bias leakage current (IV) measurement. The IV measurements are performed up to 700 V in reverse bias voltage with increments of 10 V per 10 s. The maximum voltage is kept for at least 30 s, during which multiple samples are taken to ensure the sensor is stable. The sensor needs to remain below the compliance limit of $10\,\mu$A. The handling needs to be done primarily with clean vacuum suction cups, made from a soft and anti-static dissipating material, avoiding any unnecessary handling altogether. At a second stage the sensor needs to be equipped with a straight, polyamid isolated thin aluminum cable, called high voltage tab. The high voltage tab allows the connection between a high voltage pad on the power board and the sensor back plane. The attachment needs to be done using ultra sonic welding on the back side of the sensor, with a bond wedge without wire. The IV of the sensor is repeated after that step, to ensure that no damage was inflicted during the attachment.

The hybrids are received in the form of panels, hosting a number of hybrids and some test structures. The reception QC includes visual, mechanical and electrical tests. The visual inspection concerns any damages or scratches on the hybrids, misplacement of the passive components on the boards or residuals on the bonding pads. The electrical tests are performed on the test coupons available on each panel and evaluate aspects such as the wire-bond pull strength and the thickness of the hybrids.

The ASICs are delivered in gel-packs. Their reception tests include visual inspection of the ESD-safe packaging and the individual ASICs in terms of damages or scratches. Additionally, the encountered humidity levels during transport is also monitored.

[7] ISO-7 or better, with stable temperature of 21 ± 2 C and a relative humidity of $35 \pm 15\%$.

Powerboards are distributed to all module production sites in panels and each receiving site needs to perform a visual inspection and a set of electrical tests. The inspection needs to be carried out in the cleanroom area, using a microscope and needs to evaluate whether the powerboard has any missing, damaged, misplaced or misaligned components, if there is any glue seepage of solder remnants on the surface, missing and/or damaged wire-bonds, or debris and/or physical contaminants. A minimal electrical testing setup will also be used upon reception. to ensure proper functionality before use. The tests concern basic functionality aspects, such as having a reliable communication with the AMAC and working outputs, and being able to turn on/off the low/high voltage output supply, and full characterization tests such as the DC/DC efficiency and the AMAC current monitoring. If any of the mentioned problems is encountered, the baseline scenario assumes that the powerboards are not fit for the module production and the problems are reported.

All components are stored in the aforementioned cleanroom standards, to ensure the appropriate humidity, temperature and particle count conditions.

Step-2: ***Hybrid assembly and testing***
The hybrid assembly needs to be done within a strict set of specifications, concerning ASIC placement, proper component support and final weight and thickness.

The ASICs are attached with a UV-curing glue [8]. The glue is stored in a dry and dark environment, at a temperature between 8 C and 21 C, prior to use and needs to be transferred to UV-safe syringes. The glue needs to offer good support for bonding and mechanical rigidity, without any spillage on the bonding pads of the hybrid. The optimal specifications that would offer these qualities are a roughly 70% pad coverage at a glue layer thickness of $120 \pm 40\,\mu$m[9], which translate to an amount of 4.20 ± 0.25 mg and 1.5 ± 0.1 mg under the ABC and HCC ASICs respectively. The glue weight is established by comparing the weights of the individual components (hybrid and ASICs) before the assembly and the final weight of the completed hybrid.

The assembly procedure changes depending on whether it is performed in an institute or within industry. In either case, the hybrid needs first to be removed from the common panel and weighted.

In the case where the assembly is performed in institutes, the placement is carried out with dedicated tooling (Fig. 12.12), which ensure the height and x-y placement of the ASICs on the pads[10]. The hybrid is sucked down on the support jig, which is equipped with alignment pins for the ASIC mounting and a UV LED ($\lambda = 405$ nm) structure for the curing. The ASICs are placed on a chip tray that is cut for precision placement and picked up with the custom

[8] Loctite 3525 [120].

[9] The thickness is designed to guarantee a good penetration of UV light for curing, while maintaining good support.

[10] Details can be found in Appendix B.

vacuum suction tool. Once both the hybrid and ASIC components are ready, the glue is dispensed using a 5-dot pattern (for better coverage and uniform thickness under the ASIC) on each of the hybrid pads. Then the ASIC pick-up tool is lowered down on to the hybrid and the LEDs are switched on until the glue is fully cured ($\sim 120\,\mathrm{s}$). The pick-up tool is designed to leave the desired $120\,\mu\mathrm{m}$ gap for the glue thickness. Each module type has their designated list of tools that match their characteristic geometry.

In the case where the assembly is carried out in industry the assembly workflow is a bit different. In these cases, a pick-and-place machine is employed, like the one shown in Fig. 12.13. The hybrid is placed on a support jig similar to the one mentioned earlier, but with adaptations so that it can be mounted on the pick-and-place machine. The alignment pins and LED structure are not needed in this design. The ASICs are mounted on either waffle-packs and loaded in the machine trays, or in some cases they can remain in the original gel-packs. The machines are typically equipped with glue dispensing and UV curing systems and can be programmed within the placement sequence. The machines rely on optical pattern recognition on the ASIC and hybrid pad surfaces for the lifting, alignment and placement of the ASIC. The $120\,\mu\mathrm{m}$ glue thickness can be achieved by programming a fixed height offset from the pad surface or by manufacturing a custom pick-up tool head that matches the machine system (this will be discussed in more detail later on in the text). Once the hybrid is loaded into the machine and the ASICs' cases are mounted as well, the sequence carries on sequentially as follows: a 5-dot pattern is dispensed on one hybrid pad, an ASIC is lifted from the waffle-/gel-pack and then placed on the pad, the UV curing is turned on for 10 s and only after the necessary time has passed are the LEDs turned off and the pick-up head releases the vacuum. The precision-alignment of the ASIC is done from its back-side with respect to the cut edges and the pick-up is done using the lithography, ensuring that the ASIC will not be rotated by mistake. The same sequence is repeated for all the remaining pads on the hybrid. Once the last ASIC is placed, the LED curing is switched on again for an additional 120 s to fully cure the glue under the ASICs.

Finally the hybrid is ready to be loaded in to a designated burn-in panel, using vacuum suction tools. This structure hosts a number of hybrids together and allows the parallelization of the latter procedures, namely the metrology, bonding and testing (electrical/thermal). A metrology test needs to be performed after placement to ensure that the x-y positions are within tolerances and that the heigh uniformity across the hybrid is within specification. The height uniformity is crucial both for the bonding of the ASICs to the hybrid and the later assembly onto the module, where it is important to have good planarity for the tools. Electrical and thermal (burn-in) tests are performed to ensure proper functionality and discard cases of ASIC infant mortality before mounting the hybrids on to the sensor. All tests are described in detail in Appendix B.

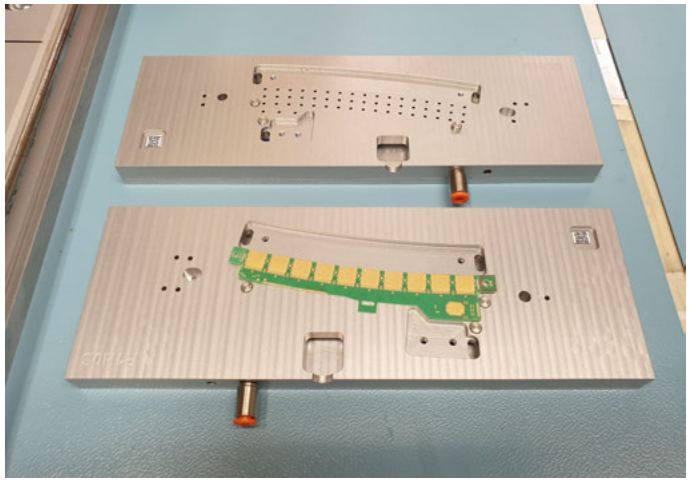

(a)

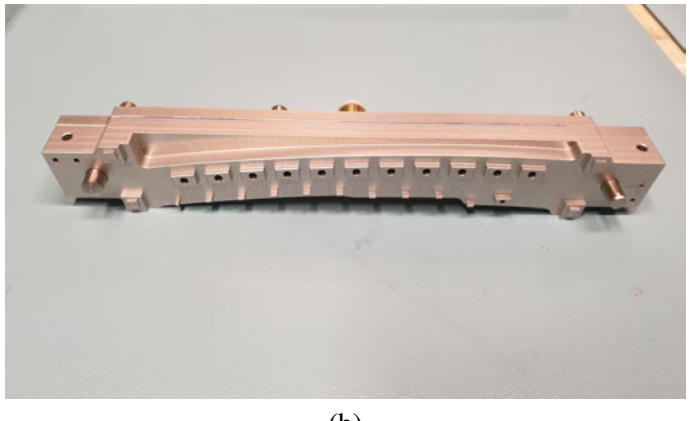

(b)

Figure 12.12. Tools for the ASIC-to-Hybrid placement. The hybrid support jig is shown in (a), while the ASIC pick-up jig in (b). In (a) one can also see the pockets that are meant for the UV-curing structure.

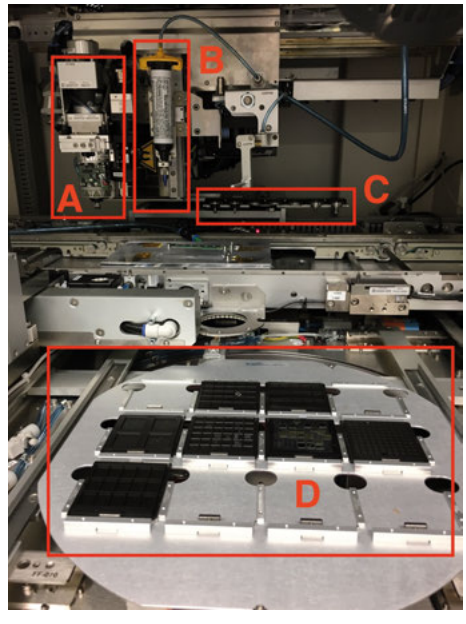

Figure 12.13. Example of a DATACON pick-and-place machine, which was also used at NOTE for prototyping. A pick-up tool (A) is used for the ASIC (D) lift-up and placement. A glue dispensing system (B) is available in the machine, while a holder for replacement tools (C) can also be used if necessary. The hybrid sits in the center of the picture. The photo has been taken from the ITk Strip end-cap assembly procedures documentation.

Step-3: ***Module assembly and testing***
The module assembly is performed after all of the required components (sensor, assembled hybrid and powerboard) are prepared and tested. Before initiating the assembly, all components are weighted individually. The mounting procedure is carried out in stages, because of the chosen adhesive and the tooling design. The technical requirements for the adhesive include mechanical stability of the final structure (essential during bonding), radiation hardness and thermal conductivity (allow heat dissipation during operation). A two-part epoxy glue[11] successfully meets these requirements and will be used throughout the production. The glue cures chemically with time, resulting in some complications that will be discussed further in the text.

A dedicated set of tooling (one for each of the module types) is used for the full assembly. The sensor is placed in a support jig which includes a vacuum suction system to keep it in place (Fig. 12.14). The jig is equipped with alignment pins for the component mounting. The assembled hybrids are placed in support jigs, designed to ensure proper alignment, and picked-up with suction tools (Fig. 12.14). The glue is mixed and dispensed on either the sensor or the back side of the hybrids, using stencils or a glue robot. The procedures vary between the sites, but need to meet the same specifications; no leakage of glue on undesirable places of the sensor (especially the front-end bonds and the guard ring), sufficient support under the hybrids and a total uniform thickness of $120 \pm 40\,\mu$m. The distance between the sensor and the hybrid is critical to get sufficient electrical isolation between the two and to maintain an adequate thermal path from the hybrid trough the sensor to the cooling. After the glue dispensing, the hybrids are lowered down on to the sensor. The jigs are left with the vacuum suction on for ~ 12 hrs. while the glue cures. Weights are added on top to ensure a uniform glue spread. The tools ensure the desired height offset. Once the hybrids are mounted, the same sequence of steps is repeated for the powerboard. The placement of the powerboard follows a similar procedure. The procedure needs to be broken down in these two stages because of the overlap of the pick-up tools.

The glue handling is non-trivial because of the time-sensitive curing. The two components of the glue need to be weighed with sufficient precision to ensure the correct mixing ratio[12]. The weighting is performed in individual containers and then mixed together for $30 - 180$ s. The acceptable working time has been determined to be up to 35 and 60 minutes at 25 C, when using a stencil or glue robot respectively. Because of the curing, the viscosity of the glue is different as time progresses and this needs to be accounted for when using glue robots. This is addressed by varying the pressure or speed while

[11] Polaris PF 7006A [121].
[12] Mix ratio by weight should be: 100/9.

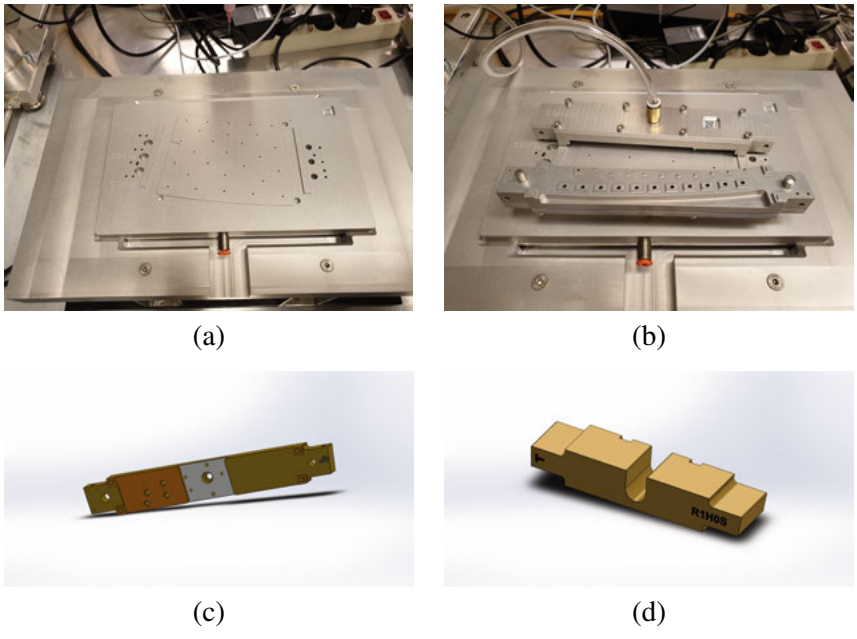

(a) (b)

(c) (d)

Figure 12.14. Tools for the Hybrid/Powerboard-to-Module assembly. The pictures show: the sensor support jig (a), the hybrids pick-up tools (b), the powerboard pick-up tool (c) and the weights (d) for the $R1$ module type.

dispensing the glue paths, targeting to keep the same amount of glue through out the acceptable working window.

Once the assembly is completed the final module is weighted and the weight of the glue is extracted. A visual inspection is performed to check for any glue leakage, as well as a metrology test to evaluate the height and positioning of the components. An IV test is also performed to test for early breakdown. Finally, the module is placed on a designated test-frame and wire-bonded, which allows further tests (metrology, thermal and electrical). All tests are described in detail in Appendix B.

Scandinavian workflow

The Scandinavian group of institutes will follow the procedures mentioned above for the production of the $R1$ and $R3$ hybrids and modules. Some modifications in the nominal workflow will be made to achieve best incorporation of the procedures into the industrial workflow of NOTE and the distribution of the work among the sites.

The latest flow chart is presented in Fig. 12.15.

Following the list of steps presented earlier; the reception of all the components (as described previously) as well as their subsequent transport to NOTE will be carried out by UU. The components are stored at the industrial site until they are needed for production.

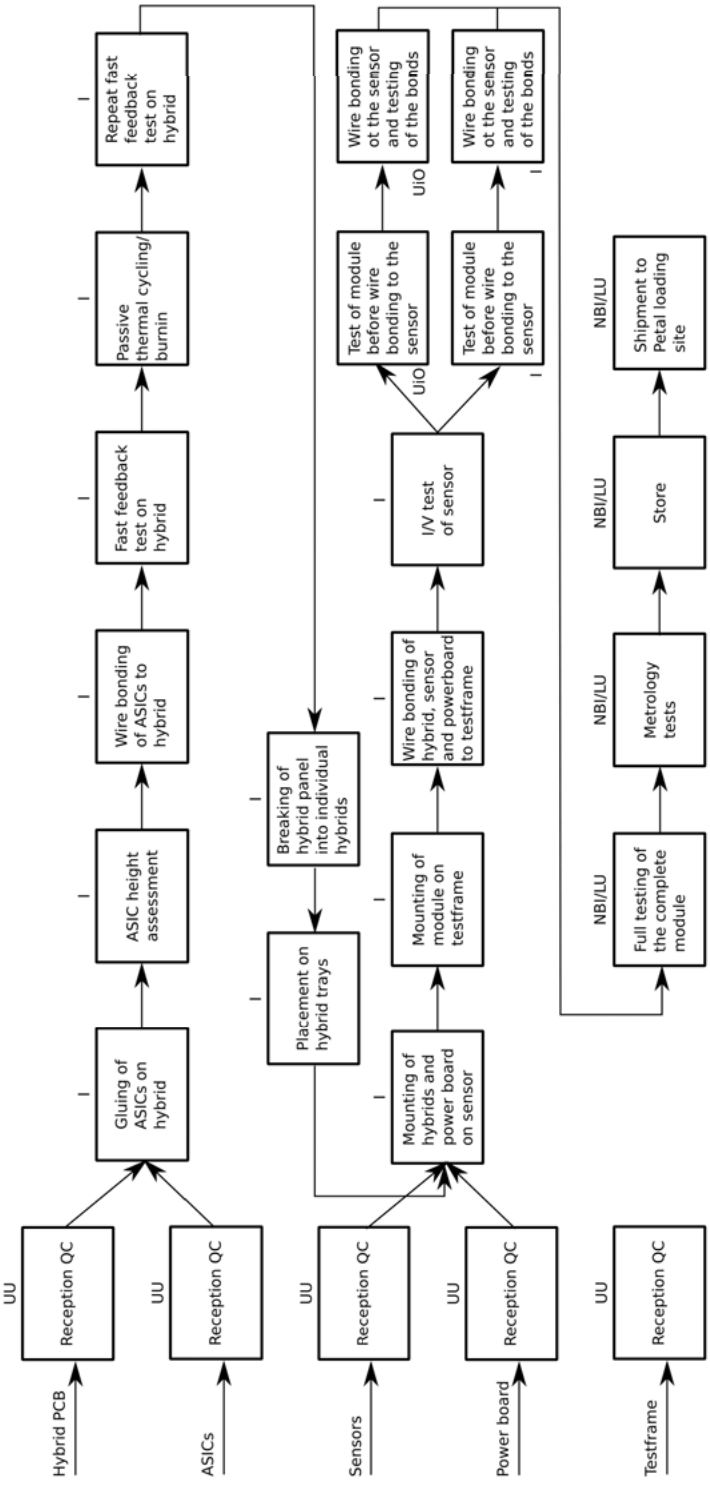

Figure 12.15. Module production workflow in the Scandinavian group of institutes.

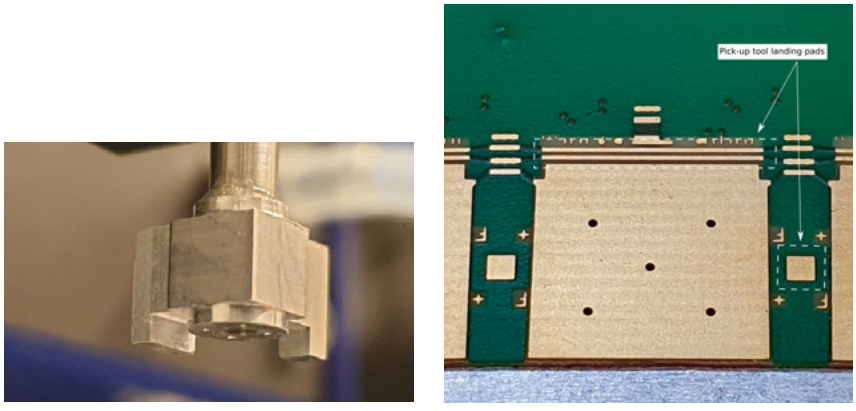

(a) (b)

Figure 12.16. Custom ASIC pick-up head for the industrial hybrid assembly workflow.

The hybrid assembly will be performed at NOTE with an automatic pick-and-place machine. UU has been working closely with the machine operators for the programming and tunning of the placement procedures, to ensure that all products are within specifications. One struggle had been the planarity of the ASIC placement on the hybrid when using the pick-and-place machine. The machine is typically using spring loaded pick-up heads that flex upon touch down, as they are purposed to place components without leaving any gaps between the substrate and the chip. This was addressed by the design and machining of a custom ASIC pick-up head (Fig. 12.16) that incorporates the desired z offset (120 μm) within the design. The pick-up tool is compatible with the automatic pick-and-place machine and has been designed to take advantage of the hybrid pads surrounding the ASIC placement for its touch down. The glue dispensing has been optimized in-house at the UU facilities, before the operations at NOTE (details can be found in Appendix B).

All the hybrid QC procedures are fully transferable to the industrial site and will be followed as described previously.

The module production will follow the nominal procedures, using a glue robot. The gluing setup (described in more detail in Appendix B) is consisted of a moving x-y table hosting a sensor-supporting-jig holder, a fixed (in x-y) mount for the syringe placement with μm precision in Z movements and an electric pneumatic valve that acts as the glue dispensing actuator. The timing of the gluing sequence is highly critical and will proceed as described below. The gluing procedure will start by first mixing the glue, transferring it into a syringe and mounting it to the setup structure. The sensor-supporting-jig will then be inserted in the setup and the relevant gluing sequence will be initiated. The gluing sequence patterns depend on the hybrid or powerboard types and are based on straight 8 mm lines (the motivation for the use of 8 mm lines is further discussed in Appendix B). During the sequence, the syringe

is held at a fixed Z offset from the top of the sensor and the table is moving for the dispensing of the patterns. Once the pattern lines have been dispensed, the sensor-supporting-jig is removed from the gluing setup and placed on the side. The hybrids/powerboard are then placed on top of the sensor surface using the tools, the weights are added and the structure is left to cure. The jigs used during the process are the same as for the nominal production. The glue robot setup can then be used for a different module production, allowing to optimize the use of glue and parallelize the workflow. Given the strict time limit imposed from the glue curing, only three modules are expected to be produced in the same session.

As mentioned earlier the calibration of the glue robot requires extended amount of testing because of the time-curing. The challenge has been addressed by using a fixed pressure for the dispensing and the construction of a look-up table for the delivered glue mass for a range of dispensing speeds at different times after mixing. An abridged version of the glue robot setup, the dispensing patterns and the robot calibration procedures are described in Appendix B, while a more detailed and thorough discussion on the employed methods is described in [122].

Once all the components are placed on to the sensor and the curing is completed the module is placed on a test-frame and an IV test is performed to ensure the sensor was not damaged (for example from glue leakage on bias/guard rings). After the completion of this test, the modules are either kept at NOTE ($R1$ modules) or shipped to UiO ($R3$ modules) for the bonding of the hybrids and powerboards to the sensor and testframe. In either case, once the bonding is completed and the bonds are tested, the modules are then shipped to LU ($R1$ modules) and NBI ($R3$ modules) for the final list of tests. The tests consist of visual inspection, electrical and thermal tests and metrology. The tests are described in detail in Appendix B. The modules are stored once tested and finally shipped in batches to IFIC for the Petal loading.

The Scandinavian group of institutes has successfully built a number of fully "electrical" (i.e. using a real, operational, sensor) and semi-electrical (i.e. using mechanical copies of the sensors with the same dimensions and markings) modules. The built module types were $R0$ and $R2$, and not $R1$ and $R3$ that will be built for the production, due to component availability and the needs of the collaboration at the time. Some examples of the produced modules are shown in Fig. 12.17.

Prototyping at UU

While the method presented above is the planned workflow during production, it should be noted that the prototyping phase required a more adaptable flow to fully develop and test all the procedures. All of the procedures needed for the full module production were first tested and optimized at UU using $R0$ module components. This served as a kick-starter for the activities, while preparing the workflow at NOTE and allowed to also foresee possible caveats.

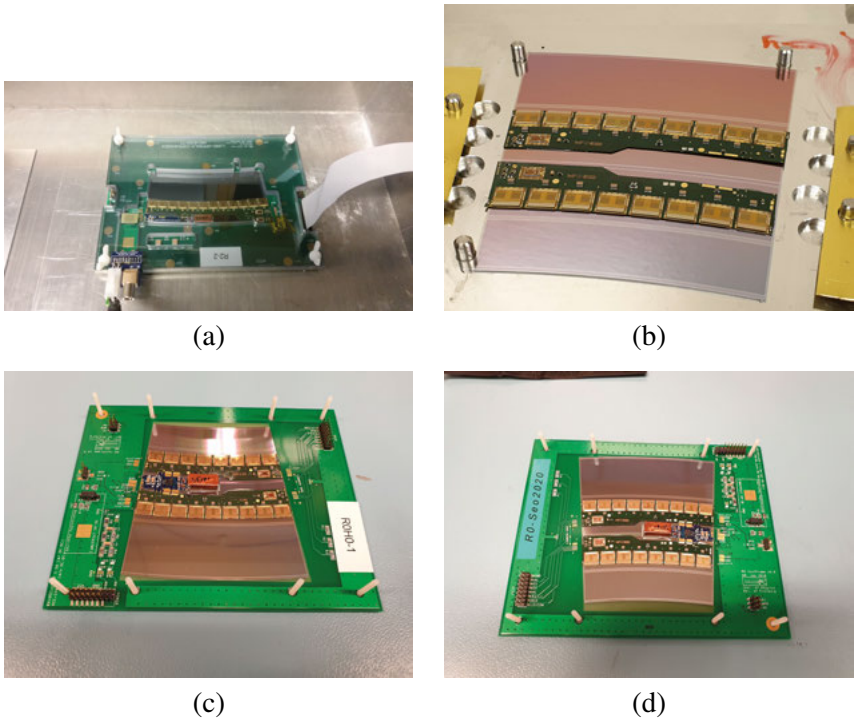

(a) (b)

(c) (d)

Figure 12.17. Examples of *R*2 (a) and *R*3 (b-d) modules produced by the Scandinavian group.

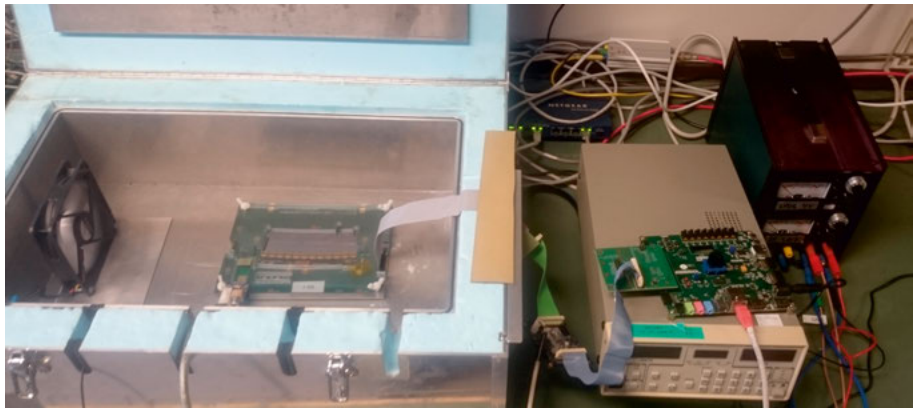

Figure 12.18. Photo of the electrical test setup used for the local UU QC procedures during prototyping.

UU has prepared an in-house hybrid assembly workflow, using a mini manual ASIC pick-and-place machine and the already mentioned custom ASIC pick-up head for the ASIC gluing and a local bonding machine. The full setup is presented in the Appendix B. All of the module gluing procedures and the robot optimization, which are also outlined in Appendix B, were also fully developed at UU.

An electrical test setup has also been prepared (Fig. 12.18), allowing quick testing of the produced hybrids and modules during prototyping. A selection of electrical tests from the first electrical module ($R2$) that was build at UU is presented in Fig. 12.19.

The progress has been affected from the Covid-19 restrictions across the world, which lead to delays in the finalizing of component and tooling designs among other things. The qualification of the UU activities on the incorporation of all production procedures within industry, and the overall Scandinavian group workflow, has been delayed as a result of this. The current workflow has been developed and optimized with the presently available components and will be tunned further in the future as new components will become available. Module production is only at its infant stage, with an exciting outlook into the long-awaited final production phase that will deliver the high-standard detector units for the ITk.

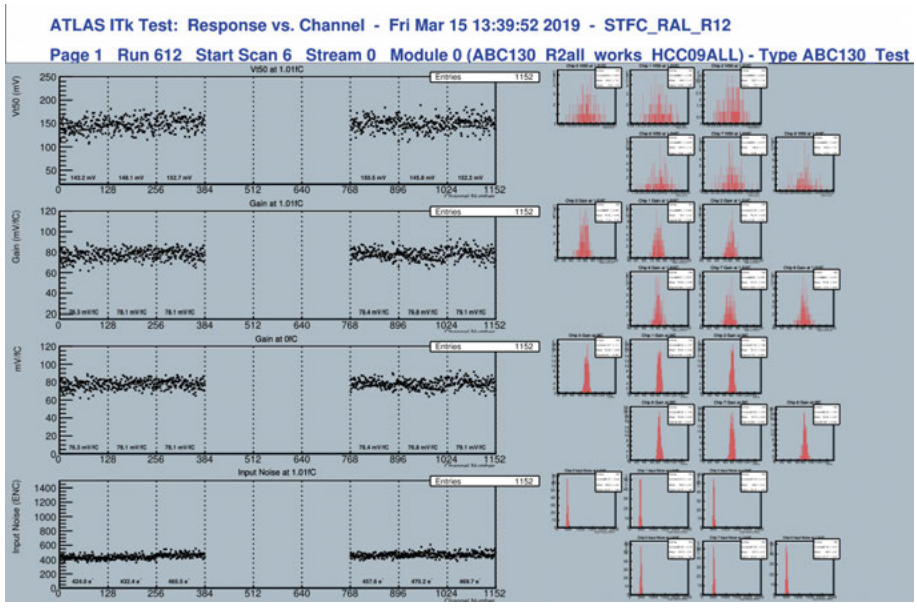

(a)

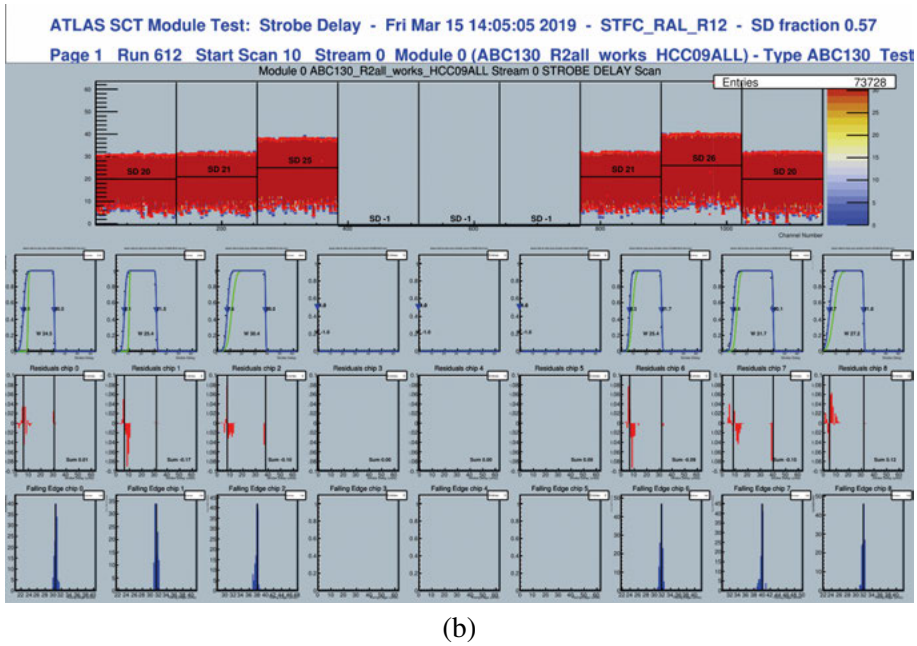

(b)

Figure 12.19. Selection of two of the electrical test results conducted on an *R*2 module. A series of response tests (Vt50, gain, mV/fC and input noise) per channel for one a portion of ASICs that populate the module is shown in (a). The results of a strobe delay test for the same channels are shown in (b). The tests are discussed in Appendix B.

Part V:
Neutron science and novel detector technologies

13. Neutron science

The unique properties of neutrons make them excellent probes for a wide range of studies on structural and magnetic properties of matter [123, 124]. Neutrons have neutral electric charge, which makes them non-destructive in their interactions and gives them high penetrating power. The have a wide energy range (Tab. 13.1) and their respective wavelengths can probe into different structures. For example, neutrons with energies in the range of atomic motions (meV) have wavelengths of the order of the inter-atomic distances and can probe structural information. Such studies can also provide complementary information to other experimental techniques such as X-ray scattering. Another important characteristic of neutrons is that, in contrast to X-rays, they do not have "linear" scattering cross section with heavier atoms (it is rather "quasi-random"). This allows them to "see" light elements such as hydrogen and deuterium even in the presence of heavier atoms and they are also sensitive to different isotopes of the same material. These attributes make them suitable probes for investigations on highly-sensitive light-element materials, such as soft matter materials or biological matter. Neutrons also have a magnetic moment and are therefore sensitive to magnetic fields in materials, making them suitable for example for the conduction of magnetic properties' studies.

The mentioned characteristics make neutron scattering experiments applicable to a wide range of research areas, such as high-energy physics, material-physics, geology and medicine. A variety of different techniques is used on research facilities like ILL, ESS or ISIS, to perform studies on the aforementioned areas. A short list of research techniques based on neutrons is given

Neutron energy	Energy range
$0.0 - 0.025\,\mathrm{eV}$	Cold neutrons
$0.025\,\mathrm{eV}$	Thermal neutrons
$0.025 - 0.4\,\mathrm{eV}$	Epithermal neutrons
$0.4 - 0.5\,\mathrm{eV}$	Cadmium neutrons
$0.5 - 1\,\mathrm{eV}$	EpiCadmium neutrons
$1 - 10\,\mathrm{eV}$	Slow neutrons
$10 - 300\,\mathrm{eV}$	Resonance neutrons
$300\,\mathrm{eV} - 1\,\mathrm{MeV}$	Intermediate neutrons
$1 - 20\,\mathrm{MeV}$	Fast neutrons
$> 20\,\mathrm{MeV}$	Ultrafast neutrons

Table 13.1. *Naming convention for neutron energy regimes.*

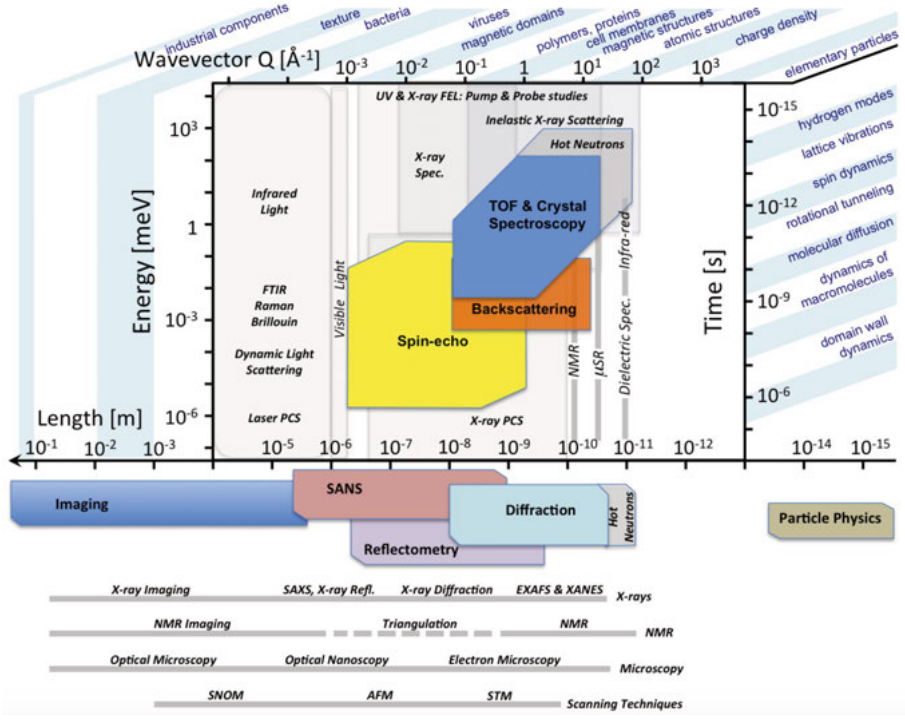

Figure 13.1. Illustration from the wide range of distance and time regimes than can be probed with neutrons at different energies. Figure from [125].

below, while an illustration of a more extensive list, spanning over a wide range of distance and time regimes, is shown in Fig. 13.1.

- Neutron diffraction
  Also known as elastic neutron scattering, the technique relies on the interaction of the neutrons with structures of crystalline materials.
- Small-angle neutron scattering (SANS)
  This technique is used to probe disordered materials (oppositely to crystalline materials) and aim to obtain information on their structure.
- Neutron spectroscopy
  Neutrons can also interact through inelastic scattering with materials. Measurements of a neutron's energy difference before and after its scattering from a sample allow the derivation of atomic and magnetic motions of atoms.
- Neutron reflectometry
  This technique relies on the reflective outcome of neutron interactions, as opposed to scattering, and is extensively used on studies of thin films.
- Imaging
  Imaging is the visual representation of an object. Imaging with neutrons implies that this is performed in a non-destructive way, and can be used complementarily to X-ray imaging. The technique relies on measurements of the beam attenuation caused by a homogeneous, uniformly-thick sample.

14. Neutron detectors

The harvesting of the results from neutron science experiments relies on neutron detection. Neutrons themselves do not carry any charge to produce a detectable electric signal and one has to rely on other methods for their detection. One option is to build upon their nuclear interactions with other materials to produce some detectable product. This is typically called a conversion layer.

Conversion layers are elements (Tab. 14.1) with high neutron capture cross sections and they can be used in gaseous or solid-state form for the conversion. The most commonly used element is ^3He because of its high capture cross section for thermal neutrons and its chemically inert character. The abundance of ^3He is however diminishing fast, causing not only an accessibility issue, but an increase in price as well.

^6Li is also a suitable candidate in terms of cross-section, but it requires special handling because of its chemical properties. The element interacts with water vapor and therefore a conductive coating layer needs to be added for protection.

B has a promising natural abundance (10^8 times that of ^3He) and can be used to take advantage of the ^{10}B high absorption cross-section. One approach is to use ^{10}B through boron trifluoride (BF3) enriched to 96% ^{10}B (natural boron is 20% ^{10}B, 80% ^{11}B). BF3 however is highly toxic and should be avoided. Another method is to use the solid-state $^{10}B_4C$ compound. It is an affordable and efficient material for the conversion and could serve as a good alternative to the gas-filled detectors such as ^3He or BF3.

The focus from here on will be on the solid-state ^{10}B conversion layer and the apparatus than can be used to detect the conversion products.

A typical experimental setup (Fig. 14.1) consists of a substrate (for example, aluminum) that is coated with a thin layer of ^{10}B. Incoming thermal neutrons are expected to interact with the layer, producing α and ^7Li particles. The particles can then be absorbed by a gas medium surrounding the coated substrate, producing an avalanche of ionizations that will be collected by a biased wire. The collection will lead to an electrical pulse, signaling the neutron capture.

The interaction can occur at different depths of the coating and thus the layer thickness needs to be tuned to achieve an optimal signal collection efficiency. If the layer is too thin, one reduces the conversion yield, while if it is too thick the products will be absorbed within the material. The ion range for α and ^7Li particles is roughly $3.2-3.9\,\mu$m and $1.5-1.7\,\mu$m respectively, therefore a layer of roughly $1\,\mu$m would preserve their propagation through the material regardless of the depth/angle of the interaction.

Element	Cross-Section (barn)	Reaction	Products
^3He	5333.(7.)	$^3He(n,p)^3He$	p, $E_p = 0.57\,\text{MeV}$ ^3He, $E_{He} = 0.19\,\text{MeV}$ $0.77\,\text{MeV}$
^6Li	940.(4.)	$^6Li(n,\alpha)^3He$	α, $E_\alpha = 2.05\,\text{MeV}$ ^3He, $E_{He} = 2.74\,\text{MeV}$ $4.79\,\text{MeV}$
^{10}B	3835.(9.)	(94%) $^{10}B(n,\alpha)^7Li*$	α, $E_\alpha = 1.47\,\text{MeV}$ ^7Li, $E_{Li} = 0.83\,\text{MeV}$ γ, $E_\gamma = 0.48\,\text{MeV}$ $2.3\,\text{MeV}$
		(6%) $^{10}B(n,\alpha)^7Li$	α, $E_\alpha = 1.77\,\text{MeV}$ ^7Li, $E_{Li} = 1.01\,\text{MeV}$ $2.79\,\text{MeV}$

Table 14.1. *List of most commonly used elements as a thermal neutron conversion layer. The second column lists the absorption cross section for* $2200\,\text{m/s}$ *travelling neutrons (i.e. thermal neutrons). The values have been taken from [126].*

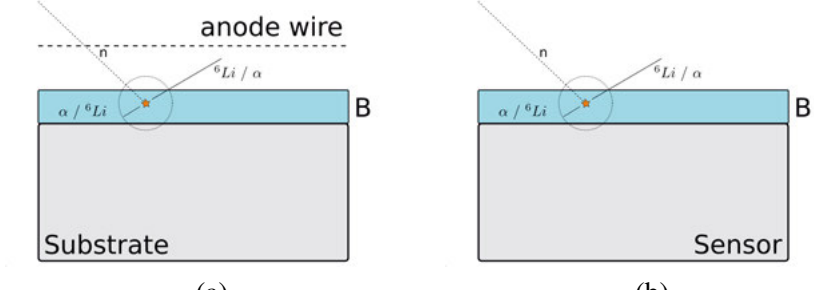

(a) (b)

Figure 14.1. Illustrations of a typical (a) and the investigated (b) experimental apparatus for collection of the neutron capture products in ^{10}B.

In this thesis a different experimental apparatus is explored, where the substrate could potentially act as the detection medium (Fig. 14.1). The study scope, status and goals are presented in the next chapter.

15. Studies for a novel neutron detector

The typical detecting apparatus for neutron capture in ^{10}B attempts to capture the products (α, ^{6}Li) with a gaseous detector surrounding the converting structure, as it was briefly outlined in the previous chapter. A new approach is being explored, where the detection of the neutron capture products will be attempted from the coating substrate. The idea of using of semiconductor for this purpose has been previously discarded because of their thick dead layers, which would seriously degrade the signal efficiency, given that the α and ^{6}Li would lose most of their energy before reaching the active area of the detector. This study aims to evaluate the suitability of the HV-MAPS detectors as candidates for this detecting apparatus. HV-MAPS (Sec. 5.2) detectors have very thin structure and a monolithic design, which could potentially allow a competitive signal efficiency, in a simpler overall setup.

The study will approach this objective in two phases; Phase-I and Phase-II. Phase-I (Sec. 15.1) will serve as an exploratory study and will be based on a preliminary setup, while Phase-II (Sec. 15.2) will be performed with the final setup, investigating its full potential.

15.1 Phase-I

Given the unfamiliarity with the coating procedure, it was decided that a preliminary sensor would be used for Phase-I. The focus was on:

- qualifying the coating procedure and
- evaluating the sensitivity of the coating for neutron capture and subsequent α detection.

15.1.1 Setup

The setup is consisted of:

- a mini strip n-on-p sensor,
- a readout-out board and
- a data acquisition system.

The sensor (Fig. 15.1) comes from the same family of sensor that are used for strip end-cap ITk sensors (mentioned in the previous part and described in Ch. 12). The sensor strips pads were stitch-bonded into one single read-out channel to optimize signal collection, with the trade-off of position resolution, which is not the primary objective in this phase.

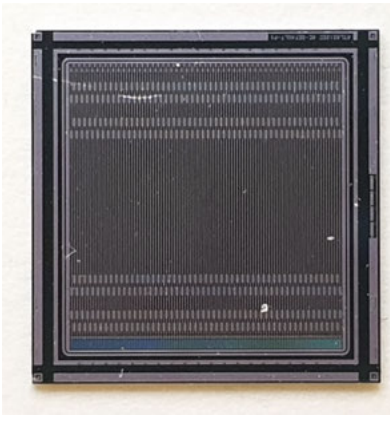

Figure 15.1. Picture of the mini n-on-p strip sensor.

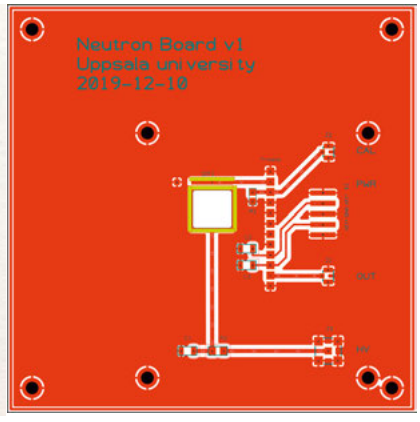

Figure 15.2. Phase-I read-out board. The board was designed by N. Bingefors.

The readout-out board (Fig. 15.2) was designed to provide the high-voltage (HV) biasing of the sensor with a low-pass filter to cut-away frequencies that could infiltrate to the signal's region of interest, the grounding and bias pads for the operation of the sensor, a preamplifier input and its respective powering scheme and the extraction of the pre-amplified output. The board also supports a calibration input, which allows the injection of pulses for the characterization of the pre-amplifier response. The board was printed in a single FR-4 layer and a container was designed to host the assembled board to reduce the susceptibility of the setup to the pick-up of surrounding noise. The container also provides a dark environment during the measurements, removing any ambient photon-income from the room.

The board was designed to also serve as the sensor holder during the coating procedure. During prototyping, two types of coating approaches were investigated; one from the top side of the sensor and one from the bottom. The top side has a thinner material budget (SiO_2 and aluminum) in between the coating layers and the active region, while the bottom side is easier to coat, given the lack of other components on the board and bonds. This lead to the decision to leave a cut-out on the readout-out board, under the sensor, in order to explore the coating from either side.

In both cases the sensor was attached with a two-part epoxy glue[1] on to the board. The glue was deposited on the rim close to the HV-pad, except from one corner where a small portion of conductive glue was used to conduct the bias to the sensor. The backside of the sensor was then mounted on top of the glue. In the case of the top-coated sensor, the bonds from the strips to the read-out and guard ring to the ground pad were made before the coating. A

[1] Araldite: 100g/80g.

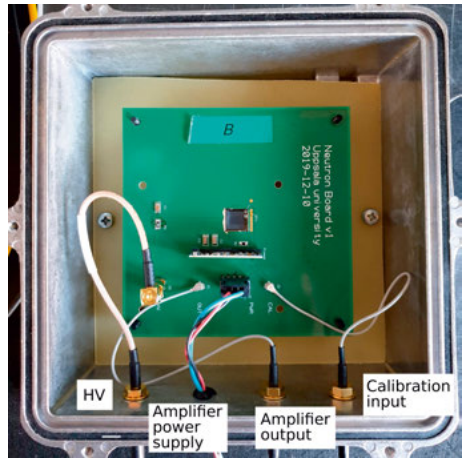

Figure 15.3. Picture of the Phase-I experimental setup.

small portion of glue was added on top of each connection to ensure that they would not become detached during the coating.

The coating of the sensors was carried out at the ESS coating facilities in Linkoping. The collaboration was very valuable for the experiment and gave useful input into the procedures. The discussions concluded in the request to apply a 1.0 μm thick layer of $^{10}B_4C$ at low temperature (maximum of 60 C), due to limitations from the components' side. For the case of the top-coated sensor, no component other than the sensor was mounted and all the pads were covered with kapton tape. During the coating, aluminum foil was added to cover all areas except the desired opening of the sensor. The bottom-coated sensor board was already assembled and a 3D-printed (PLA) case was used to cover all sensitive parts. The deposition was completed without any problem noted (for example, no adhesion problems, or detached bonds).

The further tests were continued with the top-coated sensor and all subsequent comments and discussion will refer to that one. A picture of the final setup, once all components were added, can be seen in Fig. 15.3.

15.1.2 Measurements

The final setup was tested for neutron capture detection sensitivity. The first step to that end was to evaluate the sensitivity of the setup to α particles close to the expected energy regime coming from the capture process in boron.

In the case of a neutron capture in boron the expected α particles energies are: 1.47 MeV (94%) and 1.77 MeV (6%). Assuming α particles from the most common decay, the original 1.47 MeV energy will decrease before reaching the active layer of the sensor, depending on the place the process took place and the trajectory of the particle thereafter. Simulation studies in FLUKA pro-

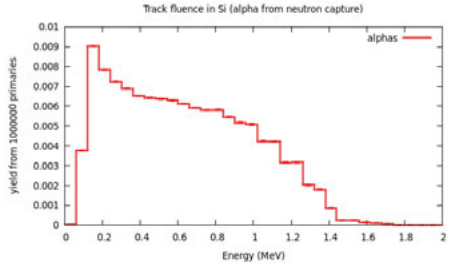

Figure 15.4. Simulation results of the expected α energy distribution that would be reaching the sensor layer of the setup.

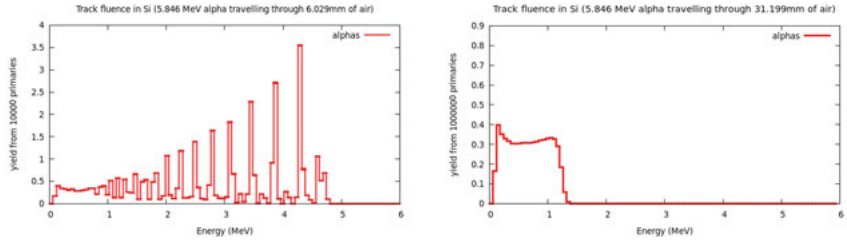

(a) (b)

Figure 15.5. Simulation studies on the attenuation profile of the 5.486 MeV α particles emitted during the ^{241}Am decay at a $\sim$ 6 mm (a) and $\sim$ 31 mm (b) distance from the coated sensor surface.

vided an estimate on the energy distributions that would be recorded with the setup. The results, illustrated in Fig. 15.4, provided the expected range of energies.

Based on these estimations, an ^{241}Am source was used to emulate αs close to that range. ^{241}Am is known to decay primarily (86%) by emission of an α with $E_\alpha = 5.486\,\text{MeV}$. Simulation studies (Fig. 15.5) provided the expected attenuation profile when the source was placed at a different distances from the sensor surface. Taking into account the attenuation in air, it was determined that a distance of $\sim 30\,\text{mm}$ would bring the α particles down to the energy spectrum expected from the neutron capture. An additional measurement was taken at a closer distance ($\sim 6\,\text{mm}$) to allow a calibration of the pulse collection software (MAESTRO).

The measurements served as a preliminary check of the viability of the study and allowed the calibration of the read-out system. Next, a similar measurement was conducted with a strong ^{252}Cf source[2]. The source was hosted in a safe, remote location and all measurements were carried out with necessary precautions. The container hosting the setup was placed on top of the source, receiving a dose of $64.7\,\mu\text{SV/h}$ and the monitoring was handled from

[2]Recorded dose of $90\,\mu\text{Sv/h}$ (on top of the source).

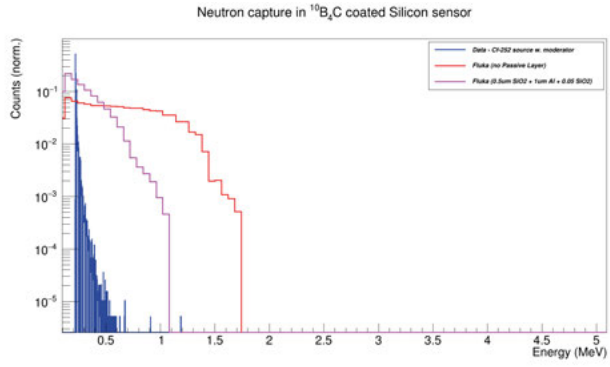

Figure 15.6. Comparative plot showing the data collected with the ^{252}Cf source (blue) and the expected results from simulations when no (red) and 1 μm-thick (purple) passivation layer was assumed. The distributions have been normalized.

a few meters away during the preparations. The measurements were collected for 2.5 hrs and the data were compared with theoretical simulations (Fig. 15.6).

The simulation was carried out assuming a thermal neutron beam entering the boron layer and collecting the distributions of the α particles in silicon. One big unknown in this study is the thickness of the dead layer on top of the detector. It is known that the dead layer is created from the SiO_2 layer and the aluminum on the strip pads, but only a rough estimate of its thickness can be made, due to disclosure agreements with the manufacturer. An approximation of 1 μm was considered to be a good choice, allowing to account for additional inefficiencies, such as the p-stop implants' layer. The results agree to a satisfactory extent for the purpose of this study and mark the Phase-I as completed.

15.2 Phase-II

Phase-II aims to explore the sensitivity of a HV-MAPS detector to neutron detection using the same principles. The sensor under consideration is the MuPix detector, which was developed for the Mu3e experiment.

This section will cover the envisioned workflow for Phase-II, as Covid-19 had an impact on the progression of this project.

The results of Phase-I were considered encouraging to attempt a similar study with the MuPix detector, covering the following steps:
Step-1: Evaluation of the MuPix sensitivity to α and γ particle energies close to those expected from the B(n,α)Li* neutron capture reaction and their respective spatial footprints.
Step-2: Coating of a MuPix detector with 1.0 μm thick layer of $^{10}B_4C$ at the Linkoping facilities.

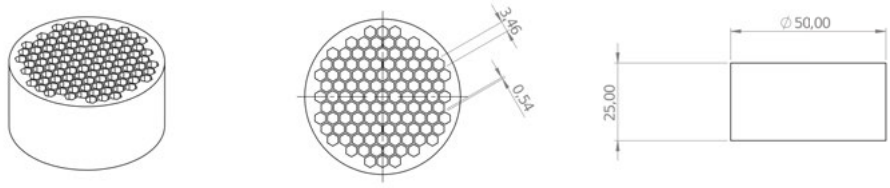

Figure 15.7. Schematics of the designed collimator. All units appear on mm.

Step-3: Evaluate the sensitivity of the coated MuPix detector with a ^{252}Cf source or neutron beam in Uppsala.

Step-1 has been progressing via remote communication with the Heidelberg University group, due to the present travel and lab accessibility restrictions. In this step the objective is to assess the efficiency of the MuPix detector in collecting the alpha signal produced during the B(n,α)Li* reaction and rejecting the γ induced signal from the same process. As already mentioned, the αs from the process are primarily expected to be produced with $E_\alpha = 1.47\,\text{MeV}$. Depending on where the reaction takes place and the angle that the alpha will be travelling in, the alphas could reach the detector with energies down to $\sim 200\,\text{keV}$. Naturally the goal is to collect as much of the produced alpha energy range as possible and it is thus important to also evaluate the cut-off α energy the MuPix detector can record.

A good approximation for these kinds of measurements can be performed using, similarly to Phase-I, an ^{241}Am source ($E_\alpha = 5.49\,\text{MeV}$) at different distances to emulate the expected α energy profile reaching the detector from neutron capture. A collimator was designed (Fig. 15.7) for the measurements to remove potential tails from the distribution, originating from non-orthogonal interaction angles.

The evaluation of the sensitivity to the γ products ($E_\gamma = 0.48\,\text{MeV}$) is important as it could interfere with the α measurements' position resolution. The position resolution, which was not of primary concern during Phase-I, will be a high desired quality for future neutron detection measurements. The γs will interact primarily via Compton Scattering in that energy regime and will therefore travel further into the detector, depositing their energy to more distant pixel segments. Studies with a ^{137}Cs, which produces photons with $E_\gamma = 0.66\,\text{MeV}$[3], are expected to allow a characterization of this interaction. Once the detector response is characterized, a gamma-rejection strategy can be designed.

Step-2 is expected to be performed, at least at the first iteration, based on the useful insights gained during the coating procedure of Phase-I. The experience

[3]The $E_\gamma = 0.66\,\text{MeV}$ photons produced from ^{137}Cs interact primarily through Compton Scattering in Si, with similar cross-sections to that of the $E_\gamma = 0.48\,\text{MeV}$ photons produced via neutron capture in ^{10}B.

will allow quicker development of the support structures, while similar coating settings are expected to be sufficient.

This collaboration suffered delays because of the Covid-19 measures. Regardless, the results collected so far appear to be very promising, with an exciting outlook for future development.

Summary and conclusions

The presented work is centred around experimental High Energy Physics (HEP), in the context of exotic particle searches, data analysis techniques and the development and production of suitable detectors. The main covered topics span the aforementioned areas and are primarily related to the ATLAS experiment at the Large Hadron Collider (LHC). A brief summary of the projects discussed in this thesis is given below.

Quark- or gluon-initiated jets are the main source of background for hadronically decaying τ leptons. The estimation of its impact on ATLAS searches is presently carried out separately from each individual analysis, using techniques such as the data-driven Fake Factor (FF) method. ATLAS has mandated a task force, Fake Tau Task Force (FTTF), to develop a universal method of determining this source of fake τs and their associated systematic uncertainties through a dedicated tool (Tau Fake Factor Tool, or TFFT). The tool will be employable by analyses to derive the FFs that apply to their specific signal regions (SR). The unified approach relies on the FF method and the exploitation of its dependence on the quark/gluon fraction that characterizes a region of specific jet composition. In the discussed approach the jet composition is described with respect to the τ candidates' p_T and number of associated tracks, which are split with respect to their jet origin in four types; b-quark jets, non-b-quark jets (i.e. u-/d-/s-/c- quarks), gluons and un-matched objects. The FF of jets from different quark/gluon-fraction composition regions is expected to have different distributions with respect to a discriminating parameter that is sensitive to the jets origin, which in the FTTF case is the jet-width. The calculations of the FFs are performed in data, using two Control Regions (CR) that are dominated by gluon-originating (multi-jet) or quark-originating ($Z+$jets) jets. Their respective quark/gluon-fractions are estimated through a Monte Carlo (MC) template fit. The TFFT is being developed to rely on inputs from the tool users and the developers. The user-provided inputs are in the form of jet-width and p_T distributions in regions defined as the SR but with an inverted requirement on the τ candidate identification criterion (anti-τ SR). The developer-provided inputs are information from the two data interpolation regions and the MC templates. The tool makes use of the inputs to perform a maximum likelihood fit on the user-provided anti-τ SR and provide a binned FF, in terms of the τ candidates' p_T and the number of associated tracks, along with its uncertainties.

Charged Higgs bosons are particles predicted by several Beyond the Standard Model (SM) theories, but not the SM, and their discovery would provide

an undisputable sign of new physics. A charged Higgs boson search is presented, that investigates the $H^{\pm} \to \tau\nu$ decay channel over a $90 - 2000\,\text{GeV}$ mass range using a $36.1\,\text{fb}^{-1}$ dataset of pp collisions collected at $\sqrt{s} = 13\,\text{TeV}$ with the ATLAS detector. The study was interpreted within the hMSSM theory which predicts $\tau\nu$ to be a sensitive channel over a large range of $H^{\pm}$ masses, especially for large $\tan(\beta)$ values, where it is dominant at low masses and subleading at high masses. The $H^{\pm}$ is expected to be produced in a topology that includes a top quark, resulting in final states that would be recorded as a τ and missing transverse energy (from the ν_{τ}), because of the $H^{\pm}$ decay, and a lepton (e or μ) and missing transverse energy (from the ν_{ℓ}) or jets signature, depending on the $W^{\pm}$ decay associated with the top quark. In this thesis, only the latter is discussed and is abbreviated as "tau plus jets". The employed analysis strategy relied on the use of a missing transverse energy trigger and the optimization of its signal sensitivity. The dominant sources of background that would potentially interfere with the study are processes that result is τ detector signatures similar to that of the signal. They were treated collectively depending on the object causing the signature, and the modelling was validated in dedicated CRs. The discrimination between signal and background was carried out using boosted decision trees. The final results were compatible with the SM-only hypothesis, yet allowed the successful setting of new upper limits on the charged Higgs boson signal strength over the investigated mass range. The study also concluded in an exclusion of all $\tan(\beta)$ values for $m_{H^{\pm}} \leq 160\,\text{GeV}$, while for $\tan(\beta) = 60$ all $m_{H^{\pm}} < 1100\,\text{GeV}$ masses are excluded, in the context of the hMSSM scenario. Lastly, the study allowed the derivation of combined results along with the ATLAS $H^{\pm} \to tb$ analysis which resulted in 95% CL exclusion limits on $\tan(\beta)$ for the hMSSM as a function of $m_{H^{\pm}}$, serving as a summary of the combined ATLAS sensitivity to $H^{\pm}$ through the two decay modes.

The physics potential of the LHC has been demonstrated with a vast number of publications, yet the present needs suggest the need for an upgrade. The LHC is presently undergoing an upgrade that will deliver higher peak luminosity values of $5 \times 10^{34}\,\text{cm}^2\text{s}^{-1}$, allowing an integrated luminosity of $250\,\text{fb}^{-1}$ per year and aiming for a total $3000\,\text{fb}^{-1}$ over the following twelve years of operation. The upgrade will result in more demanding conditions for the LHC experiments, in terms of higher particle fluxes (stressing the current detector in terms of occupancy and radiation damage) and larger collected data volumes, requiring operation at higher trigger rates. ATLAS is currently upgrading several of its systems, one of which is the inner detector, which will be replaced by the new all-silicon detector sub-system (called the Inner Tracker, or ITk). The ITk is designed to operate under the demanding conditions of the upgrade and will consist of pixel and strip detectors. The focus on this thesis was the strip detectors, and more specifically, those that will be placed in the detector end-cap section. Their global and local structures were briefly introduced, and a more detailed description of their basic units, the modules, was pro-

vided. The thesis focused on the workflow surrounding module production and the associated Quality Assurance (QA) and Quality Control (QC) procedures, in both university lab facilities and in industry. The activities within the Scandinavian group of institutes (consisting of Uppsala University , Lund University, the Niels Bohr Institute and University of Oslo) were described further because of their relevance to the work conducted by the author. The flow is relying on an industrial partner, NOTE, with Uppsala University being the main contact for the incorporation and possible adaptations of the QA/QC procedures during module production. A descriptive list of the employed procedures for the module assembly and its delegation among the Scandinavian groups is provided. The workflow is optimized with the presently available components and will be tunned further in the future as new components will become available.

Lastly, a non-ATLAS project was also covered in this thesis, which concerns the development of boron-coated semiconductors as suitable devices for neutron detection. A common method for neutron detection is the employment of a converter (solid or gas) that will produce a recordable (electrical) signal when it interacts with neutrons. The motivation for the presented project stems from the need to explore new detector technologies for neutron detection on account of the diminishing resources of the commonly used ^3He gas as a conversion medium. A suitable alternative converter is ^{10}B, which produces α particles as a result of the neutron capture. Opposingly to other approaches, the project aims to investigate the sensitivity of a semiconductor to collect the produced αs through the ^{10}B layer. The investigations were carried out in two phases; Phase-I, that offered familiarity with the procedures and provided a solid ground for proof-of-concept, and Phase-II, that will be performed with a more suited detector for position and timing resolution. Phase-I was conducted using a mini strip n-on-p sensor that was coated with a $1\,\mu$m thick $^{10}B_4C$ layer. An ^{241}Am source allowed the tuning of the setup for neutron capture and a ^{252}Cf source was used to investigate the conversion and signal collection efficiency. The results were encouraging to move on to Phase-II. Phase-II will use a MuPix detector for the setup, which is developed by Heidelberg University. The impact of Covid-19 resulted in a slower progression than expected, prohibiting the completion of the study at the time of writing. The planned workflow is described in the text.

* * *

Scientific research starts with questions. Questions become theories and, eventually, one hopes to find answers through experiments. While this may be common knowledge, it is important to reflect and acknowledge the intercorrelations it requires.

It has been both challenging and rewarding to have had the opportunity to work on so many different parts of experimental HEP physics. It is humbling

to see in practice how many steps and functions a meaningful discovery requires.

The summary of the described projects gives only a glimpse of their true value. A lot of exciting work is being carried out, only feeding the curiosity for what is to come next.

Sammanfattning på svenska

När man är nyfiken så ställer man frågor. Partikelfysik är vetenskapen att ställa frågorna om “vad?”, “Hur?” och “under vilka omständigheter?”, på ett konsekvent och upprepningsbart sätt, i syfte att lära sig om naturens grundläggande byggstenar, nämligen elementarpartiklarna och deras växelverkan vilka sker genom utbyte av kraftpartiklar. Svaren som vi har är samlade i teorier som Standardmodellen för partikelfysik (SM) och den allmänna relativitetsteorin. Dessa beskriver naturen rätt väl men vi vet också att det finns ett antal brister som t.ex. asymmetrin mellan materia och antimateria i naturen som visar att vår fysikaliska modell inte är fullständig. Därför utvecklas nya teorier för att försöka ta itu med de öppna frågorna. Sådana teorier förkortas allmän "Bortom SM-teorier", eller kort BSM.

Universums minsta byggstenar, elementarpartiklarna, som upptäckts och beskrivs av SM kategoriseras genom deras fysikaliska egenskaper. Materiepartiklar kategoriseras som fermioner, och kraftbärande partiklar som bosoner. Fermionerna är i sin tur uppdelade i leptoner (där ingår t.ex. partiklar som elektronen, e och tau, τ) och kvarkar (t.ex. b- eller u-kvarkar). Kvarkar är intressanta i den meningen att de inte kan existera på egen hand utan måste vara i formationer, hadroner. Två exempel på sådana hadroner är protonen och neutronen vilka består av tre kvarkar var. En för de flesta välkänd typ av boson är fotonen som bär den elektromagnetiska kraften. Andra bosoner heter gluon, Z, W och den nyligen upptäckta Higgs-partikeln.

Den världsledande anläggningen för forskning inom partikelfysik, Large Hadron Collider (LHC), vid CERN är värd för stora experiment i syfte att studera de ovannämnda partiklarna och hur de växelverkar. Denna avhandling handlar om forskning gjord vid ATLAS-experimentet. I LHC skapas nya elementarpartiklar genom att kollidera protoner vid mycket höga energier. I ATLAS-experimentet registreras signaler från de nyskapade partiklarna. I ATLAS-experimentet finns många olika detektorstrukturer som utnyttjar de olika partiklarnas interaktionsmetoder med material för att samla in så mycket information om partiklarna. Data som samlats in analyseras och ny fysik undersöks utgående från den redan etablerade partikelfysikkunskapen. En stor utmaning i dessa studier är felidentifiering av partikelsignaturer i detektorerna. Därför behövs dedikerade tekniker för att åtgärda detta. Ett fall som undersöks i denna avhandling är felidentifiering av kvarkar och gluoner som τ-leptoner i data. Kvarkar och gluoner kan nämligen skapa liknande signaturer i detektorn som τ-leptoner vilket ger upphov till felidentifering som kan ha stor betydelse för tolkningen av fysikresultatet. Den metod som utvecklats i denna avhandling bygger på att studera egenskaperna hos dessa felidentifieringar genom

datasimulering och utgående från dessa skapa en generell metod som kan användas i olika analyser av data från LHC.

I avhandlingen presenteras även en BSM-studie där man letar efter ytterligare Higgs-bosoner som till skillnad från den som ingår i SM är elektriskt laddade. Dessa antas tillhöra en utökad familj av partiklar som inkluderar den redan upptäckta neutrala Higgs-bosonen. Sådana bosoner förutses inte inom SM vilket gör dessa studier mycket intressanta eftersom en potentiell upptäckt skulle vara ett tydligt tecken på ny fysik bortom SM. När man letar efter nya partiklar måste de förlita sig på förutsägelser som ger vägledning för deras egenskaper. Detta möjliggör utveckling av skräddarsydda sökningar som skulle optimera chansen för en upptäckt. Studien som presenteras i denna avhandling ledde inte till en upptäckt, men det minskade utrymmet för vilka egenskaper partikeln tillåts ha för att existera i naturen.

Bristen på upptäckt av BSM är en av motivationerna för att uppgradera den experimentella utrustningen på CERN för att höja känsligheten för att finna ny fysik som krävs för att få en mer korrekt beskrivning av universum. Detta skall uppnås genom att höja intensiteten i LHC med en storleksordning för att öka chansen för exotiska fenomen. ATLAS-detektorn, liksom alla andra experiment runt LHC, måste anpassas för att matcha den nya kraftfullare acceleratorn och behoven av som ställs för datainsamling och analys. Den kanske viktigaste uppgraderingen är den som görs för detektorns inre del. Det nya instrumentet för att registrera partikelbanor med hög spatiell upplösning kommer helt och hållet att vara baserat på kiseldetektorer som antingen är segmenterade i 1-dimension (strip) eller 2-dimensioner (pixel). Den minsta enheten vid konstruktionen av detta instrument kallas modul och fokus i denna avhandling är utveckling av stripdetektormoduler som kommer att placeras i den inre detektorns yttre delar. Arbetsflödet för produktionen av dessa måste följa strikt kvalitetssäkring (QA) och kvalitetskontroll (QC) för att säkerställa att alla enheter kommer att fungera som förväntat i flera år efter installationen. Produktionen delas mellan många ATLAS-grupper utspridda över jordklotet. Fyra skandinaviska grupper från Uppsala, Lund, Köpenhamn och Oslo har gått samman i ett produktionskluster. Arbetet som utförs vid Uppsala universitet beskrivs i denna avhandling och är sammanflätat alla klustrets aktiviteter. Arbetsflödet för produktionen inklusive QA/QC-procedurer som utförs i samarbete med svensk elektronikindustri har anpassats i enlighet med detta. Projektet närmar sig slutet av förberedelser inför produktion. Modulerna som slutligen produceras kommer att installeras i ATLAS-detektorn från och med år 2025.

Ett annat område där instrumentering ursprungligen utvecklad för forskning inom partikelfysik kan tillämpas är för mätningar inom neutronvetenskaper. Neutroner kan användas för många olika experimentella mätningar såsom studier av olika funktionella materials fysikaliska egenskaper. Neutronvetenskaperna genomgår en kraftfull utveckling i landet och detta motiverar behovet av att utveckla neutrondetektorteknologier som matchar behoven och nya till-

gängliga resurser. Neutroner är neutrala partiklar och för deras detektion krävs att ett medium används som kan producera laddade partiklar från neutroninteraktioner. Det tidigare mest använda mediet för detta är ^3He. Världstillgången på ^3He minskar snabbt och därför utvecklas och undersöks andra alternativ. I denna avhandling undersöks lämpligheten av nya borbelagda halvledardetektorer för neutrondetektering. Bor producerar en α -partikel (sammansatta partiklar som består av två protoner och två neutroner) när en neutron interagerar med materialet. Den undersökta halvledarstrukturen registrerar de α-partiklar som skapas i borskiktet.

Studierna som presenteras i denna avhandling sträcker sig över olika områden inom partikelfysik, från dataanalys till detektorutveckling. Dessa ger bara en glimt av det spännande arbetet som bedrivs inom området för partikelfysik, men ändå kan de förhoppningsvis tjäna som en indikation på hur cykeln för vetenskaplig forskning bedrivs där utmaningar inom fundamental fysik kräver teknologiutveckling för att besvaras och teknologin som utvecklats i sin tur kan utnyttjas inom andra områden.

Acknowledgements

This is by far my favourite part, and I am truly excited to be writing it!

First and foremost, I wish to thank my supervisor, Richard Brenner, for giving me the opportunity to be part of the Uppsala University ATLAS group. Thank you for all your guidance, patience and support along the years. I feel lucky to have had the chance to work close to you. I also wish to thank my co-supervisors Arnaud Ferrari and Elin Bergeås Kuutmann. Arnaud, thank you for all your attention to detail (and for being the human Grammarly) and for all the last-minute proof-reads. Elin, you have been the person to turn to for all minor or major things over the years. Thank you for always having a kind word to offer and being so supportive and helpful!

I am truly grateful to all the people that I worked with over the past years. I want to thank Daniele Zanzi, Quentin Buat, Bertrand Martin Dit Latour, Michael Pitt, Pawel Jan Klimek, Vojtech Pleskot and Antonio De Maria for all your guidance and pedagogical inputs. You made the transitions into the various projects so much easier. I also feel extremely lucky to have been a part of the Scandinavian cluster and to meet and work with so many wonderful people. I would especially like to thank Geoffrey Mullier, Ole Rohne and Ole Dorholt. Geoffrey your help all those years has been immense. Thank you for answering all of my questions and bringing a different, colourful, note to even the most mundane things. Ole and Ole thank you for taking the time to show me around and hosting me at your lab. It has been a lot of fun, and I really enjoyed it. The support network from Uppsala University has been invaluable! A big thank you to Nils Bingefors, Lars-Erik Lindquist, Niklas Johansson, Fredrik Bohlin, Dan Bergman, Johan Eriksson, Lars Hermansson, Hans Calén, Johan Nyberg, Petter Ström and Daniel Primetzhofer. Nils, thank you for always being there and for helping out with all the crisis situations in the lab. Lars-Erik, I honestly cannot count the times I reached out in near panic for last-minute alterations. Thank you! Words do not cover how relieved I was every time. Fredrik, thank you for putting up with me during all those tool iterations! Johan, thank you for training me into the arts of 3D printing and for always keeping an eye on the attempts. Hans and Jonan, thank you for introducing me to the magical land of radioactive sources and for all the pedagogical inputs around them. Petter, I don't think many people can make a full day at work so fun and relaxed the way you do. Thank you for all the help! I would also like to thank Chung-Chuan Lai and Linda Robinson for all their help in the boron coating procedures. Last, but definitely not least, I would like to thank Johnny Goncalves. Johnny, I have really enjoyed all these long

days in the clean-room, even the second half of them when hell would break loose. Thank you for all the chats and all the help throughout these years.

To the members of the Uppsala ATLAS group, Richard, Arnaud, Elin, Mattias Ellert, Rebeca Gonzalez Suarez, Nils, Venu Ellajosyula, Thomas Mathisen, Christina Dimitriadi, Olga Sunneborn Gudnadottir, Jonas Steentoft, Max Isacson, Mikael Mårtensson, Petar Bokan and Joakim Gradin, a big smile comes to my face when I think of you. I am really going to cherish our lunch brakes. Richard, thank you for all the life-lessons and once-in-a-million stories and Mattias, thank you for sharing an amazing number of insane facts to all discussions. Rebeca, whenever I see toothpaste, I will think of you. Thank you for showing me many windows, at a time where I did not feel I could look for any. I cannot express how grateful I am. Venu, I want to make jokes, but I will instead say once again how happy I am that you joined the group. I feel extremely lucky to have had the chance to work near you. Thank you for all the chats and for listening when I needed to vent. Thomas, thank you for bringing out the goofiest of my sides! Christina, thank you for checking up on me during the dark, isolated months of the writing and Olga, thank you for all the fun hang outs, the "shared" science fair session and the workout photoshoot. Jonas, thank you for all your wonderful energy! It was life-saving during those long module building sessions. And for baking excellent cookies in times of need. Max, thank you for all the grid magic and for being the official ambassador to Swedish culture throughout the years! I think most of my fun times in Uppsala are thanks to you and Pamela. Mikael, thank you for all your help during the first few years (I would have been lost without you) and for all the chats on your unique projects. Petar, thank you for all the fun times whenever you were here! And for passing down the thesis-nailing hammer. Thank you all for all the fun times out and the coffee trips in flock-formation after lunch!

For the cumbersome part of reading my thesis, I want to thank once again Richard, Arnaud, Elin, Vojtech, Venu, Jonas and Geoffrey.

To my friends. Thank you for being there during the good, crazy, bad and super-crazy-bad times. Thank you for the support packages with motivating mugs on them. Thank you for the midday yoga videos and the midnight calls. Thank you for the hugs, understanding and love.

To my family. You are who shaped me to who I am. Ek, without you, I don't think I would have an inch of humour in my life. Or bruises... There is always a tradeoff. Mum, Dad, all the pictures of calmness and serenity in my mind, and the ability to reach for them in times of need, are thanks to you. All the trust, courage and joy to explore, are strong because of you. All the steps that I have taken are thanks to you.

Lefteri, you have helped me through my absolute worse. Thank you for arguing with me, laughing with me, taking walks with me and simply making everything better. I have no words for what you mean to me.

References

[1] M. Tanabashi *et al.*, "Particle data group," *Phys. Rev. D*, vol. 98, no. 3, p. 030001, 2018.

[2] J. Goldstone, A. Salam, and S. Weinberg, "Broken symmetries," *Phys. Rev.*, vol. 127, pp. 965–970, Aug 1962.

[3] F. Englert and R. Brout, "Broken symmetry and the mass of gauge vector mesons," *Phys. Rev. Lett.*, vol. 13, pp. 321–323, Aug 1964.

[4] P. W. Higgs, "Broken symmetries and the masses of gauge bosons," *Phys. Rev. Lett.*, vol. 13, pp. 508–509, Oct 1964.

[5] P. W. Higgs, "Spontaneous symmetry breakdown without massless bosons," *Phys. Rev.*, vol. 145, pp. 1156–1163, May 1966.

[6] ATLAS Collaboration, "Observation of a new particle in the search for the Standard Model Higgs boson with the ATLAS detector at the LHC," *Phys. Lett. B*, vol. 716, pp. 1–29. 29 p, Aug 2012.

[7] CMS Collaboration, "Observation of a new boson at a mass of 125 GeV with the CMS experiment at the LHC. Observation of a new boson at a mass of 125 GeV with the CMS experiment at the LHC," *Phys. Lett. B*, vol. 716, pp. 30–61. 32 p, Jul 2012.

[8] L. Alvarez-Gaumé and M. A. Vázquez-Mozo, *An invitation to quantum field theory*, vol. 839. Springer Science & Business Media, 2011.

[9] Super-Kamiokande Collaboration, "Evidence for oscillation of atmospheric neutrinos," *Phys. Rev. Lett.*, vol. 81, no. 8, p. 1562, 1998.

[10] SNO Collaboration, "Direct evidence for neutrino flavor transformation from neutral-current interactions in the sudbury neutrino observatory," *Phys. Rev. Lett.*, vol. 89, Jun 2002.

[11] G. C. Branco, P. Ferreira, L. Lavoura, M. Rebelo, M. Sher, and J. P. Silva, "Theory and phenomenology of two-higgs-doublet models," *Phys. Rep.*, vol. 516, no. 1-2, pp. 1–102, 2012.

[12] N. Craig and S. Thomas, "Exclusive signals of an extended higgs sector," *JHEP*, vol. 2012, no. 11, p. 83, 2012.

[13] H. E. Haber and G. L. Kane, "The search for supersymmetry: probing physics beyond the standard model," *Phys. Rep.*, vol. 117, no. 2-4, pp. 75–263, 1985.

[14] R. D. Peccei and H. R. Quinn, "CP conservation in the presence of pseudoparticles," *Phys. Rev. Lett.*, vol. 38, pp. 1440–1443, Jun 1977.

[15] M. Trodden, "Electroweak Baryogenesis: A Brief Review," Tech. Rep. hep-ph/9805252. CWRU-98-18, May 1998.

[16] S. L. Glashow and S. Weinberg, "Natural conservation laws for neutral currents," *Phys. Rev. D*, vol. 15, no. 7, p. 1958, 1977.

[17] C. Csaki, "The minimal supersymmetric standard model," *Mod. Phys. Lett. A*, vol. 11, no. 08, pp. 599–613, 1996.

[18] H. Murayama, "Supersymmetry phenomenology," *Particle physics. Proceedings, Summer School, Trieste, Italy*, pp. 296–335, 1999.

[19] N. Polonsky, *Supersymmetry: Structure and phenomena. Extensions of the standard model*, vol. 68. 2001.
[20] M. Carena, S. Heinemeyer, O. Stål, C. E. M. Wagner, and G. Weiglein, "Mssm higgs boson searches at the lhc: benchmark scenarios after the discovery of a higgs-like particle," *Eur. Phys. J. C*, vol. 73, Sep 2013.
[21] A. Djouadi, L. Maiani, G. Moreau, A. Polosa, J. Quevillon, and V. Riquer, "The post-higgs mssm scenario: habemus mssm?," *Eur. Phys. J. C*, vol. 73, no. 12, p. 2650, 2013.
[22] G. Knoll, *Radiation Detection and Measurements*. 4th ed., 2010.
[23] G. Lutz, *Semiconductor radiation detectors: device physics*. Springer, 2007.
[24] S. Sze, *Semiconductor Devices*. J. Wiley & Sons, 1985.
[25] Halbleiter, "Fundamentals: Conductors - insulators - semiconductors." `https://www.halbleiter.org/en/fundamentals/conductors-insulators-semiconductors/`. Accessed: 2020-12-30.
[26] A. Covington, "Quick reference manual for silicon integrated-circuit technology," *Electrochimica Acta*, vol. 31, no. 12, p. 1679, 1986.
[27] E. Britannica, "P-type semiconductor, electronics." `https://www.britannica.com/science/p-type-semiconductor`. Accessed: 2020-12-30.
[28] Pedia, "Difference between p-type and n-type semiconductor." `https://pediaa.com/difference-between-p-type-and-n-type-semiconductor/`. Accessed: 2020-12-30.
[29] A. S. Sedra and K. C. Smith, *Microelectronic circuits*. New York: Oxford University Press, 1998.
[30] C. Leroy and P.-G. Rancoita, *Principles of radiation interaction in matter and detection*. World Scientific, 2011.
[31] C. Fabjan, "Collider detectors for multi-tev particles," in *Encyclopedia of Physical Science and Technology (Third Edition)* (R. A. Meyers, ed.), pp. 253 – 268, New York: Academic Press, third edition ed., 2003.
[32] S. Seidel, "Silicon strip and pixel detectors for particle physics experiments," *Phys. Rep.*, vol. 828, pp. 1–34, 2019.
[33] F. Ferrazza, "Chapter IB-1 - Crystalline Silicon: Manufacture and Properties," in *Practical Handbook of Photovoltaics (Second Edition)* (A. McEvoy, T. Markvart, and L. Castañer, eds.), pp. 79 – 97, Boston: Academic Press, second edition ed., 2012.
[34] ATLAS Collaboration, "Technical Design Report for the ATLAS Inner Tracker Strip Detector," Tech. Rep. CERN-LHCC-2017-005. ATLAS-TDR-025, CERN, Geneva, Apr 2017.
[35] R. Turchetta, "CMOS monolithic active pixel sensors (MAPS) for scientific applications," 2003.
[36] ALICE Collaboration, "Technical Design Report for the Upgrade of the ALICE Inner Tracking System," Tech. Rep. CERN-LHCC-2013-024. ALICE-TDR-017, Nov 2013.
[37] I. Perić *et al.*, "High-voltage pixel detectors in commercial CMOS technologies for ATLAS, CLIC and Mu3e experiments," *Nucl. Instrum. Meth. A*, vol. 731, pp. 131–136, 2013.

[38] H. Augustin *et al.*, "The MuPix System-on-Chip for the Mu3e Experiment," *Nucl. Instrum. Meth. A*, vol. 845, pp. 194–198, 2017.
[39] L. R. Evans and P. Bryant, "LHC Machine," *JINST*, vol. 3, p. S08001. 164 p, 2008.
[40] E. Mobs, "The CERN accelerator complex - 2019. Complexe des accélérateurs du CERN - 2019," Jul 2019.
[41] ATLAS Collaboration, "The ATLAS Experiment at the CERN Large Hadron Collider," *JINST*, vol. 3, p. S08003. 437 p, 2008.
[42] CMS Collaboration, "The CMS experiment at the CERN LHC. The Compact Muon Solenoid experiment," *JINST*, vol. 3, p. S08004. 361 p, 2008.
[43] ALICE Collaboration, "The ALICE experiment at the CERN LHC. A Large Ion Collider Experiment," *JINST*, vol. 3, p. S08002. 259 p, 2008.
[44] LHCb Collaboration, "The LHCb Detector at the LHC," *JINST*, vol. 3, no. LHCb-DP-2008-001. CERN-LHCb-DP-2008-001, p. S08005, 2008.
[45] TOTEM Collaboration, "The TOTEM Experiment at the CERN Large Hadron Collider," *JINST*, vol. 3, p. S08007, 2008.
[46] LHCf Collaboration, "The LHCf detector at the CERN Large Hadron Collider," *JINST*, vol. 3, p. S08006, 2008.
[47] MoEDAL Collaboration, "Technical Design Report of the MoEDAL Experiment," Tech. Rep. CERN-LHCC-2009-006. MoEDAL-TDR-001, Jun 2009.
[48] O. S. Brüning *et al.*, *LHC Design Report*. CERN Yellow Reports: Monographs, Geneva: CERN, 2004.
[49] ATLAS Collaboration, "Luminosity public results Run 2." `https://twiki.cern.ch/twiki/bin/view/AtlasPublic`. Accessed: 2020-12-30.
[50] B. Salvachúa, "Overview of proton-proton physics during Run 2," 2019.
[51] R. Steerenberg *et al.*, "Operation and performance of the CERN Large Hadron Collider during proton Run 2," no. CERN-ACC-2019-067, p. MOPMP031. 4 p, 2019.
[52] ATLAS Collaboration, "Luminosity public results Run 2." `https://twiki.cern.ch/twiki/bin/view/AtlasPublic/LuminosityPublicResultsRun2`. Accessed: 2020-12-30.
[53] ATLAS Collaboration, *ATLAS inner detector: Technical Design Report, 1*. Technical Design Report ATLAS, Geneva: CERN, 1997.
[54] J. Pequenao, "Computer generated image of the ATLAS inner detector." Mar 2008.
[55] ATLAS Collaboration, "ATLAS pixel detector electronics and sensors," *JINST*, vol. 3, p. P07007, 2008.
[56] A. Andreazza, "The ATLAS Pixel Detector operation and performance," Tech. Rep. ATL-INDET-PROC-2010-019, CERN, Geneva, Aug 2010.
[57] M. Capeans *et al.*, "ATLAS Insertable B-Layer Technical Design Report," Tech. Rep. CERN-LHCC-2010-013. ATLAS-TDR-19, Sep 2010.
[58] ATLAS Collaboration, "Operation and performance of the ATLAS semiconductor tracker," *JINST*, vol. 9, p. P08009. 80 p, Apr 2014.
[59] ATLAS Collaboration, "Performance of the ATLAS Transition Radiation Tracker in Run 1 of the LHC: tracker properties," *JINST*, vol. 12, p. P05002.

45 p, Feb 2017.
[60] ATLAS Collaboration, "Published tilecal figures." https://twiki.cern.ch/twiki/bin/view/AtlasPublic/PublishedTilecalFigures. Accessed: 2020-12-30.
[61] ATLAS Collaboration, *ATLAS muon spectrometer: Technical Design Report*. Technical Design Report ATLAS, Geneva: CERN, 1997.
[62] A. Ruiz-Martinez and A. Collaboration, "The Run-2 ATLAS Trigger System," Tech. Rep. ATL-DAQ-PROC-2016-003, CERN, Geneva, Feb 2016.
[63] A. D. Martin, W. J. Stirling, R. S. Thorne, and G. Watt, "Parton distributions for the lhc," *Eur. Phys. J. C*, vol. 63, p. 189–285, Jul 2009.
[64] ATLAS Collaboration, *ATLAS Computing: technical design report*. Technical Design Report ATLAS, Geneva: CERN, 2005.
[65] ATLAS Collaboration, "Performance of electron and photon triggers in ATLAS during LHC Run 2," *Eur. Phys. J. C*, vol. 80, p. 47. 56 p, Sep 2019.
[66] R. Achenbach *et al.*, "First data with the ATLAS Level-1 Calorimeter Trigger," Tech. Rep. ATL-DAQ-PROC-2008-006. ATL-COM-DAQ-2008-014, CERN, Geneva, Oct 2008.
[67] ATLAS Collaboration, "Electron reconstruction and identification in the ATLAS experiment using the 2015 and 2016 LHC proton-proton collision data at $\sqrt{s} = 13$ TeV," *Eur. Phys. J. C*, vol. 79, p. 639. 40 p, Feb 2019.
[68] ATLAS Collaboration, "Measurement of the photon identification efficiencies with the ATLAS detector using LHC Run 2 data collected in 2015 and 2016," *Eur. Phys. J. C*, vol. 79, p. 205. 55 p, Oct 2018.
[69] ATLAS Collaboration, "Performance of the ATLAS muon triggers in Run 2," *JINST*, vol. 15, p. P09015. 58 p, Apr 2020.
[70] ATLAS Collaboration, "Muon reconstruction performance of the ATLAS detector in proton–proton collision data at $\sqrt{s}$=13 TeV," *Eur. Phys. J. C*, vol. 76, p. 292. 45 p, Mar 2016.
[71] J. Illingworth and J. Kittler, "A survey of the hough transform," *Computer Vision, Graphics, and Image Processing*, vol. 44, no. 1, pp. 87 – 116, 1988.
[72] ATLAS Collaboration, "Muon reconstruction and identification efficiency in ATLAS using the full Run 2 pp collision data set at $\sqrt{s} = 13$ TeV," Tech. Rep. CERN-EP-2020-199, CERN, Geneva, Dec 2020.
[73] M. Cacciari, G. P. Salam, and G. Soyez, "The anti-kt jet clustering algorithm," *JHEP*, vol. 2008, no. 04, p. 063, 2008.
[74] A. Hrynevich, "ATLAS jet and missing energy reconstruction, calibration and performance in LHC Run-2," Tech. Rep. ATL-PHYS-PROC-2017-045. 06, CERN, Geneva, May 2017.
[75] ATLAS Collaboration, "Topological cell clustering in the ATLAS calorimeters and its performance in LHC Run 1," *Eur. Phys. J. C*, vol. 77, p. 490. 87 p, Mar 2016.
[76] ATLAS Collaboration, "Jet global sequential corrections with the ATLAS detector in proton-proton collisions at $\sqrt{s} = 8$ TeV," Tech. Rep. ATLAS-CONF-2015-002, CERN, Geneva, Mar 2015.
[77] ATLAS Collaboration, "Measurements of b-jet tagging efficiency with the ATLAS detector using $t\bar{t}$ events at $\sqrt{s} = 13$ TeV," *JHEP*, vol. 08, p. 089. 49 p, May 2018.

[78] ATLAS Collaboration, "The ATLAS Tau Trigger in Run 2," Tech. Rep. ATLAS-CONF-2017-061, CERN, Geneva, Jul 2017.
[79] ATLAS Collaboration, "Reconstruction, Energy Calibration, and Identification of Hadronically Decaying Tau Leptons in the ATLAS Experiment for Run-2 of the LHC," Tech. Rep. ATL-PHYS-PUB-2015-045, CERN, Geneva, Nov 2015.
[80] ATLAS Collaboration, "Identification of hadronic tau lepton decays using neural networks in the ATLAS experiment," Tech. Rep. ATL-PHYS-PUB-2019-033, CERN, Geneva, Aug 2019.
[81] G. Choudalakis, "On hypothesis testing, trials factor, hypertests and the BumpHunter," Tech. Rep. arXiv:1101.0390, Jan 2011.
[82] G. Cowan, K. Cranmer, E. Gross, and O. Vitells, "Asymptotic formulae for likelihood-based tests of new physics," *Eur. Phys. J. C*, vol. 71, no. 2, pp. 1–19, 2011.
[83] ATLAS Collaboration, "Search for charged Higgs bosons produced in association with a top quark and decaying via $H^{\pm} \to \tau\nu$ using pp collision data recorded at $\sqrt{s} = 13$ TeV by the ATLAS detector," *Phys. Lett. B*, vol. 759, pp. 555–574. 20 p, Mar 2016.
[84] ATLAS Collaboration, "Search for charged Higgs bosons decaying into top and bottom quarks at $\sqrt{s} = 13$ TeV with the ATLAS detector," *JHEP*, vol. 11, p. 085. 55 p, Aug 2018.
[85] ATLAS Collaboration, "Search for a light charged Higgs boson in the decay channel $H^+ \to c\bar{s}$ in $t\bar{t}$ events using pp collisions at $\sqrt{s}$ = 7 TeV with the ATLAS detector," *Eur. Phys. J. C*, vol. 73, p. 2465. 9 p, Feb 2013.
[86] ATLAS Collaboration, "Search for a Multi-Higgs Boson Cascade in $W^+W^-b\bar{b}$ events with the ATLAS detector in pp collisions at $\sqrt{s} = 8$TeV," *Phys. Rev. D*, vol. 89, p. 032002. 23 p, Dec 2013.
[87] CMS Collaboration, "Search for charged Higgs bosons in the $H^{\pm} \to \tau^{\pm}\nu_{\tau}$ decay channel in proton-proton collisions at $\sqrt{s} = 13$ TeV," *JHEP*, vol. 1907, p. 142. 43 p, Mar 2019.
[88] CMS Collaboration, "Search for charged Higgs bosons decaying into a top and a bottom quark in the all-jet final state of pp collisions at $\sqrt{s} = 13$ TeV," *JHEP*, vol. 2007, p. 126. 45 p, Jan 2020.
[89] CMS Collaboration, "Search for a charged Higgs boson decaying into top and bottom quarks in proton-proton collisions at $\sqrt{s} = 13$ TeV in events with electrons or muons," *JHEP*, vol. 2001, p. 096. 48 p, Aug 2019.
[90] CMS Collaboration, "Search for a light charged Higgs boson in the $H^{\pm} \to cs$ channel in proton-proton collisions at $\sqrt{s} = 13$ TeV," *Phys. Rev. D*, vol. 102, p. 072001. 26 p, May 2020.
[91] CMS Collaboration, "Search for a light charged Higgs boson decaying to a W boson and a CP-odd Higgs boson in final states with $e\mu\mu$ or $\mu\mu\mu$ in proton-proton collisions at $\sqrt{s} = 13$ TeV," *Phys. Rev. Lett.*, vol. 123, p. 131802. 18 p, May 2019.
[92] C. Degrande, R. Frederix, V. Hirschi, M. Ubiali, M. Wiesemann, and M. Zaro, "Accurate predictions for charged higgs production: Closing the $m_{H^{\pm}} \sim m_t$ window," *Phys. Lett. B*, vol. 772, pp. 87 – 92, 2017.
[93] A. Djouadi, L. Maiani, A. Polosa, J. Quevillon, and V. Riquer, "Fully covering the mssm higgs sector at the lhc," *JHEP*, vol. 2015, no. 6, p. 168, 2015.

[94] ATLAS Collaboration, "Search for charged Higgs bosons decaying via $H^{\pm} \to \tau^{\pm}\nu_{\tau}$ in the τ+jets and τ+lepton final states with 36 fb^{-1} of pp collision data recorded at $\sqrt{s} = 13$ TeV with the ATLAS experiment," *JHEP*, vol. 09, p. 139. 46 p, Jul 2018.
[95] J. Alwall *et al.*, "The automated computation of tree-level and next-to-leading order differential cross sections, and their matching to parton shower simulations," *JHEP*, vol. 2014, no. 7, p. 79, 2014.
[96] T. Sjöstrand, S. Mrenna, and P. Z. Skands, "A Brief Introduction to PYTHIA 8.1," *Comput. Phys. Commun.*, vol. 178, pp. 852–867. 27 p, Oct 2007.
[97] L. Devroye, "Nonuniform random variate generation," *Handbooks in operations research and management science*, vol. 13, pp. 83–121, 2006.
[98] ATLAS Collaboration, "Search for charged Higgs bosons decaying via $H^{\pm} \to \tau^{\pm}\nu$ in fully hadronic final states using pp collision data at $\sqrt{s}$ = 8 TeV with the ATLAS detector," *JHEP*, vol. 03, p. 088. 27 p, Dec 2014.
[99] G. Apollinari *et al.*, *High-Luminosity Large Hadron Collider (HL-LHC): Technical Design Report V. 0.1*. CERN Yellow Reports: Monographs, Geneva: CERN, 2017.
[100] HL-LHC Industry, "Project schedule." `https://project-hl-lhc-industry.web.cern.ch/content/project-schedule`. Accessed: 2020-12-30.
[101] P. Azzi *et al.*, "Report from Working Group 1: Standard Model Physics at the HL-LHC and HE-LHC," Tech. Rep. arXiv:1902.04070, CERN, Geneva, Dec 2018.
[102] X. Vidal *et al.*, "Report from Working Group 3: Beyond the Standard Model physics at the HL-LHC and HE-LHC," Tech. Rep. arXiv:1812.07831, CERN, Geneva, Dec 2018.
[103] M. Cepeda *et al.*, "Report from Working Group 2: Higgs Physics at the HL-LHC and HE-LHC," *CERN Yellow Rep. Monogr.*, vol. 7, pp. 221–584. 364 p, Dec 2018.
[104] A. Cerri *et al.*, "Report from Working Group 4: Opportunities in Flavour Physics at the HL-LHC and HE-LHC. Flavour Physics at the HL-LHC and HE-LHC," Tech. Rep. arXiv:1812.07638, CERN, Geneva, Dec 2018.
[105] ATLAS Collaboration, "Technical Design Report: A High-Granularity Timing Detector for the ATLAS Phase-II Upgrade," Tech. Rep. CERN-LHCC-2020-007. ATLAS-TDR-031, CERN, Geneva, Jun 2020.
[106] ATLAS Collaboration, "Technical Design Report for the Phase-II Upgrade of the ATLAS TDAQ System," Tech. Rep. CERN-LHCC-2017-020. ATLAS-TDR-029, CERN, Geneva, Sep 2017.
[107] ATLAS Collaboration, "Expected performance of the ATLAS detector at the High-Luminosity LHC," Tech. Rep. ATL-PHYS-PUB-2019-005, CERN, Geneva, Jan 2019.
[108] ATLAS Collaboration, "HL-LHC prospects for diboson resonance searches and electroweak vector boson scattering in the $WW/WZ \to \ell\nu qq$ final state," Tech. Rep. ATL-PHYS-PUB-2018-022, CERN, Geneva, Oct 2018.
[109] ATLAS Collaboration, "Prospective study of vector boson scattering in WZ fully leptonic final state at HL-LHC," Tech. Rep. ATL-PHYS-PUB-2018-023, CERN, Geneva, Oct 2018.

[110] ATLAS Collaboration, "Prospects for the measurement of the W-boson mass at the HL- and HE-LHC," Tech. Rep. ATL-PHYS-PUB-2018-026, CERN, Geneva, Oct 2018.
[111] ATLAS Collaboration, "Prospect study of electroweak production of a Z boson pair plus two jets at the HL-LHC," Tech. Rep. ATL-PHYS-PUB-2018-029, CERN, Geneva, Nov 2018.
[112] ATLAS Collaboration, "Prospect for a measurement of the Weak Mixing Angle in $pp \to Z/\gamma^* \to e^+e^-$ events with the ATLAS detector at the High Luminosity Large Hadron Collider," Tech. Rep. ATL-PHYS-PUB-2018-037, CERN, Geneva, Nov 2018.
[113] ATLAS Collaboration, "Prospects for the measurement of the $W^\pm W^\pm$ scattering cross section and extraction of the longitudinal scattering component in pp collisions at the High-Luminosity LHC with the ATLAS experiment," Tech. Rep. ATL-PHYS-PUB-2018-052, CERN, Geneva, Dec 2018.
[114] ATLAS Collaboration, "Measurement prospects of the pair production and self-coupling of the Higgs boson with the ATLAS experiment at the HL-LHC," Tech. Rep. ATL-PHYS-PUB-2018-053, CERN, Geneva, Dec 2018.
[115] ATLAS Collaboration, "Projections for measurements of Higgs boson cross sections, branching ratios, coupling parameters and mass with the ATLAS detector at the HL-LHC," Tech. Rep. ATL-PHYS-PUB-2018-054, CERN, Geneva, Dec 2018.
[116] ATLAS Collaboration, "Technical Design Report for the ATLAS ITk Pixel Detector," Tech. Rep. ATL-COM-ITK-2018-019, CERN, Geneva, Mar 2018.
[117] ATLAS Collaboration, "Latest performance studies of the ATLAS Inner Tracker (ITk) in the HL-LHC." https://atlas.web.cern.ch/Atlas/GROUPS/PHYSICS/PLOTS/IDTR-2019-009. Accessed: 2020-12-30.
[118] L. Poley *et al.*, "The ABC130 barrel module prototyping programme for the ATLAS strip tracker," *JINST*, vol. 15, p. P09004. 82 p, Sep 2020.
[119] C. Lacasta *et al.*, "Design of the first full size ATLAS ITk Strip sensor for the endcap region," Tech. Rep. ATL-ITK-PROC-2018-010, CERN, Geneva, Feb 2018.
[120] Henkel, "Loctite technical data sheet." http://tds.henkel.com/tds5/Studio/ShowPDF/AA%203525-EN?pid=AA%203525&format=MTR&subformat=REAC&language=EN&plant=WERCS. Accessed: 2020-12-30.
[121] A. Corporation, "Epolite FH 5313 epoxy for bonding a variety of substrates." https://www.andovercorp.com/products/accessories/epolite-fh-5313-epoxies/. Accessed: 2020-12-30.
[122] J. Steentoft, "Developing Module Assembly and Quality Control Procedures for the HL-LHC Upgrade of the ATLAS Inner Tracker," Dec 2019.
[123] G. L. Squires, *Introduction to the theory of thermal neutron scattering; 3rd ed.* Cambridge: Cambridge University Press, 2012.
[124] A. T. Boothroyd, *Principles of neutron scattering from condensed matter*. Oxford: Oxford University Press, 2020.
[125] S. Peggs (ed.), "ESS Technical Design Report," 2013.
[126] NIST Center for Neutron Research, "Neutron scattering lengths list." https://www.nist.gov/ncnr/neutron-scattering-lengths-list.

Accessed: 2020-12-30.

Appendix A.
ATLAS ITk strip sensor

Sensor properties

The specification for the silicon n+-in-p float-zone sensor used for the new ATLAS tracker, in view of the HL-LHC upgrade, are listed in Tab. A.1.

Substrate Material	
Size	8-inch/200 mm or 6-inch/150 mm
Type	p-type FZ
Crystal orientation	$\langle 100 \rangle$
Thickness (physical)	$300 - 320\,\mu$m
Thickness (active)	$\geq 90\%$ of physical thickness
Thickness tolerance	$\pm 5\%$
Resistivity	$> 3\,$kΩcm
Oxygen concentration	1×10^{16} to $7 \times 10^{17}\,$cm^{-3}
Sensor specifications before irradiation	
Full depletion voltage	$< 330\,$V (preference for $< 150\,$V)
Maximum operating voltage	700 V
Poly-silicon bias resistors	$1 - 2\,$MΩ
Inter-strip resistance	$> 10\times$ Rbias at 300 V at 23 C
Inter-strip capacitance	$< 1\,$pF/cm at 300 V, measured At 100 kHz
Coupling capacitance	$> 20\,$pF/cm at 1 kHz
Resistance of read-out Al strips	$< 15\,\Omega$/cm
Resistance of n-implant strip	$< 20\,$kΩ/cm
Onset of micro-discharge at	$> 700\,$V
Total initial leakage current, incl. guard rings	$< 0.1\,$mA/cm^2 at 700 V at room temperature
Number of strip defects	$< 1\%$ per strip and $< 1\%$ per sensor
After irradiation ($1.2 \times 10^{15}\,$neq/cm$^2 - 50\,$MRad)	
Onset of micro-discharge at	$> 700\,$V or $V_{\text{fulldepletion}} + 50\,$V after irradiation (if lower)
Inter-strip resistance	$> 10\times$ Rbias at 400 V and for $T = -20\,$C
Collected charge	> 7500 electrons per MIP at 500 V
Mechanical Specifications	
Dicing precision	$< \pm 20\,mu$m or better
Sensor bow after process and dicing	$< 200\,\mu$m

Table A.1. *Specifications for the n+-in-p-type sensor for the ITk strip detector. The table is also available in [34].*

Appendix B.
Quality Assessment and Quality Control procedures for the Strip EC module production

Quality Assurance during gluing - Hybrids

The gluing of the ASICs on the hybrids is carried out using a 5-dot pattern (Fig. B.1), with the Loctite 3525 UV-curing glue. In the following, the glue dispensing QA will be described, as followed by Uppsala University (UU).

In the scope of the UU activities, the glue dispensing is first optimized in in-house facilities and then incorporated in the industrial assembly procedures.

The tests were performed using a mini manual pick-and-place machine (Fig. B.1). The machine has a moving XY stage plate and a fixed (in XY) ASIC pick-up head holder, capable of travelling in Z for the ASIC pick-up and placement. A custom setup has been designed for the mounting of the hybrid, the ASIC alignment before the pick-up and the UV curing. The hybrid is placed on to the structure and is aligned with respect to a stopper on the jig, using the camera. Once the alignment is complete, the vacuum under the pad is switched on and the hybrid is ensured in place. The ASIC is placed in the extruding pocket of the jig, which keeps it aligned with respect to the pad it will be placed on. The machine supports custom ASIC pick-up heads, allowing the use of the tool designed for NOTE. A UV curing system has also been set in place. The machine is additionally equipped with a glue dispenser.

During operation, the center of the pad is located and a 5-dot pattern sequence is initiated. The pattern is achieved by movement of the stage through predefined positions. Once completed, the ASIC is lifted and placed on to the pad (by moving the table) and the UV curing is initiated. The legs of the ASIC pick-up head ensure the proper Z offset.

The glue dispenser is tunned with respect to the used pressure and time settings to optimize the dispensing. It is essential to avoid any excessive glue that could lead to spreading on the bonding pads, while ensuring proper support for bonding. A list of optimization tests is shown in Fig. B.2.

Quality Assurance during gluing - Modules

The gluing of components on the modules is carried out with a glue stencil or a glue robot, using a two-part epoxy glue. In the following, the glue dispensing using a glue robot, as developed and characterized by Uppsala University (UU), will be presented.

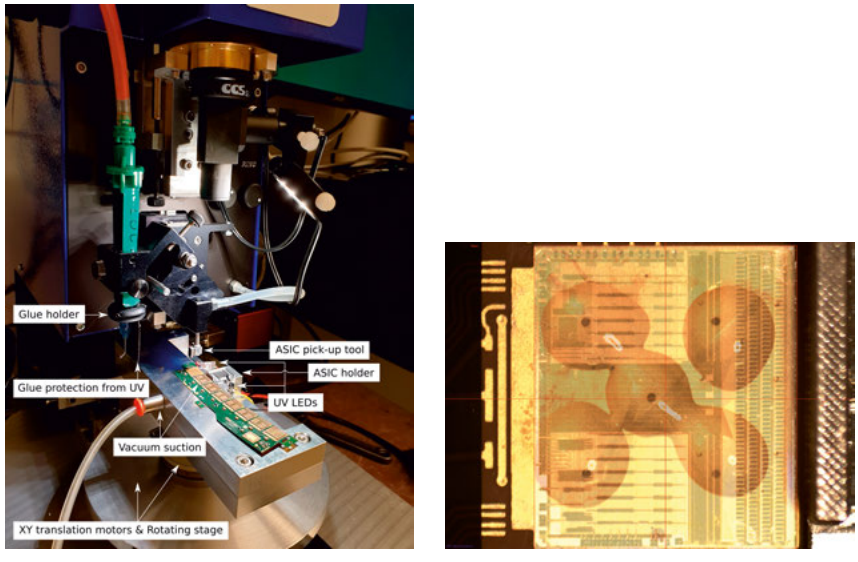

(a) (b)

Figure B.1. (a) Mini manual pick-and-place machine. (b) Picture of the 5-dot pattern, with an overlay of the ASIC on top.

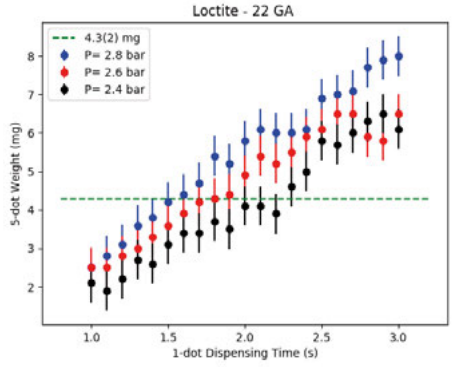

Figure B.2. In-house (UU) optimization study of glue dispensing for the (ABC) ASIC-to-Hybrid placement.

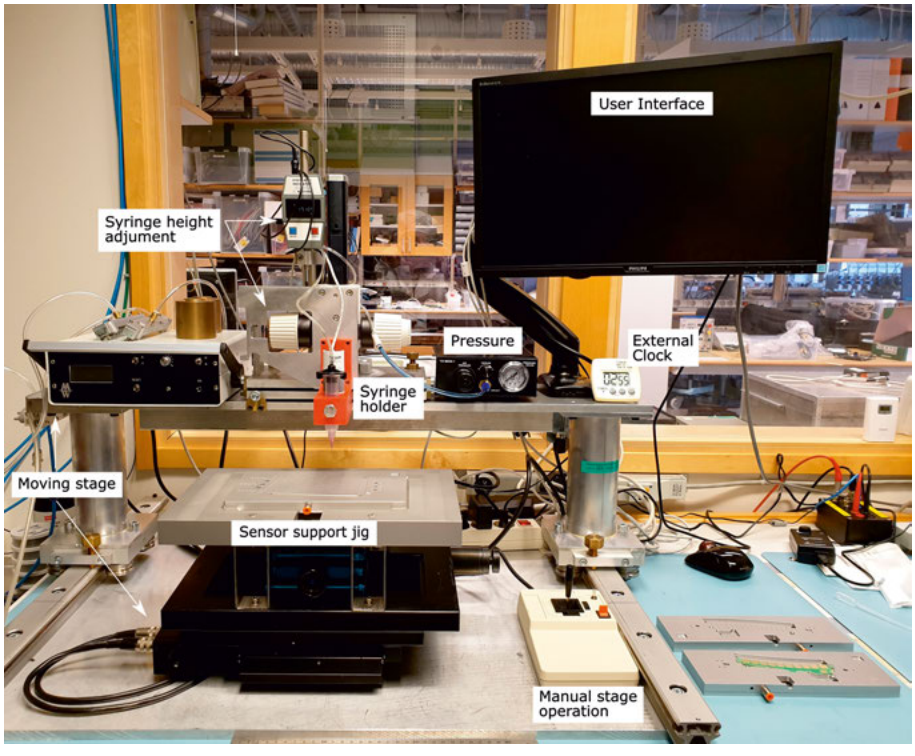

Figure B.3. Glue robot setup.

The gluing setup (Fig. B.3) is consisted of:

- a moving Marzhauser XY table,
- a fixed (in XY) mount for the syringe placement with μm precision in Z movements and
- an electric pneumatic valve for pressure actuation of the glue dispensing.

A Python script is used to control the XY-table coordinates and speed, as well as the pneumatic valve (on/off). The script is used to select the appropriate pattern for dispensing, turn on and off the pneumatic valve and logging this information in log-files after each sequence. A graphical user interface has been developed to make the operation of the robot by the industrial collaborators as simple and robust as possible.

The dispensing is carried out by keeping the glue syringe at a fixed Z offset from the top of the sensor and moving the XY table through pre-defined positions, allowing the dispensing of the patterns. The script relies on the following inputs; the list of patterns (one for each hybrid and powerboard type), the time since the glue mixing and a three-dimensional (glue mass, table speed, time after mixing) look-up table. The list of patterns and look-up table are provided by the developer (UU), while the time since mixing is handled automatically by the robot when the operator initiates it. The time is assumed

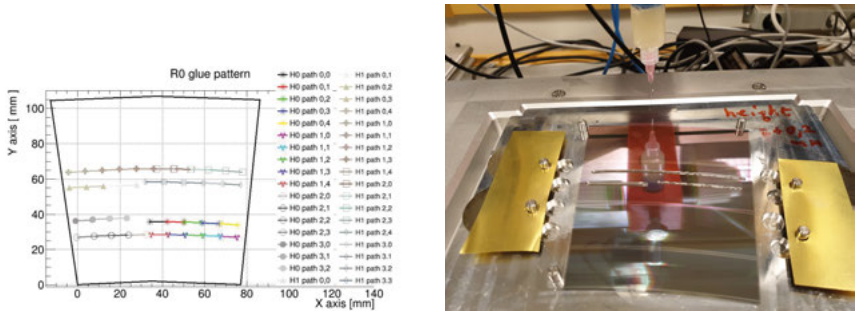

(a) (b)

Figure B.4. Example of the design (a) and dispensing (b) of the pattern lines for *R*0 module dispensing. The *R*0 module production was a common deliverable from all module production sites to kick-start the procedures while waiting for the preparation of the parts for the other module types.

to start counting from the initialization of the script unless otherwise stated by the operator. The pattern lines have been developed to follow closely the stencil patterns, while relying on 8 mm lines to simplify the QA. This choice is motivated because of the different sensor and hybrid geometries and therefore the need for dispensing suitable gluing patterns for each of them. The tunning of each individual pattern would require much longer time and was not considered needed. The segmentation of all patterns into 8 mm lines allows the development of a common dispensing approach, using the same look-up table, that offers the same coverage and support to the structure as the stencil patterns. An example of the patterns is illustrated in Fig. B.4. The look-up table has been developed by a series of runs where the same 8 mm lines have been dispensed using different table-speed settings at different times. An example of a preliminary version of the table is shown in Fig. B.5.

The operator of the robot carries out the following sequence of step for each gluing session:

1. **Preparation of the glue.** The glue components will be available in bottles and stored in cold storage. The correct amount of each part[4] is extracted, transferred to weight containers and left to reach room temperature. The two components are then mixed together using a plastic spatula for 3 min. At the time the mixing starts, the glue robot graphical user interface is initiated. Once the mixing is completed, the glue is transferred to a syringe and is mounted on the setup. The pressure is checked to be at 3.0 bar and a test dispensing is issued to check the connections and remove potential air bubbles.

[4]Mix ratio by weight should be: 100/9.

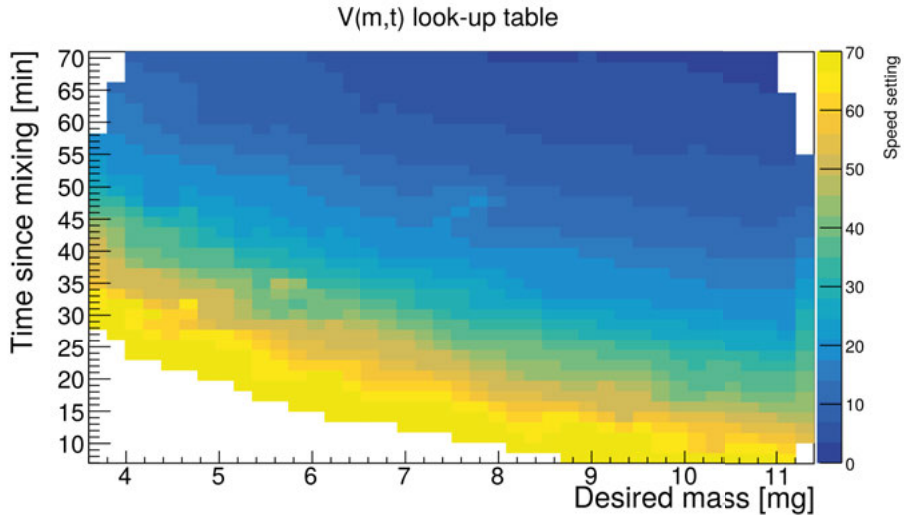

Figure B.5. Three-dimensional look-up table used during the pattern dispensing. Table prepared by J. Steentoft.

2. **Preparation of the sensor.** The sensor is mounted on to a vacuum suction support jig. The suction prohibits any movements of the sensor and keeps it flat.
3. **Preparation of the hybrids/powerboard.** The hybrids/powerboards are placed on the appropriate alignment jigs and lifted using the respective pick-up tools.
4. **Glue dispensing.** The appropriate dispensing pattern is requested and dispensed.
5. **Sensor removal from the setup.** The sensor jig is removed from the glue robot setup and placed on the side. This allows the use of the setup for another module production.
6. **Hybrids/powerboard placement.** Once the glue dispensing is finished the hybrids/powerboard are placed down on to the sensor.
7. **Addition of the weights.** Weights are placed on top of the hybrids/powerboard pick-up tool and are left in place during the curing. The purpose of the weights is to ensure a flat and uniform glue layer between the components.
8. **Curing.** The components are left to cure for 12 hrs. During this time the vacuum suction is kept on for all parts.

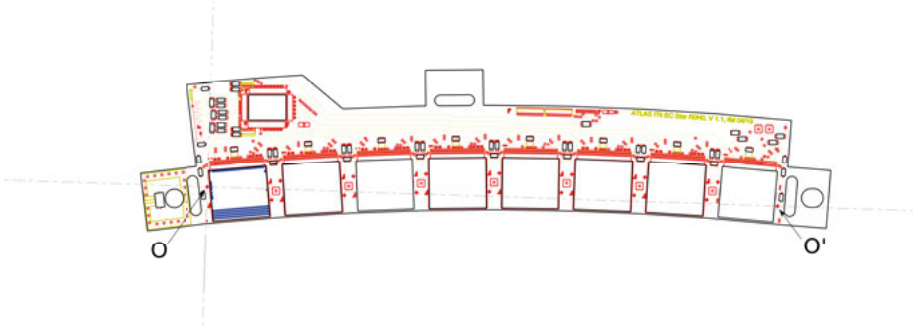

Figure B.6. Hybrid coordinate system for metrology tests. The photo has been taken from the ITk Strip EC metrology procedures documentation.

Metrology tests - Hybrids

The purpose of the hybrid metrology tests is to find errors in an early stage of the assembly that could potentially affect its quality. The errors that are being investigated are:

- Poor placement (x,y) of the ASICs, which can cause problems during their bonding to the hybrid or sensor.
- Non-uniform ASIC planarity (Z), which can lead to poor pick-up of the assembled hybrid during module production.
- Insufficient curing of the glue, which can lead to poor mechanical support.

In order to determine the x,y positions of features on the hybrids, one needs to establish a common coordinate system. This is defined with respect to fiducial marks on the hybrids, as illustrated for the case of the $R0H0$ module in Fig. B.6

Measurements concerning the x,y placements of the ASICs are carried out by (x,y) measurements of fiducial marks on all the ASICs, when the hybrid is held on vacuum (Fig. B.7). The values are compared with the expected value and only variations within a $\pm$ 0.1 mm margin are accepted.

Measurements concerning the Z placement of the ASICs are carried out by performing a scan of measurements on specific positions on the ASICs' surface and on the pad underneath, assuming the hybrid surface to be the horizontal reference plane (Fig. B.8). The values are used to calculate the glue thickness between the ASIC and the pad, by first calculating an average height for the top of the ASIC surface and then subtracting the ASIC thickness. The calculated thickness is compared to the glue target thickness: $120 \pm 40\,\mu$m. The values are also used to determine the flatness of the ASIC placement and only deviations within a $\pm\,40\,\mu$m margin are accepted.

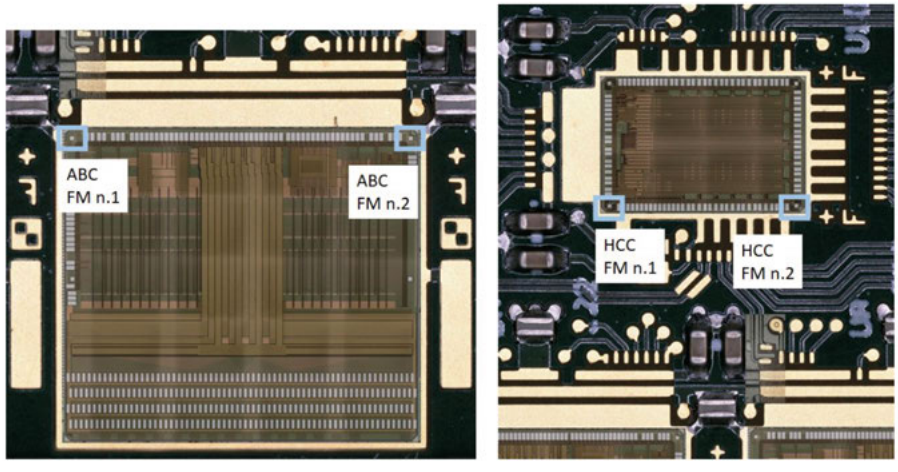

Figure B.7. Hybrid metrology for ASIC placement. The abbreviation “FM” stands for “fiducial marks" and refers to the pre-defined points used for the metrology. The photo has been taken from the ITk Strip EC metrology procedures documentation.

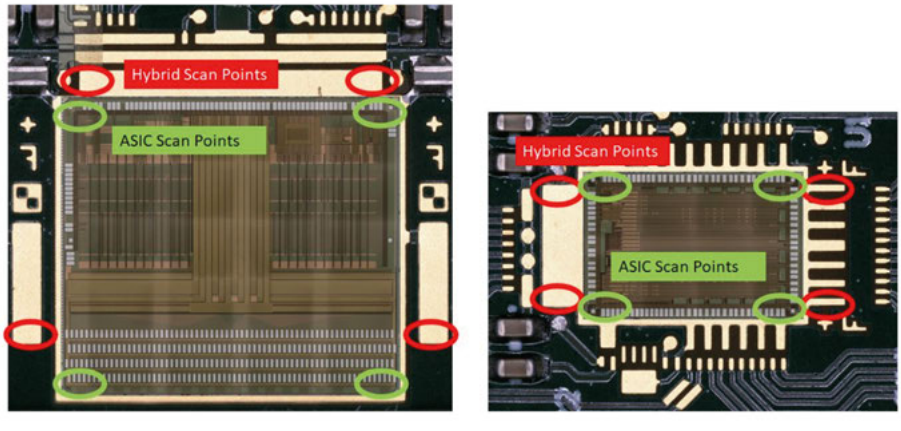

Figure B.8. Hybrid metrology for ASIC planarity. The photo has been taken from the ITk Strip EC metrology procedures documentation.

Metrology tests - Modules

The purpose of the module metrology tests is to identify errors in the assembly that could potentially affect its quality. The errors being investigated are:

- Glue thickness between the components (hybrids/powerboard) and the sensor.
- Poor placement of the components (hybrids/powerboard) on the sensor. In the case of a misplaced component the module needs to be rejected, as misplacement can cause bonding problems or inability to fit into the Petal.

Only modules that successfully pass these tests will proceed to be bonded.

The modules are placed on to a test frame with vacuum applied, and a scan is performed logging the x,y and z coordinates at a list of predefined points along the structure. An additional scan is performed without the vacuum, to evaluate possible sensor bow issues because of the assembly.

A common coordinate system (Fig. B.9) is used where:

- the x-axis is defined to be perpendicular to the strips' orientation, following the direction from the HCC edge to the high-voltage tab edge.
- the y-axis is defined to be parallel to the strips' orientation.
- The z-axis is defined to follow the direction upwards of the module surface.

The hybrids placement is evaluated using the same fiducial marks that are used for the hybrid alignment during the hybrid metrology tests, as described above. The powerboard placement is evaluated based on the two corners of the powerboard that are closest to the origin point.

For the glue thickness, a scan of points on the sensor surface on either side of the hybrids/powerboard is used to define a zero reference plane. The hybrid height is evaluated based on measurements on any exposed copper pads, for example those located in the gap between the ABC ASICs. The powerboard height is evaluated based on measurements on the bond pads. The glue thickness is calculated by first calculating the average and standard deviations of the measurements on the hybrids/powerboard and then subtracting their thicknesses.

Types of electrical tests

An overview of the ASIC electrical tests is described below. They are relevant for both the hybrid and module QC procedures, described in later sections of the Appendix.

An **ASIC communication** test is employed to verify the wire bond connections. The communication is evaluated through requests of personal IDs from each of the ASICs on the hybrid. The test is successful if all IDs are returned correctly.

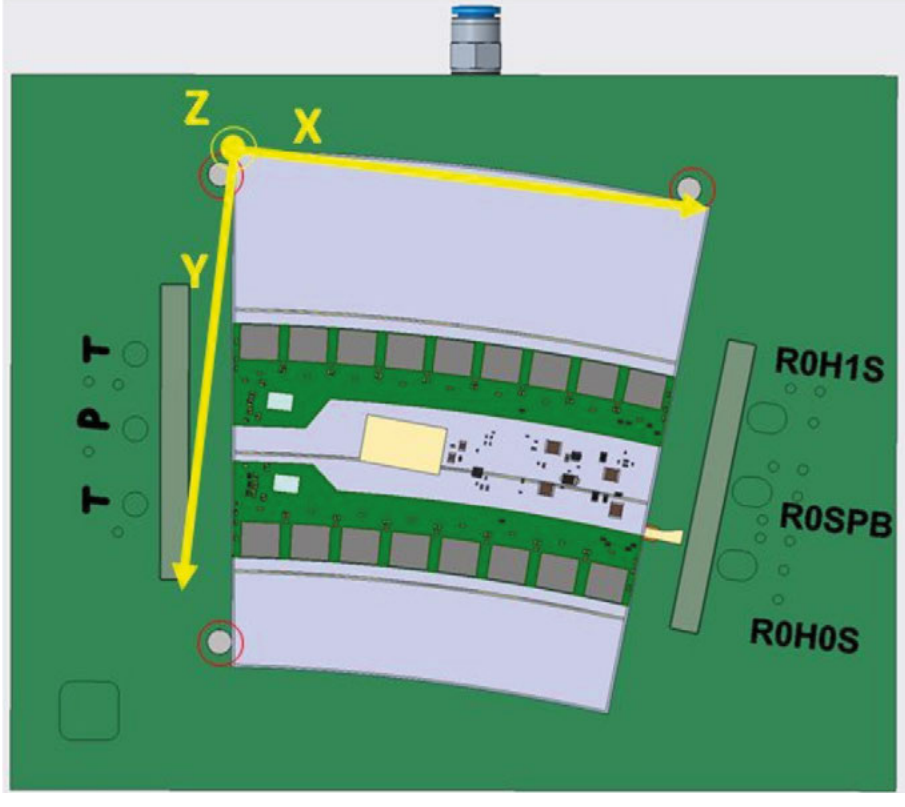

Figure B.9. Module metrology coordinate system. The photo has been taken from the ITk Strip EC metrology procedures documentation.

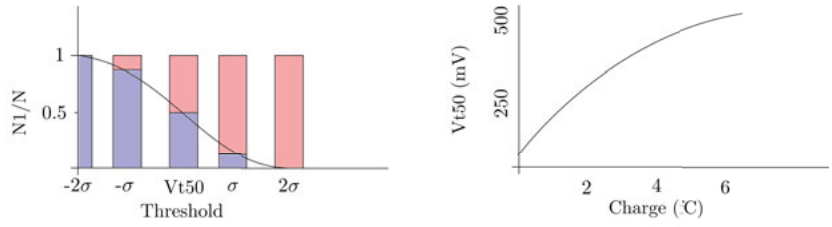

(a) (b)

Figure B.10. Qualitative illustrations of the threshold scan (a) and response curve (b) tests.

Each ASIC channel is responsible for amplifying the incoming signal, which corresponds to the collected charge from a given strip. The ABC ASICs however are binary readout chips which do not allow a direct knowledge of the gain in that ASIC. The determination of that amplification gain is instead possible by using statistical evaluation methods, such as threshold scans, on injected signals.

During a **threshold scan** a fixed simulated charge is chosen and injected into a channel. A list of different discrimination thresholds are examined to derive the most optimal configuration for that charge collection. This is done by performing N consecutive measurements and recording the number of measurements above the threshold (N1) to calculate the efficiency of the channel for that threshold:

$$\varepsilon = \frac{\mathrm{N1}}{\mathrm{N}}. \tag{15.1}$$

The same sequence is repeated for multiple threshold values and a threshold scan curve is retrieved (Fig. B.10). The objective is the identification of the discrimination threshold that allows 50% signal collection efficiency (Vt50).

The same test can be repeated for multiple injected charge values. Typical choices are: 1 fC, 2 fC, 4 fC, etc.

A **three-point-gain** test is the performance of the threshold scans for three different injection charge values; one nominal and two antisymmetric offset values. For example, for an injection charge of 1 fC, the ± 0.5 fC values are scanned as well. The variation is considered small and a linear fit of the Vt50 distribution is performed with respect to the injected charge value. The slope of the fit corresponds to the gain (mV/fC).

In a similar fashion, the **response curve** test relies on performing the threshold scan over 10 different injection charge values and the extraction of their respective Vt50 thresholds. The collected Vt50 distribution is fit with an exponential function with respect to the injected charge value (Fig. B.10).

The tests are performed individually for each channel, but the goal is to see the full picture. The desired outcome is to obtain a flat Vt50 threshold value

distribution across all ASICs, or as close to that as possible. This will imply a constant gain for all the channels, i.e. same amplification settings for all the strips. For the case of the ABC130 ASICs the specifications required a $90-95\%$ average gain.

A **strobe delay** test concerns the determination of the optimal time window for the read-out of the collected data once a read-out request has been made. Upon such a request, the collected charge in each channel is compared to the discriminating threshold to issue a hit/no-hit output. Each channel however has a different pulse rise time and it is possible that a false hit/no-hit is determined if the comparison is performed too late/soon. The strobe delay test is performed by injecting a set charge value and setting a much lower discrimination threshold. It is expected that the output will record a hit if the comparison of the injection pulse to the threshold is done within the correct time window. A list of strobe delay values is tested, where the test pulse is injected for 200 times. The efficiency is recorded and a final strobe delay value for each channel is chosen so that the measurements are within the efficiency plateau.

The **trim range** test is required to minimize the variation among the channels on their threshold scan responses.

The **noise occupancy** tests is among the most crucial tests as it determines the false hits (noise) recorded at different threshold values, when no injection charge is applied. It is expected to have less noise at higher thresholds. The measurements are reported as Equivalent Noise Charge (ENC), i.e. the number of electrons that would result in the recorded pulse.

Electrical & thermal tests - Hybrids

Once the ASICs have been placed on the hybrid PCBs, the hybrids are placed in groups on to a panel, where they are kept for bonding and the subsequent electrical and thermal tests.

The hybrids are first subjected to a single electrical test to test proper functionality. The test includes:

- an ASIC communication test, to ensure proper bonding,
- establishment of proper communication through the pads responsible for transmission/reception of the AMAC control signals,
- confirmation of hybrid thermistor temperature read-output,
- a strobe delay test,
- a three-point-gain test.

A hybrid is considered of good quality if less than 2% of the read-out channels fail the tests and if multiple channel failures occur, they should be fewer than eight in series. Only the panels where all the hybrids successfully pass the electrical tests move on to the burn-in tests.

The burn-in tests are comprised from a combination of electrical and thermal tests and aim to minimize the hybrids that are likely to fail during the infant mortality phase. The tests are performed within a custom crate, designed to hold multiple panels at once and ensure optimal cooling during the tests. The burn-in tests require an initial testing sequence focused on:

- establishment of proper communication through the pads responsible for transmission/reception of the AMAC control signals,
- confirmation of hybrid thermistor temperature read-output,
- electrical characterization of the hybrids through monitoring of the on-board current, voltage and temperature at a hybrid thermistor temperature of 40 C.

Once the initial sequence is completed, it is possible to carry out the full burn-in testing procedure that spans for 100 hrs.. The testing needs to be performed at stable hybrid temperature of 40 C. The sequence will perform:

- an ASIC communication test,
- a strobe delay test,
- a three-point gain test,
- a response curve,
- a noise occupancy scan.

Electrical & thermal tests - Modules

The fully assembled modules are subjected to a combination of electrical and thermal tests (burn-in). A custom thermally insulated container ("cold-box") has been designed to perform these tests. The cold-box consists of four vacuum chucks that will support the modules. The chucks are placed on top of Peltier elements, with a heat exchange under them. The coolant from the chiller passes through the copper heat exchange.

Once all modules are loaded into the cold-box, a Nitrogen / dry-air flow is initiated to cool-down the modules down to -35 C ($\sim$ 1 hr.). Each module is then subjected to a sequence of thermal-cycles between -35 C and $+40$ C. A cycle is defined to start at -35 C and ends once the temperature does a full circle (up to $+40$ C and back down to -35 C) and will be repeated 10 times (12 hrs.). The temperature monitoring is done with the hybrid thermistor read-out.

Once the modules reaches -35 C and before the initialization of the thermal cycling a module characterization sequence is performed (lasting for roughly 30 min.), comprising of the following tests:

- an ASIC communication test,
- a strobe delay test,
- a trim range test,
- a three-point gain test,
- a response curve,

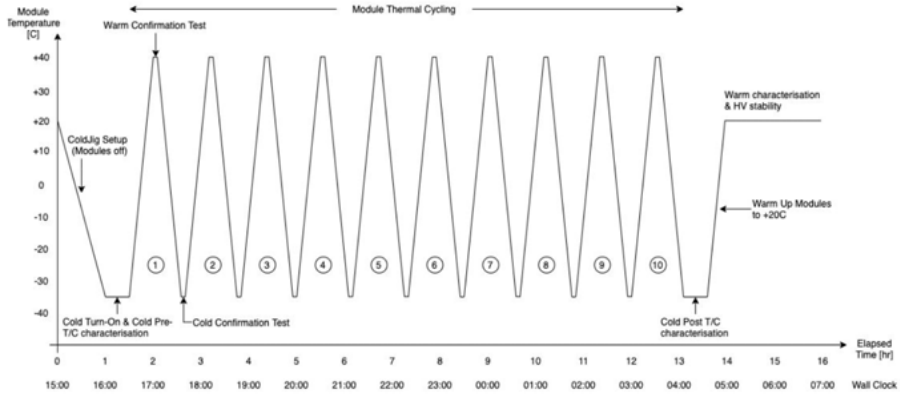

Figure B.11. Indicative timeline of a module burn-in test. The figure has been taken from the ITk Strip EC electrical tests documentation.

- a noise occupancy scan,
- an IV curve.

The sequence is also repeated after the completion of the thermal cycling. A module is considered of good quality if less than 2% of the read-out channels fail the tests and if multiple channel failures occur, they should be fewer than eight in series. The module should also not exhibit leakage current above $0.1\,\mu\mathrm{A/cm}^2$.

In between the cycles, at the max and min temperature values, a quick (5 min.) sequence of confirmation tests is carried out, consisting of:

- an ASIC communication test, to ensure proper bonding,
- a strobe delay test,
- a three-point gain test,
- a monitoring of the AMAC readout (read sensor current, hybrid and power board thermistor temperature, DC/DC converter input voltage/current values).

After the full thermal cycling is completed, the module is warmed up to 20 C and a high-voltage stability test is performed. The modules remain biased and the current is monitored. The modules are considered to be of good quality if they demonstrate a stable current.

After the final test is performed, the cold-box is warmed up to room temperature, marking the completion of the tests. All aforementioned steps are illustrated in Fig. B.11.

Acta Universitatis Upsaliensis
Uppsala Dissertations from the Faculty of Science
Editor: The Dean of the Faculty of Science

1–11: 1970–1975

12. *Lars Thofelt*: Studies on leaf temperature recorded by direct measurement and by thermography. 1975.
13. *Monica Henricsson*: Nutritional studies on Chara globularis Thuill., Chara zeylanica Willd., and Chara haitensis Turpin. 1976.
14. *Göran Kloow*: Studies on Regenerated Cellulose by the Fluorescence Depolarization Technique. 1976.
15. *Carl-Magnus Backman*: A High Pressure Study of the Photolytic Decomposition of Azoethane and Propionyl Peroxide. 1976.
16. *Lennart Källströmer*: The significance of biotin and certain monosaccharides for the growth of Aspergillus niger on rhamnose medium at elevated temperature. 1977.
17. *Staffan Renlund*: Identification of Oxytocin and Vasopressin in the Bovine Adenohypophysis. 1978.
18. *Bengt Finnström*: Effects of pH, Ionic Strength and Light Intensity on the Flash Photolysis of L-tryptophan. 1978.
19. *Thomas C. Amu*: Diffusion in Dilute Solutions: An Experimental Study with Special Reference to the Effect of Size and Shape of Solute and Solvent Molecules. 1978.
20. *Lars Tegnér*: A Flash Photolysis Study of the Thermal Cis-Trans Isomerization of Some Aromatic Schiff Bases in Solution. 1979.
21. *Stig Tormod*: A High-Speed Stopped Flow Laser Light Scattering Apparatus and its Application in a Study of Conformational Changes in Bovine Serum Albumin. 1985.
22. *Björn Varnestig*: Coulomb Excitation of Rotational Nuclei. 1987.
23. *Frans Lettenström*: A study of nuclear effects in deep inelastic muon scattering. 1988.
24. *Göran Ericsson*: Production of Heavy Hypernuclei in Antiproton Annihilation. Study of their decay in the fission channel. 1988.
25. *Fang Peng*: The Geopotential: Modelling Techniques and Physical Implications with Case Studies in the South and East China Sea and Fennoscandia. 1989.
26. *Md. Anowar Hossain*: Seismic Refraction Studies in the Baltic Shield along the Fennolora Profile. 1989.
27. *Lars Erik Svensson*: Coulomb Excitation of Vibrational Nuclei. 1989.
28. *Bengt Carlsson*: Digital differentiating filters and model based fault detection. 1989.
29. *Alexander Edgar Kavka*: Coulomb Excitation. Analytical Methods and Experimental Results on even Selenium Nuclei. 1989.
30. *Christopher Juhlin*: Seismic Attenuation, Shear Wave Anisotropy and Some Aspects of Fracturing in the Crystalline Rock of the Siljan Ring Area, Central Sweden. 1990.

31. *Torbjörn Wigren*: Recursive Identification Based on the Nonlinear Wiener Model. 1990.
32. *Kjell Janson*: Experimental investigations of the proton and deuteron structure functions. 1991.
33. *Suzanne W. Harris*: Positive Muons in Crystalline and Amorphous Solids. 1991.
34. *Jan Blomgren*: Experimental Studies of Giant Resonances in Medium-Weight Spherical Nuclei. 1991.
35. *Jonas Lindgren*: Waveform Inversion of Seismic Reflection Data through Local Optimisation Methods. 1992.
36. *Liqi Fang*: Dynamic Light Scattering from Polymer Gels and Semidilute Solutions. 1992.
37. *Raymond Munier*: Segmentation, Fragmentation and Jostling of the Baltic Shield with Time. 1993.

Prior to January 1994, the series was called *Uppsala Dissertations from the Faculty of Science*.

Acta Universitatis Upsaliensis

Uppsala Dissertations from the Faculty of Science and Technology
Editor: The Dean of the Faculty of Science

1–14: 1994–1997. 15–21: 1998–1999. 22–35: 2000–2001. 36–51: 2002–2003.

52. *Erik Larsson*: Identification of Stochastic Continuous-time Systems. Algorithms, Irregular Sampling and Cramér-Rao Bounds. 2004.
53. *Per Åhgren*: On System Identification and Acoustic Echo Cancellation. 2004.
54. *Felix Wehrmann*: On Modelling Nonlinear Variation in Discrete Appearances of Objects. 2004.
55. *Peter S. Hammerstein*: Stochastic Resonance and Noise-Assisted Signal Transfer. On Coupling-Effects of Stochastic Resonators and Spectral Optimization of Fluctuations in Random Network Switches. 2004.
56. *Esteban Damián Avendaño Soto*: Electrochromism in Nickel-based Oxides. Coloration Mechanisms and Optimization of Sputter-deposited Thin Films. 2004.
57. *Jenny Öhman Persson*: The Obvious & The Essential. Interpreting Software Development & Organizational Change. 2004.
58. *Chariklia Rouki*: Experimental Studies of the Synthesis and the Survival Probability of Transactinides. 2004.
59. *Emad Abd-Elrady*: Nonlinear Approaches to Periodic Signal Modeling. 2005.
60. *Marcus Nilsson*: Regular Model Checking. 2005.
61. *Pritha Mahata*: Model Checking Parameterized Timed Systems. 2005.
62. *Anders Berglund*: Learning computer systems in a distributed project course: The what, why, how and where. 2005.
63. *Barbara Piechocinska*: Physics from Wholeness. Dynamical Totality as a Conceptual Foundation for Physical Theories. 2005.
64. *Pär Samuelsson*: Control of Nitrogen Removal in Activated Sludge Processes. 2005.

65. *Mats Ekman*: Modeling and Control of Bilinear Systems. Application to the Activated Sludge Process. 2005.
66. *Milena Ivanova*: Scalable Scientific Stream Query Processing. 2005.
67. *Zoran Radovic´*: Software Techniques for Distributed Shared Memory. 2005.
68. *Richard Abrahamsson*: Estimation Problems in Array Signal Processing, System Identification, and Radar Imagery. 2006.
69. *Fredrik Robelius*: Giant Oil Fields – The Highway to Oil. Giant Oil Fields and their Importance for Future Oil Production. 2007.
70. *Anna Davour*: Search for low mass WIMPs with the AMANDA neutrino telescope. 2007.
71. *Magnus Ågren*: Set Constraints for Local Search. 2007.
72. *Ahmed Rezine*: Parameterized Systems: Generalizing and Simplifying Automatic Verification. 2008.
73. *Linda Brus*: Nonlinear Identification and Control with Solar Energy Applications. 2008.
74. *Peter Nauclér*: Estimation and Control of Resonant Systems with Stochastic Disturbances. 2008.
75. *Johan Petrini*: Querying RDF Schema Views of Relational Databases. 2008.
76. *Noomene Ben Henda*: Infinite-state Stochastic and Parameterized Systems. 2008.
77. *Samson Keleta*: Double Pion Production in dd→αππ Reaction. 2008.
78. *Mei Hong*: Analysis of Some Methods for Identifying Dynamic Errors-invariables Systems. 2008.
79. *Robin Strand*: Distance Functions and Image Processing on Point-Lattices With Focus on the 3D Face-and Body-centered Cubic Grids. 2008.
80. *Ruslan Fomkin*: Optimization and Execution of Complex Scientific Queries. 2009.
81. *John Airey*: Science, Language and Literacy. Case Studies of Learning in Swedish University Physics. 2009.
82. *Arvid Pohl*: Search for Subrelativistic Particles with the AMANDA Neutrino Telescope. 2009.
83. *Anna Danielsson*: Doing Physics – Doing Gender. An Exploration of Physics Students' Identity Constitution in the Context of Laboratory Work. 2009.
84. *Karin Schönning*: Meson Production in pd Collisions. 2009.
85. *Henrik Petrén*: η Meson Production in Proton-Proton Collisions at Excess Energies of 40 and 72 MeV. 2009.
86. *Jan Henry Nyström*: Analysing Fault Tolerance for ERLANG Applications. 2009.
87. *John Håkansson*: Design and Verification of Component Based Real-Time Systems. 2009.
88. *Sophie Grape*: Studies of PWO Crystals and Simulations of the $\bar{p}p \to \bar{\Lambda}\Lambda, \bar{\Lambda}\Sigma^0$ Reactions for the PANDA Experiment. 2009.
90. *Agnes Rensfelt*. Viscoelastic Materials. Identification and Experiment Design. 2010.
91. *Erik Gudmundson*. Signal Processing for Spectroscopic Applications. 2010.
92. *Björn Halvarsson*. Interaction Analysis in Multivariable Control Systems. Applications to Bioreactors for Nitrogen Removal. 2010.
93. *Jesper Bengtson*. Formalising process calculi. 2010.
94. *Magnus Johansson*. Psi-calculi: a Framework for Mobile Process Calculi. Cook your own correct process calculus – just add data and logic. 2010.
95. *Karin Rathsman*. Modeling of Electron Cooling. Theory, Data and Applications. 2010.

96. *Liselott Dominicus van den Bussche*. Getting the Picture of University Physics. 2010.
97. *Olle Engdegård*. A Search for Dark Matter in the Sun with AMANDA and IceCube. 2011.
98. *Matthias Hudl.* Magnetic materials with tunable thermal, electrical, and dynamic properties. An experimental study of magnetocaloric, multiferroic, and spin-glass materials. 2012.
99. *Marcio Costa.* First-principles Studies of Local Structure Effects in Magnetic Materials. 2012.
100. *Patrik Adlarson*. Studies of the Decay $\eta \rightarrow \pi^+\pi^-\pi^0$ with WASA-at-COSY. 2012.
101. *Erik Thomé.* Multi-Strange and Charmed Antihyperon-Hyperon Physics for PANDA. 2012.
102. *Anette Löfström.* Implementing a Vision. Studying Leaders' Strategic Use of an Intranet while Exploring Ethnography within HCI. 2014.
103. *Martin Stigge.* Real-Time Workload Models: Expressiveness vs. Analysis Efficiency. 2014.
104. *Linda Åmand.* Ammonium Feedback Control in Wastewater Treatment Plants. 2014.
105. *Mikael Laaksoharju.* Designing for Autonomy. 2014.
106. *Soma Tayamon.* Nonlinear System Identification and Control Applied to Selective Catalytic Reduction Systems. 2014.
107. *Adrian Bahne.* Multichannel Audio Signal Processing. Room Correction and Sound Perception. 2014.
108. *Mojtaba Soltanalian.* Signal Design for Active Sensing and Communications. 2014.
109. *Håkan Selg.* Researching the Use of the Internet — A Beginner's Guide. 2014.
110. *Andrzej Pyszniak*. Development and Applications of Tracking of Pellet Streams. 2014.
111. *Olov Rosén*. Parallel Stochastic Estimation on Multicore Platforms. 2015.
112. *Yajun Wei*. Ferromagnetic Resonance as a Probe of Magnetization Dynamics. A Study of FeCo Thin Films and Trilayers. 2015.
113. *Marcus Björk*. Contributions to Signal Processing for MRI. 2015.
114. *Alexander Madsen*. Hunting the Charged Higgs Boson with Lepton Signatures in the ATLAS Experiment. 2015.
115. *Daniel Jansson*. Identification Techniques for Mathematical Modeling of the Human Smooth Pursuit System. 2015.
116. *Henric Taavola*. Dark Matter in the Galactic Halo. A Search Using Neutrino Induced Cascades in the DeepCore Extension of IceCube. 2015.
117. *Rickard Ström*. Exploring the Universe Using Neutrinos. A Search for Point Sources in the Southern Hemisphere Using the IceCube Neutrino Observatory. 2015.
118. *Li Caldeira Balkeståhl.* Measurement of the Dalitz Plot Distribution for $\eta \rightarrow \pi^+\pi^-\pi^0$ with KLOE. 2015.
119. *Johannes Nygren.* Input-Output Stability Analysis of Networked Control Systems. 2016.
120. *Joseph Scott.* Other Things Besides Number. Abstraction, Constraint Propagation, and String Variable Types. 2016.
121. *Andrej Andrejev*. Semantic Web Queries over Scientific Data. 2016.

122. *Johan Blom*. Model-Based Protocol Testing in an ERLANG Environment. 2016.
123. *Liang Dai*. Identification using Convexification and Recursion. 2016.
124. *Adriaan Larmuseau*. Protecting Functional Programs From Low-Level Attackers. 2016.
125. *Lena Heijkenskjöld*. Hadronic Decays of the ω Meson. 2016.
126. *Delphine Misao Lebrun*. Photonic crystals and photocatalysis. Study of titania inverse opals. 2016.
127. *Per Mattsson*. Modeling and identification of nonlinear and impulsive systems. 2016.
128. *Lars Melander*. Integrating Visual Data Flow Programming with Data Stream Management. 2016.
129. *Kristofer Severinsson*. Samarbete = Samverkan? En fallstudie av AIMday vid Uppsala universitet. 2016.
130. *Nina Fowler*. Walking the Plank of the Entrepreneurial University. The little spinout that could? 2017.
131. *Kaj Jansson*. Measurements of Neutron-induced Nuclear Reactions for More Precise Standard Cross Sections and Correlated Fission Properties. 2017.
132. *Petter Bertilsson Forsberg*. Collaboration in practice. A multiple case study on collaboration between small enterprises and university researchers. 2018.
133. *Andreas Löscher*. Targeted Property-Based Testing with Applications in Sensor Networks. 2018.
134. *Simon Widmark*. Causal MMSE Filters for Personal Audio. A Polynomial Matrix Approach. 2018.
135. *Damian Pszczel*. Search for a new light boson in meson decays. 2018.
136. *Joachim Pettersson*. From Strange to Charm. Meson production in electron-positron collisions. 2018.
137. *Elisabeth Unger*. The Extremes of Neutrino Astronomy. From Fermi Bubbles with IceCube to Ice Studies with ARIANNA. 2019.
138. *Monica Norberg*. Engagerat ledarskap för att skapa förutsättningar för allas delaktighet. Utgångspunkter i kvalitetsarbetet. 2019.
139. *Peter Backeman*. Quantifiers and Theories. A Lazy Aproach. 2019.
140. *Walter Ikegami Andersson*. Exploring the Merits and Challenges of Hyperon Physics. with PANDA at FAIR. 2020.
141. *Petar Bokan*. Pair production of Higgs bosons in the final state with bottom quarks and τ leptons in the ATLAS experiment. Search results using LHC Run 2 data and prospect studies at the HL-LHC. 2020.
142. *Carl Kronlid*. Engineered temporary networks. Effects of control and temporality on inter-organizational interaction. 2020.
143. *Alexander Burgman*. Bright Needles in a Haystack. A Search for Magnetic Monopoles Using the IceCube Neutrino Observatory. 2020.
144. *Eleni Myrto Asimakopoulou*. Search for charged Higgs bosons with tau-lepton signatures at the ATLAS experiment of the Large Hadron Collider and development of novel semiconductor particle detectors. 2021.